THE UNIVERSITY OF CHICAGO

PATTERN FORMING MECHANISMS OF COLOR VISION

A DISSERTATION SUBMITTED TO
THE FACULTY OF THE DIVISION OF THE PHYSICAL SCIENCES
IN CANDIDACY FOR THE DEGREE OF
DOCTOR OF PHILOSOPHY

DEPARTMENT OF PHYSICS

BY
ZILY BURSTEIN

CHICAGO, ILLINOIS
AUGUST 2022

To my mother and father, Leah Burstein and Dov Burstein.

[A]t a fundamental level color is a private experience. The subjective nature of color can hinder scientific inquiry, but it adds much to its allure. And through the study of color we hope to glean insight into fundamental aspects of human experience.

— "A Tour of Contemporary Color Vision Research"

TABLE OF CONTENTS

LIST OF FIGURES

ACKNOWLEDGMENTS

Foremost, I am grateful to David D. Reid, my mentor and collaborator. Thank you for cultivating my love for research, for encouraging me to ask interesting questions, and for convincing me that we could solve them. Without David, this thesis would not be possible.

I would like to thank Jack Cowan, who envisioned the application of his pivotal Wilson-Cowan equations to our understanding of color vision. Thank you also to Wim van Drongelen for his guidance, insights, and much-needed levity, which guided me throughout my graduate school journey. I was lucky to be a part of the van Drongelen lab, whose members Graham Smith, Somin Lee, Sylvia Edoigiawerie, Andrew Tryba, and Sarita Deshpande were a continuous source of inspiration and support. I am especially grateful to Graham Smith, for all of our meaningful conversations and the subsequent aha moments, and to Peter Thomas, whose scientific intuition and creativity were invaluable to this project. I would also like to thank my thesis committee, Wim van Drongelen, Jeffrey Harvey, Daniel Holz, Michael Rust, and Peter Thomas, for their patience and support. I am so honored to have had the opportunity to share my research with you.

Finally, I want to thank my family and friends for their endless love and support. I thank Megan Smallen for being the best friend anyone could ask for; Larisa and Felix Rozinsky and Nina and Leonid Burshteyn, for their treasured wisdom; and my brilliant brother, Guy Burstein, for keeping me grounded. One of my proudest achievements has been building a meaningful and joyous life with Ramon Feldbrin. Ramon, thank you for believing in me, laughing with me, and for being by my side through it all.

Above all, I thank my parents, Leah and Dov Burstein, my guiding lights. I am lucky to be your daughter.

ABSTRACT

While our understanding of the way single neurons process chromatic stimuli in the early visual pathway has advanced significantly over recent years, we do not yet know how these cells interact to form stable representations of hue. Drawing on the findings of physiological studies, this dissertation offers a dynamical model of how the primary visual cortex tunes for color, hinged on intracortical interactions and emergent network effects. After detailing the evolution of network activity through analytical and numerical approaches, I discuss the effects of the model's cortical parameters on the selectivity of the tuning curves. In particular, I explore the role of the model's thresholding nonlinearity in enhancing hue selectivity by expanding the region of stability, allowing for the precise encoding of chromatic stimuli in early vision. Finally, in the absence of a stimulus, the model is capable of explaining hallucinatory color perception via a Turing-like mechanism of biological pattern formation.

CHAPTER 1

INTRODUCTION

Our experience of color begins in the early visual pathway, where, from the moment light strikes the retina, photoreceptor cells set off the neural mechanisms by which the photons' chromatic information is converted to the hues we ultimately see. This transition relies on the processing of millions of neurons, each of which has a small, if not negligible, role. To understand color vision, we must therefore not only characterize how each of these individual cells respond to and relay chromatic information, but also how the aggregate properties of the resultant networks amount to our perception of color.

Over the past several decades, the field of color vision has made numerous advances in both of these arenas. Electrophysiological recordings of individual neurons have given us a clearer picture of how chromatic information flows through the visual pathway, and optical imaging experiments have shed light on the functional architecture of its central processing hubs. Meanwhile, clinical studies have characterized the endgame of these computations — the discrimination between different wavelengths of light as well as the genetic and contextual effects governing how we perceive them. Although we now know much about these first and final stages of the color processing pathway, the field of color vision is left asking: what constitutes the transition between the two stages, and at which point of the neural stream does it originate?

Several theories of color vision have sought to answer these questions at the level of the single neuron, assigning specific weights to the neuronal responses of successive layers of processing. However, as a modeler-dependent parameterization scheme aimed at reproducing specific color-tuning responses, such tuning is necessarily arbitrary and, therefore, not a reflection of the physiology of the brain. In "Multi-Stage Color Model," perhaps the most impactful of the iterations of the *standard model* of color vision [57], Russell and Karen De Valois frame the issue of cortical tuning as the development of "precise processing circuits

from very limited genetic instructions" [24]. They suggest that such specificity in tuning can arise on the basis of firing pattern correlations between nearby neurons, and further argue that the necessary mechanisms emerge "between, not within, individual cells." In effect, they call for the consideration of network dynamics, an urging which has proven prescient in light of electrophysiological studies of macaque visual cortex [48] that point to the need for a population theory of chromatic processing remarkably early in the visual pathway.

In this dissertation, I present a model of intracortical network dynamics that accounts for cells responsive to the gamut of hues without the need to fine-tune the input parameters. To do so, I begin by introducing the relevant anatomical structures as the stage for the single-neuron processing schemes of which the emergent hue tuning mechanism consists. Contrasting the features of these two levels of cortical processing sets us up to differentiate between the concepts of chromatic signalling and color sensation. It also reframes the transition between these first and final stages of the color pathway in terms of the underlying neuronal population dynamics throughout its course.

1.1 Anatomy of the Visual Pathway

The typical neuron involved in the color vision pathway communicates its chromatic information via a rapid change in membrane potential, from which propagates an electrical impulse and corresponding release of signalling molecules onto its neighboring cells. These molecules can be categorized into two types — excitatory neurotransmitters, which raise the membrane potentials of the postsynaptic neurons, making them more likely to fire and propagate the signal, and inhibitory neurotransmitters, which lower the target neurons' firing rates.

However, the flow of chromatic information starts with the absorption of photons by an unconventional type of neuron located at the back of the retina known as the photoreceptor cone. Human vision consists of three types of photoreceptor cells: the L, M, and S cones, named for the long, medium, and short wavelengths of the visible light spectrum to which

they are responsive. Figure 1.1 depicts a spectral sensitivity diagram, which characterizes the probability of a photon's absorption by each cone as a function of the light's wavelength. The L, M, and S cones are often called, the "red," "green," and "blue" cones for the color sensation elicited at the peak of each spectral curve. However, the principle of univariance holds that their signalling gives no information about the specific wavelength of the absorbed light and only the total number of photons absorbed [82]. Thus, a cone cell will respond identically to a wavelength close to the peak of its spectral curve and a different stimulus further away, if the light intensity of the latter compensates for its smaller absorption probability.

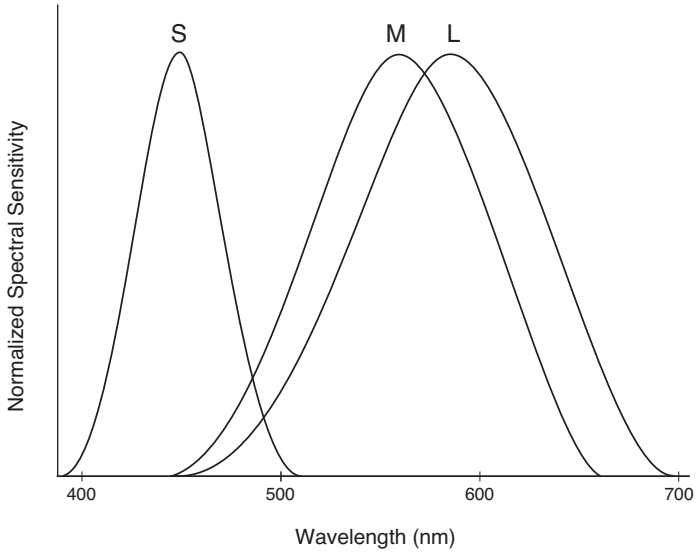

Figure 1.1: Spectral Sensitivity Diagram. The relative sensitivities of the cones are normalized to the same peak. Replicated from [89].

Furthermore, unlike the classical neuron, the cones do not communicate with other neurons with an all-or-nothing action potential, but with a graded change in membrane potential proportional to the stimulus strength. The subsequent release of neurotransmitters onto the next layer of retinal nerve cells is thus closely modulated by the intensity of light. In the final layer of the retinal processing stage, illustrated in figure 1.3, the signal is transmitted into

two types of ganglion cells, which signal via the typical action potential mechanism. The most common type of ganglion cell, called the P cell, is characterized by a center-surround, cone-opponent receptive field, which means that the neuron is maximally activated by an increment (+) or decrement (−) of input from either the L or M cone onto its innermost sensory space and a simultaneous input of the opposite sign and from the other cone type onto its outer region [17]. The second type of ganglion cell, called the K cell, is maximally activated by increments of S cone input and decrements of L+M cone input, but there is disagreement about whether these neurons display a center-surround spatial opponency similar to the P cells [20, 60]. A schematic of the P and K cells' receptive fields is given in figure 1.2. In addition, some have proposed the existence of an analogous −S+(L+M) ganglion cell, though it has yet to be confirmed by experiment [75, 86].

What we do know, however, is that at this point of the visual system, the signals are divided into two *cardinal* pathways: the L/M pathway and the S/(L+M) pathway, encoded in the cone-opponent responses of the P and K cells, respectively. This subtractive computation amplifies the signal-to-noise ratio through the comparison of the otherwise largely overlapping cone responses seen in the spectral sensitivity curves [36, 57]. From here, the two types of signals travel through the optic nerve to the separate *parvocellular* and *koniocelluar* layers of the lateral geniculate nucleus (LGN), the first center of visual processing located inside the brain (see figure 1.3). The respective parvocellular LGN cells (postsynaptic to the P cells) and koniocellular LGN cells (postsynaptic to the K cells) have the same receptive field structures as their presynaptic cells [82, 84, 99, 104]. A separate *magnocellular* layer processes luminance signals conveyed as increments or decrements of L+M input.

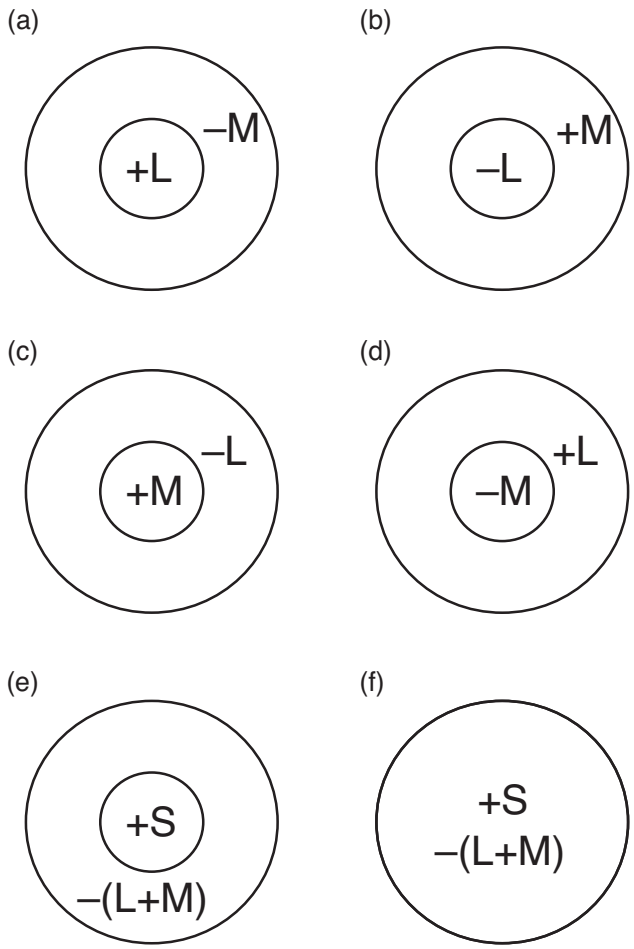

Figure 1.2: Schematic of Retinal Ganglion Cell Receptive Fields. (a) An L-ON retinal ganglion P cell is maximally excited by an increment of input from L cones onto the center of its receptive field and by a decrement of M cone input onto its surround. (b) An L-OFF ganglion P cell responds to the same cone inputs to the center and surround as the L-ON cell, but is maximally excited by input of the opposite sign. (c)-(d) For the M-ON P cell (c) and M-OFF P cell (d), the cone types to the center and surround are reversed from (a)-(b). (e) The S-ON K cells are less common in the retina. They exhibit maximal activation to increments of S and decrements of (L+M) signals. (f) Some reports have shown that these K cells do not exhibit spatial opponency.

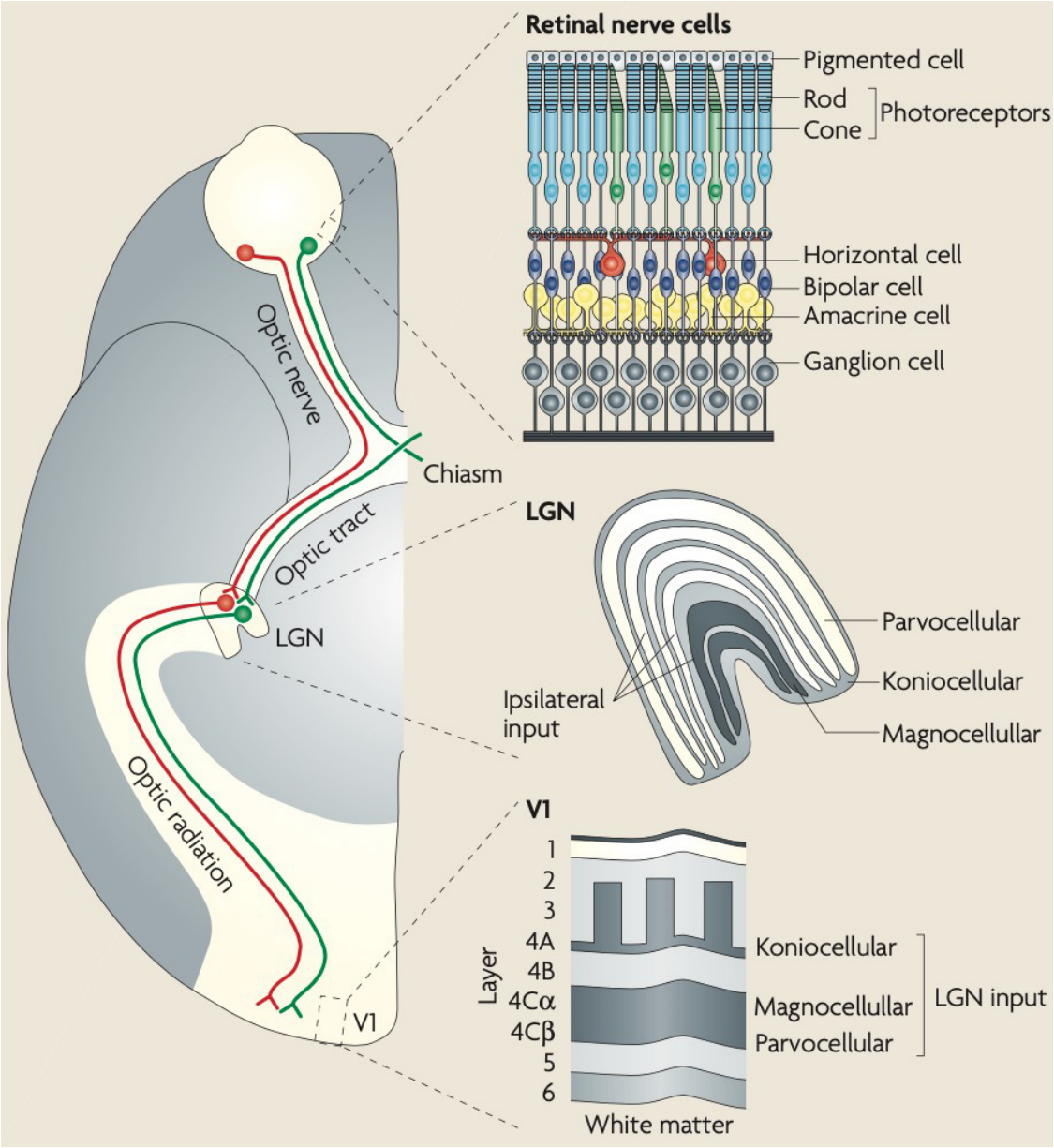

Figure 1.3: Early Visual Pathway. Reprinted by permission from Springer Nature: Nature Reviews Neuroscience. Machinery of Colour Vision, Solomon and Lennie, 2007 [86].

1.2 The Functional Organization of the Visual Cortex

LGN cells project onto distinct layers of the visual cortex (V1), as pictured in Fig. 1.3, and from there to the cells in layers 2 and 3 of V1, themselves presynaptic to other areas of the brain [39, 82, 83]. The receptive fields of these cortical cells are both larger and more varied than those of the retina and LGN. Foremost among them are the *double-opponent* cells, whose receptive fields consist of two color-opponent regions of opposite configurations. These cells are further divided into two subtypes: the concentric double-opponent cells and oriented double-opponent cells, both depicted in figure 1.4 [22, 34, 55]. Both receptive field structures allow the neurons to tune for patterns by recognizing boundaries between regions of different chromaticity, while the latter cells also tune for oriented stimuli due to their elongated receptive fields. In addition, V1 contains single-opponent cells, which are most responsive to non-oriented, full-field stimuli and display no sensitivity to edges [54, 55, 67, 83].

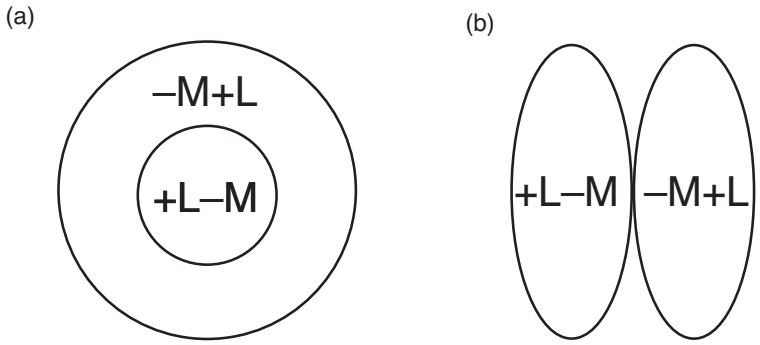

Figure 1.4: Schematic of Double-Opponent Receptive Fields. (a) A concentric configuration featured in cells within V1. (b) The elongated configuration of orientated double-opponent V1 cells.

The standard model of layers 2-3 of the visual cortex places non-oriented, color tuning cells in the so-called "CO blobs," cortical regions rich in the metabolic protein cytochrome oxidase, and oriented cells in the "interblob" regions between them [61, 68]. Within the

latter, orientation selectivity is arranged in a *pinwheel* formation, with neighboring neurons preferring similarly oriented stimuli. Figure 1.5 shows a horizontal cross-section of V1 primate cortex and its corresponding orientation preference map, comprised of many repeating pinwheels with unoriented CO blob centers. This figure also highlights the connectivity among the orientation-tuning cells within each pinwheel and the longer-range connections between them.

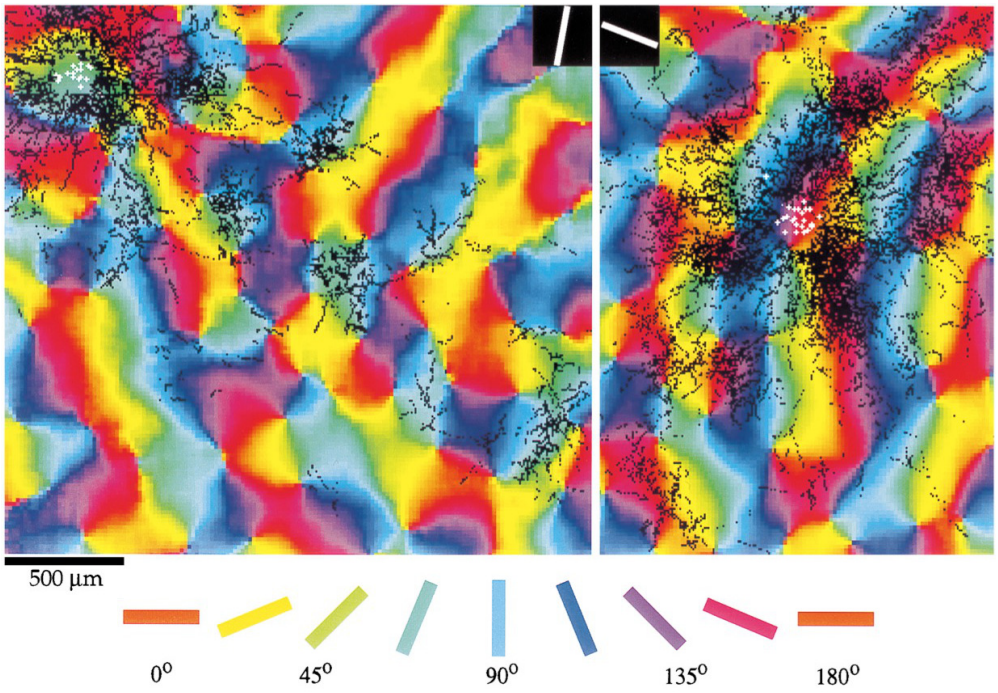

Figure 1.5: V1 orientation map obtained from optical imaging of the tree shrew cortex. Color is used to indicate the neurons' orientation preferences for grayscale bar stimuli. White symbols indicate the cells into which a marker was injected, while the black symbols are the labeled axons specifying the recurrent connectivity. The inserts indicate the orientation preference of the neurons at the injection sites. Reprinted from Bosking et al., [4]. Copyright 1997 Society for Neuroscience.

The pinwheel modules extend vertically, perpendicular to the surface of the brain and

across the cortical layers, with two pinwheel columns (one for each eye) forming the basic module of visual information processing known as the *hypercolumn* [2, 8, 68]. Each of these hypercolumns is roughly 1 mm^2 in area and responsive to both the chromaticity and orientation of stimuli detected by both eyes within a small region of the visual field [51, 93]. Figure 1.6 shows a schematic of the pinwheel column structure assumed in this text, though it is important to note that many have challenged this textbook picture of the visual cortex [76, 86]. Experiments have pointed out that the separation of the orientation- and color-processing pathways is blurrier than first predicted [34, 35, 53] and have called into question the complete alignment of the CO blobs with the pinwheel centers [2, 62, 106].

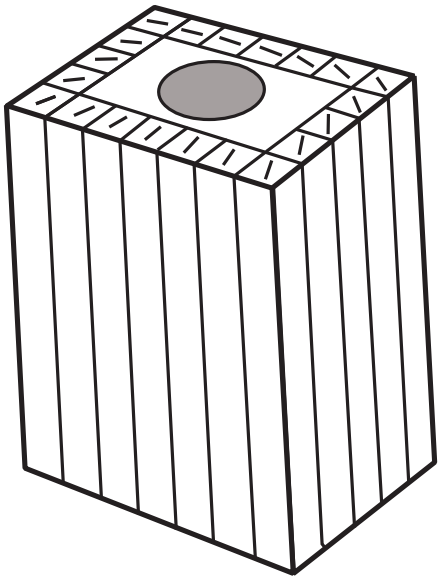

Figure 1.6: A schematic of a pinwheel column. In the *ice cube model* of the visual cortex [8, 93], the orientation map (see Fig. 1.5) runs through all cortical layers. Neighboring orientation columns prefer similar orientations in a pinwheel formation, the center of which is populated by color-preferring cells of low orientation selectivity in a region known as the CO blob.

Similarly, while we know that the L−M and S−(L+M) cone-opponent signals travel along separate pathways through the retina, LGN, and early stages of the visual cortex, there is yet no consensus as to how and where these signals are synthesized to encode hue. Electrophysiological studies of macaque visual cortex have shed some light on this question, pointing to the cortical layers 2-3 of V1 as the first point of convergence. Single-cell recordings have identified two main types of color responsive regions: color patches which contain neurons tuned exclusively to stimuli modulating either of the cone-opponent pathways [68] and patches with neurons exhibiting a *mixed* sensitivity to a combination of the two [61, 66]. At the same time, many experiments have shown that the processing of individual hues previously associated with higher-level mechanisms has its origins in V1 [23, 34, 35, 36, 44, 48, 64, 65, 66, 67, 92, 98, 104, 105]. These experiments have identified neurons in V1 tuned to the gamut of hues, and many have pointed to the role of processing nonlinearities in determining their tuning curves [23, 34, 44, 64, 98].

Compellingly, several of these experiments have shown that both the cone-opponent [62, 66, 68, 78] and hue-tuning [66, 105] cells mainly inhabit the CO blob regions of V1, and some have speculated that this colocalization stems from the sought-after mixing of the two cardinal pathways [66, 104]. This could mean that the same type of neuron is capable of encoding either cone-opponency or hue, depending on background network interactions. Conversely, other experiments have indicated a distinct population of hue-sensitive neurons in the interblob regions, more conclusively associated with orientation tuning and possibly receiving mixed input from the distinct cone-opponent neurons of the CO blobs [35, 61, 67, 107]. Equally unsettled is the question of how much S cone input contributes to the mixing of the cone-opponent channels, with some studies showing a relatively weak S cone input into the neurons of V1, compared to its L and M cone counterparts [66, 104]. The variations across these experiments may stem, in part, from differences in optical imaging and electrode penetration techniques, including the particulars of the chromatic stimulus

used [66, 67, 76, 78]. As a whole, however, these studies implicate a mixing mechanism which, beyond tying them together, points to the need for a population theory of chromatic processing in V1.

To that end, we must characterize the hue-specific intracortical connectivity between different populations of neurons, analogous to the geometrically organized connectivity seen in the orientation map of figure 1.5. In this regard, imaging studies have indicated a linear relationship between cortical distance and hue angle difference, which minimizes the wiring length of cells tuned to similar hues [66, 67, 105]. The hue-preferring cells inhabit the so-called "color regions," defined as such for their activation by red-green grating stimuli [67]. As mentioned above, these regions predominantly overlap with the CO blobs [66, 105] and are responsive to the full range of hues, much like the organization of orientation preference within the corresponding interblobs. Figure 1.7 shows the distribution of hue-responsive neurons within a typical color region (panel a) as well as a more coarse-grained demarcation of peak activity within several of these regions (panel b).

Yet while this hue-tuning micro-architecture implicates V1 as the substrate for the convergence of the two cone-opponent channels, it cannot single-handedly establish the mechanistic framework with which the cardinal pathways mix. It does not, for instance, specify whether the mixing occurs at the level of the single-neuron or as a population effect, or how neurons preferring different cone-opponent signals interact to encode hue. What is required, therefore, is a theory for the interactions underpinning the mixing mechanisms and, thereby, the transition of the neurons' chromatic receptive field properties on whose foundation lies our perception of hue. We thus continue with a discussion of previous theories of color tuning which have sought to model this transition and an overview of the mean field theory assumptions at the center of the model presented here.

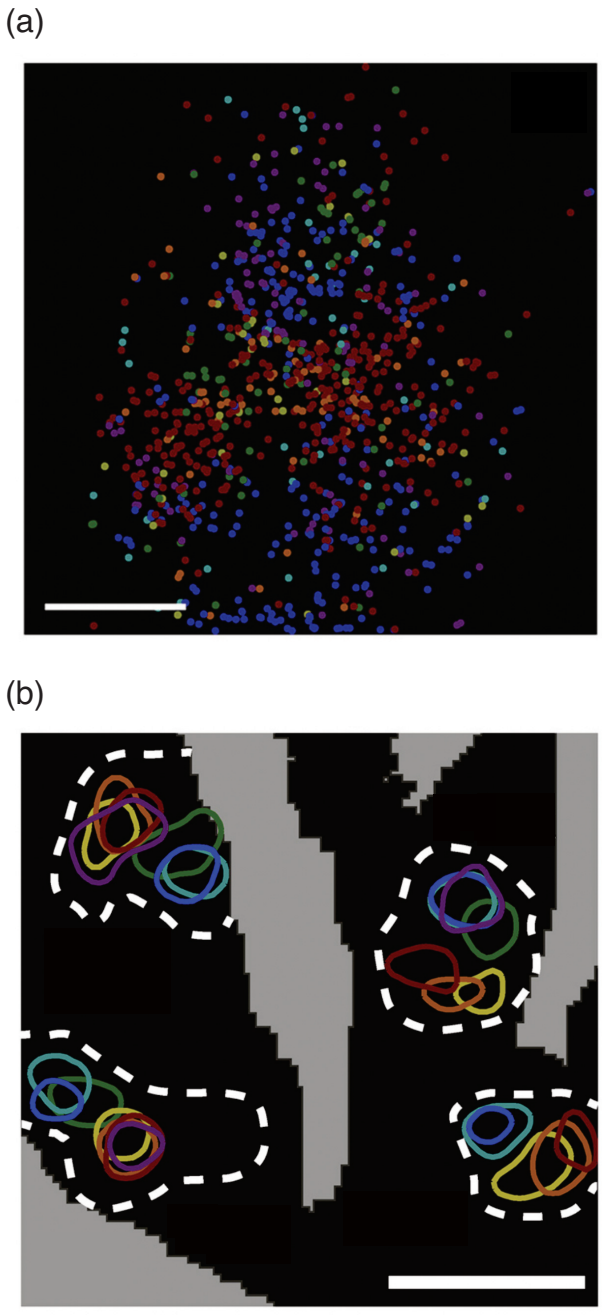

Figure 1.7: (a) Hue map of individual hue-selective cells obtained by 2-photon calcium imaging of neuronal responsiveness to seven test hues. Scale bar: 200 µm. (b) Regions of peak response to test hues (solid contours). The dashed white lines demarcate the color-preferring regions, colocalized with the CO blobs. Scale bar: 0.5 mm. Modified with permission from [67].

1.3 Theories of Color Vision

1.3.1 Physiology and Perception

Just as the L, M, and S cones are often mislabeled in terms of color, cone-opponency — observed in electrophysiological recordings of single neurons [83] — is often confounded with hue-opponency — a phenomenon first theorized by Ewald Hering in the nineteenth century and later mapped out in clinical studies by Jameson and Hurvich [23, 52, 84, 96]. Best depicted in the Derrington-Krauskopf-Lennie (DKL) stimulus space (Fig. 1.8), cone-opponency predicts that neurons tuned to either the L−M or S−(L+M) pathway will not respond to light whose wavelengths isolate the other [26, 31]. It is tempting to equate these null responses to the four unique hues of color-opponent theory, in which unique blue, for example, is observed when the "redness" and "greenness" of a perceived color exactly cancel. But the wavelengths of the unique hues specified by perceptual studies [52] only roughly match up with the wavelengths isolating either cone-opponent pathway [102, 103, 104], and, more fundamentally, we do not yet understand the mechanisms behind the processing which the analogy implies [72, 90, 96]. That is, how do we get from the single neurons' chromatic responses to our perception of color?

Yet despite these admonitions, cognition is best explored through its physiological counterparts, as is, for example, argued by Georgopolous et al. in motivating a population-based model of motor cortex and corresponding motor function [38]. The approach they detail proceeds in four steps, adapted here for models exploring the neuronal mechanisms of color perception:

1. Choose the cognitive variable of interest, e.g., color sensation.

2. Describe the activity of cells in the relevant cortical areas.

3. Select a specific color sensation, e.g., "redness" as is described in the perceptual studies

of Jameson and Hurvich [52].

4. Record neural activity in the cortical area during cognitive processing, i.e., during the subject's sensation of color.

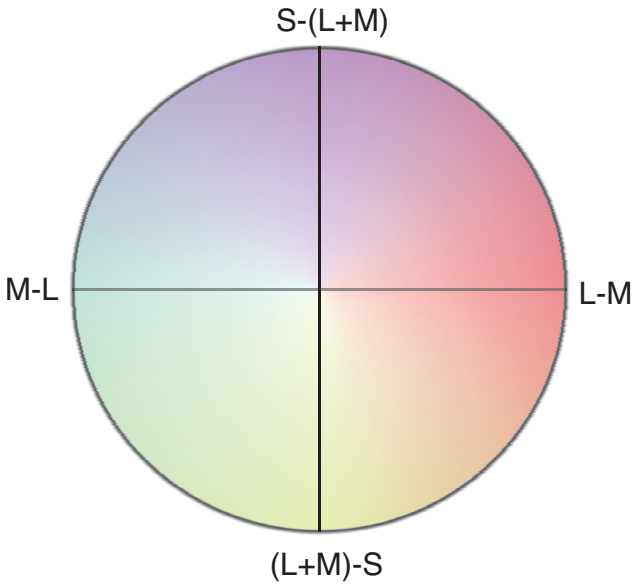

Figure 1.8: The DKL space maps chromatic stimuli onto a circle with two "cardinal" axes representing the L−M and S−(L+M) pathways. The excitatory or inhibitory effect of a stimulus on cone-opponent cells tuned to either pathway can be thought of as a projection of its location in DKL space onto the relevant axis. Stimuli isolating the two pathways correspond roughly to wavelengths associated with the red, green, blue, and yellow unique hues of opponent-color theory, leading to the common, but mistaken, conflation of chromatic stimulus and color perception.

While the field of color vision has made numerous advances in steps two and three, the subjective nature of color sensation, and thus the limited use of animal studies, poses many challenges for the final step. We cannot, after all, know what color sensation a monkey in an electrode experiment actually perceives. Nonetheless, the hallmark of previous color

models is the prediction of hue sensation at the final stage of processing [24, 70] or the confounding of cone- and color-opponency in their interpretations [32, 85, 88]. As we will see in chapter two, this contrasts with the model presented in this dissertation, which does not assign a sensation to the neuronal responses at the level of V1. Rather, proceeding in the confines of the physiological domain and DKL stimulus space (i.e., within step two above), we model the transition of intracortical *chromatic* receptive field properties. This approach allows us to think about the origin of hue sensation in terms of the chromatic processing within V1, without confounding the two concepts. Yet a theory of color vision must also be cautious of the opposite extreme offered by the physiological perspective — that of conflating the necessary mechanisms for hue processing with measurements of neuronal activity [10]. The current technology of physiological experiments can only tell us what brain regions are activated by chromatic signalling, and to what extent. As a result, the necessary processing has often been attributed to higher-level brain areas [24, 64, 65, 70, 108] and yet unidentified higher-order mechanisms [89, 96, 103].

A central question of color vision research is whether these mechanisms rely on parallel or modular processing to encode stimulus chromaticity [16, 35, 67, 74, 80, 83]. This has often been reframed in terms of anatomical separation, with the assumption that cells responsive to multiple visual features must be involved in the processing mechanisms underlying the perceptual correlate of each [34]. This would mean, for example, that the oriented, color-selective cells described above would be relevant for the perception of both the shape and color of a stimulus. But as argued in [24], we cannot infer relevance on the basis of receptive field properties, as, for instance, such a neuron might use chromatic information primarily to encode the stimulus's spatial properties, indicating a functional separation of spatial and chromatic processing. On the other hand, many experiments have demonstrated the joint processing of stimulus chromaticity and orientation [34, 35].

Similarly, the processing of chromatic and luminance properties is likely multiplexed

[80, 89]. The majority of input to the visual cortex comes from the LGN parvocellular system, whose individual cells encode the L−M pathway, with signals eventually projecting onto the blob regions of V1. However, signals from the parvocellular system also project onto the V1 interblobs and, as a result, the parvocellular cells are believed to carry luminance information for these mostly achromatic target cells [24, 39, 50, 89]. Thus, questions about the modularity of the visual pathway are left unresolved. If signalling about chromaticity is transmitted with information about other visual features, such as brightness, orientation, and spatial frequency, how do these features get teased apart? If not, where is the purported "color center" of the brain [18, 36]?

1.3.2 Multi-Stage Models

Several authors have approached a theory of chromatic processing through combinatorial models which parameterize the weights of the L, M, and S cones contributing to successive stages of neuronal signalling [24, 37, 56, 70, 89]. Though differing in their assumptions of modularity, the theories share a mechanistic framework for the transition of single-cell receptive field properties along the visual pathway [10], starting with cells in the retina and lateral geniculate nucleus (LGN) known to be tuned broadly to the cone-opponent axes and building up to cells in various cortical areas more narrowly tuned to different chromatic directions in DKL space.

The basic framework of these multi-stage models is epitomized by the four-stage model of De Valois et al. [24]. The first stage of this model assumes that the responses of the L, M, and S cones follow the spectral sensitivity diagram (Fig. 1.1) and is thus rooted in the established physiology of visual processing at the level of the retina. The resulting response functions are unitless, representing the relative excitatory or inhibitory effect of a particular wavelength of light on the neurons' responses, rather than the absolute values of their firing rates. In the second stage, the model quantifies cone opponency by assigning weights to the

cone contributions into the inputs of the various cone-opponent cells of the LGN. For the De Valois model, the weights are based on the relative number of cones within the retina and thus assume a direct relationship between the ratio of cones and their contributions to the second processing stage [89]. Furthermore, the model adds an S cone contribution to the input into cells encoding the L−M pathway. Note that this contrasts with the model of Mehrani et al. [70], which assigns the weights based on recordings of LGN cell responses to cone-isolating stimuli that indicate no S cone contribution to the receptive fields of these cells [83].

The third stage of the De Valois framework postulates a mechanism for the mixing of the cardinal cone-opponent systems based on a linear summation of the second-stage LGN signals afferent on the postsynaptic third-stage V1 cells. Thus, each third-stage neuron has a combined input from both of the cone-opponent pathways [23]. In addition, the model assumes modularity by separating out the luminance and chromatic information conveyed by the presynaptic stage-two cells.

Importantly, we take issue with two aspects of this proposed mechanism. First, the model takes the responses of the third-stage neurons to represent the color-opponency of human perception. As such, it associates the zeros of the stage-three neuron response curves with the red, green, yellow, and blue unique hues, contrary to evidence that these hues have no special status at the early stages of vision [103] and that the unbalanced response strengths of an individual opponent neuron's excitatory and inhibitory regions cannot on their own account for the neutralization of two opponent colors [96]. This dovetails with our argument above that assigning a perceptive quality to neuronal responses confounds chromaticity with color sensation [84]. Secondly, while parsimonious, the linear mechanism tunes the cone weights arbitrarily, disregarding the specifics of the real neurons' receptive fields [30, 57, 89].

At the final stage of the model, the stage-three response functions are rectified, which removes their inhibitory (i.e., negative) regions and thereby strips the chromatic signals of

overt opponency. These signals are then combined to reproduce the hue-tuning receptive fields of neurons responsive to stimuli of selective spectral ranges. Interestingly, predictive of future population-based models of cortical processing, De Valois et al. point to the role of network effects in preserving color-opponency at this cortical stage, which is otherwise lost at the level of the individual stage-four hue-tuning cell. Furthermore, the addition of a rectifying nonlinearity reflects the understanding that the linear combinatorial mechanism cannot, on its own, sufficiently explain the variety of color cells observed in the visual cortex [35, 53, 83]. The role of processing nonlinearities in narrowing the selectivity of the hue tuning curves is likewise emphasized in the Mehrani et al. multi-stage model, which also incorporates rectification in the V1 processing stage, in addition to further nonlinearities via the multiplication of these cells' responses at later processing stages [70]. Note, however, that this model does not integrate the two cone-opponent channels until these later stages and therefore does not implicate V1 as the origin of the channel mixing mechanism.

But just how separate are the cortical stages of chromatic processing? Within V1, Hanazawa et al. have demonstrated both "Type 1" neurons preferring hues concentrated around the cardinal axes and "Type 2" neurons with more widely distributed preferences [44]. Notably, the response curves of the latter are best fit by a sigmoidal surface, in agreement with the thresholding nonlinearity proposed above and by the model presented in this dissertation. Similarly, Liu et al. have shown that V1 cells responsive to DKL directions close to the L−M and M−L directions are pooled into separate cortical regions [67]. These findings indicate that processing within the visual cortex relies on the cardinal pathways at least to some extent and, therefore, that the functional integration of the two channels is initiated, but not yet perfected, in V1 [67]. This dissertation thus assumes that the cone-opponent and hue-tuning stages of color processing occur simultaneously, crossing and blurring, rather than sequentially as in the previous multi-stage models [27]. It does so by departing from the stage-wise combinatorial schemes of these models in favor of a nonlinear, population-based

theory of a hue tuning mechanism originating in V1.

1.4 Neural Field Theory

Previous models of cortical visual processing have approached the analysis of the underlying population dynamics through the lens of neural field theory. This theory takes the statistical mechanics approach of describing the complex, multidimensional neuronal interactions by an effective lower-dimensional field of neural connectivity within which the activity dynamics take place.

In the general framework, the multi-layered three-dimensional cortical structure is characterized as a flattened two-dimensional sheet, while the various neurons are grouped by their excitatory or inhibitory postsynaptic effects. Furthermore, given the millions of neurons within V1, and therefore the redundancy in their receptive field structures, the cortical sheet is spatially coarse grained such that each point represents the activity of a large population of neurons. Likewise, these models assume that the relevant dynamics occur on a timescale larger than that of the single-cell level fluctuations and thus average the activity state variables over the latter timescale [19, 100, 101]. As will be described in chapter two, both the state variables used to describe the cortical activity and the timescale over which the governing field equations are temporally coarse grained reflect various modeling assumptions about the physiology and histology of the cortex. For the purposes of this dissertation, I will describe a class of field equations which seek to model the visual cortex as a pattern forming system capable of encoding the various features of vision [5, 6, 7, 8, 9, 13, 32, 45, 85, 88]. The mathematical details of this framework are left to chapter two.

Each of these models generalizes the Wilson-Cowan neural field formulation [14, 100, 101] by replacing its two canonical equations for the excitatory and inhibitory dynamics with a single equation incorporating both. (We note an exception for the model of Smirnova et al., which offers a two-population description of joint orientation and color processing [85].) Fur-

thermore, each reframes the description of the network activity in terms of its feature-based connectivity, in addition to, or in place of, the original distance-based formulation. Thus, the activity of each neuronal population is no longer labeled purely by its position on the cortical sheet, but also by its preferred stimulus in an analogous feature space. The corresponding network topology may be modeled on the cortical histology, such as the orientation map of figure 1.5 or spatial-frequency maps addressed in [6], [7], and [8]. Conversely, it may be based entirely on functional considerations, as for instance in the orientation tuning model of Sompolinksy et al., also known as the Ring Model, which posits a topology based on the experimentally-motivated assumption that populations with similar orientation preferences are maximally connected [3] and on the argument that the important features of such a connectivity are captured by its first-order Fourier components [45].

Importantly, a feature-based model makes certain assumptions regarding the modularity of cortical processing and the basic cortical unit wherein the relevant dynamics take place. For example, the spherical model of orientation and frequency tuning [6, 7, 8] takes the hypercolumn as the central unit of joint, non-modular feature processing. Accordingly, it coarse grains the feature space so that each point encodes the activity of a large neuronal population labeled by both the orientation and frequency preferences of its constituent neurons. Furthermore, because a network encompassing all the preferences is contained within one hypercolumn (i.e., one point in the coarse-grained cortical space), modelers proceeding within this framework may choose to leave off a description of the cortical space connectivity to further reduce the dimensionality of the system.

In contrast, models taking the orientation map as their starting point (e.g., [5] and [9]) decompose the connectivity into a local isotropic term (connecting neurons of all orientation preferences within a hypercolumn) and a long-range anisotropic term (maximally connecting similarly-tuned neurons between different hypercolumns). In this setup, the connectivity is only partially captured by a single hypercolumn, and a complete picture of orientation

tuning cannot be viewed from this local scale alone. The basic cortical structure is thus composed of several hypercolumns, and the emergent activity is labeled by both its orientation preference in feature space as well as its position in cortical space. Yet, the model takes the "modular" perspective in the sense that its feature space is comprised of only one variable (i.e., orientation preference). Notably, the orientation-tuning Ring Model likewise takes this modular approach in treating orientation tuning as an isolated cortical process, but does so at the local scale of a single hypercolumn, as in the spherical model discussed above.

Along with their differing modeling assumptions, the various setups focus on distinct aspects of the dynamics. Several seek to explain hallucinations through the lens of bifurcation theory, wherein a loss of stability of the system's homogeneous steady state leads to the emergence of patterns of cortical activity with symmetries determined by the underlying cortical connectivity [5, 6, 9]. These models make a point to map the cortical activity back to visual space to explain such visual phenomena as those categorized by Heinrich Klüver in his groundbreaking clinical reports of drug-induced hallucinations [59]. Others proceed in the opposite direction, focusing instead on the network tuning curves which emerge in response to a "real" (i.e., light) stimulus [13, 45]. These tend to place a greater emphasis on the evolution of cortical feature tuning and thus yield a more time-dependent description of the network activity.

However, regardless of whether they take a modular or joint, local or long-range, stimulus- or hallucination-driven, and stationary or dynamical approach, none of these feature models impose values on their respective cortical parameters. They therefore put the onus on the network interactions, and not the modeler, to fine-tune the activity patterns and feature tuning curves. Moreover, by removing the focus from the feedforward stream of visual processing, these models lay out a theory in which the necessary mechanisms underlying perception cannot be described solely on the basis of information *inherited* from the LGN, but rely to a large degree on the signalling *emerging* within the cortical stage of processing

[40]. This reconceptualizes the link between physiology and perception from one which is guided by the stage-wise linearity assumed by previous color models to one reflecting the nonlinear population dynamics within the visual cortex. It is within this mechanistic framework that we proceed.

CHAPTER 2

MODEL

In addition to the forward flow of chromatic information through the successive stages of processing, the encoding of color reflects the neuronal dynamics within each. Modelers agree that the next forays into a mechanistic theory of color vision should consider these intracortical circuits, but disagree about where such interactions first become important. This dissertation presents a model of color processing in which intracortical neuronal dynamics within the visual cortex serve as the substrate for hue perception. Drawing on the canonical Wilson-Cowan neural field equations and the Ring Model of orientation tuning, I show that this population approach allows us to account for cells responsive to the full range of DKL directions without the need to fine-tune the input parameters [3, 45, 100, 101]. The threshholding we employ bears in mind the input-response nonlinearities of previous combinatorial models, but zooms out of the single-cell, feedforward interpretation of input as the stimulus-driven LGN afferents to individual neurons. Rather, we model input as the total synaptic current into a population of cells, taking into account both the cone-opponent LGN signals as well as the hue-dependent connectivity between distinct neuronal populations. The resulting demarcation between the cone-opponent and the hue-selective mechanisms in the same population of cells points to the importance of V1 in the transition from chromatic stimulus to color perception. In chapter three I characterize this role by exploring the effects of the model's connectivity parameters and processing nonlinearities on the narrowness and stability of the emergent hue tuning curves. Furthermore, I show that the model is able to explain color sensation in the absence of LGN input and thus exemplifies a biological mechanism of spontaneous pattern formation evoking color hallucinations.

2.1 Dynamical Equation for the Hue Tuning Mechanism

In light of the patchy distribution of color-sensitive cells reported in [62, 66, 68, 78], we model the color map of V1 as a set of neuronal networks, each colocalized with one CO blob region and encoding the chromaticity of its corresponding portion of the visual field. This organization brings to mind the hypercolumnar structure of orientation preference within V1 [51], which, on the basis of its feature-based connectivity properties, allows for the representation of network activity as a function of a localized feature space. Thus, we assume an averaged hue-dependent activity $a(\theta, t)$, where θ represents a direction in the DKL stimulus space, a strictly physiological conception of "hue," separate from the one categorizing color perception. While an object's geometrical properties exist independent of our perception, we cannot say the same thing for color. A photon of wavelength 700 nm striking a retina is no more "red" than any other particle — color is a perceptual phenomenon not yet represented in these first stages of vision. In drawing this distinction, and in agreement with [66] and [102], we give no special status to V1 cells tuned to the DKL directions associated with the unique hues of color-opponent theory, while simultaneously emphasizing the cone-opponent nature of feedforward afferents from the LGN.

The resulting activity $a(\theta, t)$ of a network of hue-preferring cells, expressed as a firing rate in units of spikes/second, is dominated by the membrane properties of its constituent cells, whose membrane potential variations occur on the order of the membrane time constant τ_0, taken to be 1 ms. In the vein of previous neural mean-field models of feature detection [6, 8, 9, 21, 28, 42], and in close analogy to the Ring Model of orientation tuning [3, 45], we let $a(\theta, t)$ evolve according to the single-population firing-rate formulation of the Wilson-Cowan equations:

$$\tau_0 \frac{da(\theta, t)}{dt} = -a(\theta, t) + g[h(\theta, t)], \tag{2.1}$$

where $h(\theta, t)$, the synaptic input, takes into account both excitatory and inhibitory afferents

into a population of cells preferring hue θ, and $g(x)$ is an activation function, described below.

To analyze the relationships between feedforward and recurrent processing and to distinguish between their respective effects on $a(\theta, t)$, we write $h(\theta, t)$ as a sum of the stimulus-driven synaptic input from the LGN and the intracortical input resulting from the hue-dependent network connectivity within V1:

$$h(\theta, t) = h_{\text{ctx}}(\theta, t) + h_{\text{lgn}}(\theta). \tag{2.2}$$

We express the input as the effect of the net synaptic current on the membrane potential of a cell, following the convention of [28]. Thus, $h(\theta, t)$ has units of mV and can take on both positive and negative values, chosen here so that $a(\theta, t)$ typically ranges from 0 to 60 spikes/sec, in agreement with electrophysiological experiments penetrating individual color-responsive cells [15, 53, 61, 98].

The input is converted to a firing rate according to the nonlinear activation function

$$g(h) = \beta \cdot (h - T) \cdot \mathcal{H}(h - T), \tag{2.3}$$

where $\mathcal{H}(x)$ is the Heaviside step function defined as $\mathcal{H}(x) = 1$ for $x > 0$ and zero for $x \leq 0$. By constraining the network activity to levels below 60 spikes/sec, we ignore the effects of neuronal saturation commonly implemented in models of $g(h)$ [3, 28]. Here, T is the threshold potential of a neuron, below which the synaptic input has no effect on the mean firing rate of the network. Interestingly, as a processing feature, this thresholding nonlinearity has been speculated to account for the chromatic responses of individual neurons in V1 [44]. The amplification of these responses, and thus the mean network response, is modulated by β, the neural gain, measured in spike$\cdot$sec^{-1}/mV. We assume that β is adaptive, its value determined by far-ranging internal and external influences, from attentional mechanisms to

hallucinogenic input [33, 71].

2.1.1 Feedforward Input

To parameterize the input, prior work has relied on the direct relationship between cortical feature preferences and properties of the visual stimulus [3, 8]. The activity of cortical neurons labeled, for instance, by their frequency preferences was mapped directly onto a visual space parameterized by the same variable. Our model deviates in this regard by emphasizing that the stimulus's chromatic information is first discretized along the two cone-opponent pathways.

We incorporate this aspect of early processing by projecting the stimulus's DKL space position $\bar{\theta}$ onto the two cardinal axes:

$$\begin{aligned} l &= \cos\bar{\theta} \\ s &= \sin\bar{\theta}. \end{aligned} \tag{2.4}$$

The magnitudes of l and s are thus taken to represent the normalized strengths of the L−M and S−(L+M) cone-opponent signals, respectively. The feedforward input is then given by

$$h_{\text{lgn}} = c(l\cos\theta + s\sin\theta), \tag{2.5}$$

where c is the signal strength, or contrast, expressed as the mean postsynaptic *coarse* membrane potential (in units of mV, as explained below) of the target hue population generated by the presynaptic LGN neurons. Formulated in this way, the input captures the colocalization of cone-opponency and hue selectivity in the activity of V1 cells as observed in [66] and [105]. With this setup, the hue-tuning networks, parameterized by θ, are not only responsive to the individual cone-opponent stimulus signals, l and s, but also implement the combinatorial mechanisms by which they are first mixed [23]. Substituting in the expressions for l

and s into 2.5, we obtain

$$h_{\text{lgn}} = c\cos(\theta - \bar{\theta}). \tag{2.6}$$

With this form, we point out the similarity of our combinatorial scheme to that of [70], in which the input from cone-opponent V2 cells into hue-tuning V4 cells is weighted as a function of the difference in their preferred hue angles. Most evidently, we differ from this model by first combining the cone-opponent signals in V1 rather than V4, in accordance with the studies described in chapter one. But beyond pointing to V1 as the origin of mixing, these experiments indicate that the combinatorial feedforward scheme is not sufficient to account for the variability of neuronal hue preferences. Reference [66] showed, for instance, that the contribution of signals isolating the S−(L+M) pathway is too small to explain the shifting of hue preferences away from the L−M axis by purely combinatorial means. As put forward in chapter one, a more complete understanding of neuronal hue encoding within V1 requires us to consider the nonlinear population dynamics therein [63, 83, 98].

2.1.2 Recurrent Interactions

We begin by characterizing the connectivity of the target hue tuning populations with a translation-invariant cortical connectivity function $w(|x - x'|)$, such that the interactions between neurons in a single CO blob (length scale $\sim$ .5 mm) depend only on the cortical distance between them [11, 78]. The network's connectivity comprises the interactions of both its excitatory and inhibitory populations,

$$w(|x - x'|) = w_{\text{exc}} + w_{\text{inh}}, \tag{2.7}$$

each of which we model as a sum of an isotropic and distance-dependent term:

$$w_{\text{exc}} = E_0 + E_1 \cos(|x - x'|)$$
$$w_{\text{inh}} = -I_0 - I_1 \cos(|x - x'|). \tag{2.8}$$

We set $E_0 \geq E_1 > 0$ and $I_0 \geq I_1 > 0$ so that w_{exc} and w_{inh} are purely excitatory and inhibitory, respectively, in accordance with Dale's Law [3, 21].

Next, we map the connectivity function onto hue space, drawing from the hue-tuning micro-architecture revealed by the imaging studies of [66], [67], and [105] (see Fig. 1.7). Thus, in a similar manner to the local feature processing models of [3] and [8], we model the CO blob as a single color-processing unit consisting of N neurons labeled by the continuous hue preference variable $\theta \in [-\pi, \pi]$ [8]. To describe the spatial organization of their hue preference data, [67] and [105] applied a linear hue metric of the form $d(\Delta\theta) = a + b\Delta\theta$, where d represents the cortical distance between two populations preferring hue stimuli $\Delta\theta \equiv |\theta - \theta'|$ apart in DKL space. Note, this choice of metric implies a discontinuity between $\theta = 0$ and $\theta = 2\pi$, allowing for the 2π periodicity of the hue preference label. Liu et al. report that the metric was able to capture the micro-organization of 42% of their tested hue maps [67], and a regression performed by Xiao et al. on an individual hue map gave $R^2 = .91$ [105].

In agreement with these findings, we let $|x - x'| = |\theta - \theta'|$, absorbing the constants a and b into the connectivity strength values E_0, E_1, I_0, and I_1 in 2.8. Substituting this change of variables and setting $J_0 = E_0 - I_0$, $J_1 = E_1 - I_1$ (measured in mV/spike·sec^{-1}) gives

$$w(|\theta - \theta'|) = J_0 + J_1 \cos(|\theta - \theta'|). \tag{2.9}$$

As detailed in Fig. 2.1, this functional form captures the local excitation and lateral inhibition connectivity ansatz typically assumed in neural field models as an analogy to diffusion-

driven pattern formation [1, 5, 49, 58, 94]. Further, the function is even in $\Delta\theta$, and we drop the absolute value in the remaining text. Notably, we posit that neurons in close proximity in both cortical and hue space maximally excite each other, and those separated by $\Delta\theta = \pi$ mutually inhibit each other, evoking the hue-opponency of perception on a cellular level.

Here, it is important to distinguish between the connectivity function and the center-surround receptive fields of single- and double-opponent color cells [83]. While the structures of both can be approximated by the same functional form, the resemblance is superficial: the former characterizes the interactions between different neuronal populations, and the latter is a property of single cells, often adapted for computer vision algorithms [87, 95].

Finally, we weigh the influence of the presynaptic cells by convolving the connectivity function with the network activity, arriving at the cortical input to the target hue population at time t:

$$h_{\text{ctx}}(\theta, t) = \int_{-\pi}^{\pi} w(\theta - \theta')a(\theta', t)d\theta'. \tag{2.10}$$

The recurrent input is thus a continuous function in θ, derived from the population-level interactions. As put forward by the above-mentioned imaging studies, these interactions are colocalized with the cone-opponent feedforward input, h_{lgn}, within the same CO blob regions of V1. Collectively, our formulation of $h(\theta, t)$ implements the mixing posited by these experiments, without requiring us to arbitrarily fine-tune the relative weights of the afferent signals.

Finally, for analytical purposes, we will also consider the unrectified version of the model:

$$\tau_0 \frac{da(\theta, t)}{dt} = -a(\theta, t) + \beta(h(\theta, t) - T). \tag{2.11}$$

This linear version applies to the parameter regime in which the net input $h(\theta, t)$ is always above threshold and will be addressed in chapter three.

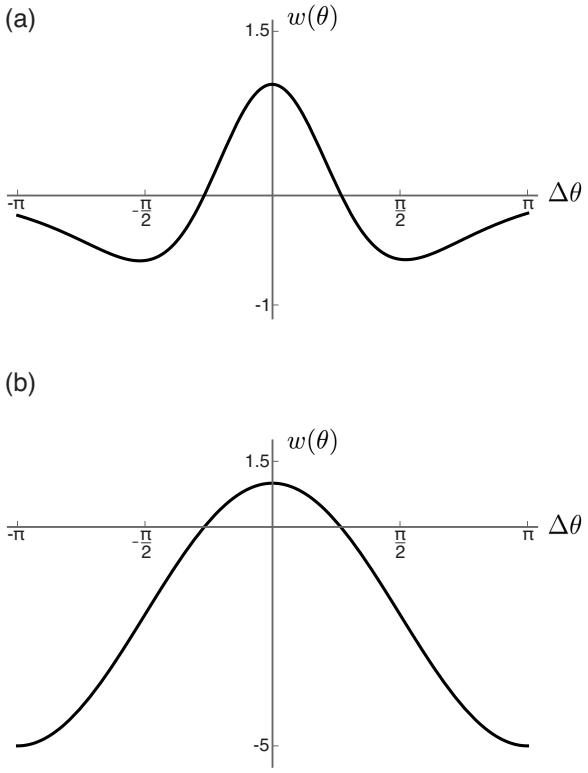

Figure 2.1: Cortical connectivity functions. (a) A difference of two Gaussians, one characterizing the excitatory interactions (here with $\sigma_E = 40°$) and the other the inhibitory interactions ($\sigma_I = 90°$). This is the connectivity typically assumed in mean field models of cortical processing. (b) The difference of cosines formulation (2.9), with $J_0 = -2$ and $J_1 = 3$, captures the local excitation and lateral inhibition assumed in (a).

2.2 Overview of Unit Conventions

Although each of the network models introduced in section 1.4 seeks to represent the population activity based on a generalized Wilson-Cowan equation, their varying unit conventions reflect different physiological assumptions. Thus, a brief overview of these conventions is in order, followed by a description of the unit choices made here.

2.2.1 Voltage-Based vs. Current-Based Models

As representations of the mean population activity, neuronal network models must make certain assumptions with respect to their constituent neurons. In this regard, there are two alternative assumptions in modeling the response of a postsynaptic cell to its net input [21, 28]. The *current-based model* assumes that the network dynamics are dominated by the synaptic properties of the afferent connections, that is, by the synaptic current (in units of mA) generated by the presynaptic cells. The time constant, τ_0, in this case describes the decay of the synaptic current, whose value depends on the length and conductance of the dendrites [21]. The Wilson-Cowan equation, thus reads:

$$\tau_0 \frac{dI_j(\theta,t)}{dt} = -I_j(\theta,t) + \sum_i w_i a_i(\theta,t), \tag{2.12}$$

where i and j represent the presynaptic and postsynaptic neurons, respectively. Here, the net input into the network is the sum of presynaptic activity (both recurrent and external), weighted by the synaptic strengths w_i, and is described in terms of its effects on the synaptic current I_j, referred to in the literature as the net synaptic input [21] or synaptic drive [14, 28]. The activation function may be then applied to the current at any point in the dynamics to determine the activity of the pre- and post-synaptic neurons, i.e.,

$$a(\theta,t)_{i,j} = g(I_{i,j}). \tag{2.13}$$

Note that if $I_i(\theta,t)$ represents a synaptic input from recurrent connections, it is equivalent to the current of the postsynaptic neurons, $I_j(\theta,t)$. Otherwise, one would need to determine I_i, and the corresponding a_i, through a separate application of 2.12, where now the previously presynaptic neurons are postsynaptic to their own input.

More commonly, modelers adopt the *voltage-based model* in which the assumption is that the network dynamics are governed by the membrane properties of the postsynaptic cells

[1, 3, 8, 9, 13, 45, 47]. In this case, τ_0 represents the membrane time constant, the time scale of the membrane potential fluctuations. Note that this is the modeling assumption of the 1973 Wilson-Cowan formulation, in which the temporal coarse graining requires that the relevant network dynamics are captured at a timescale greater than or equal to τ_0 [101]. It is also the assumption we make here.

In its most general form [28] as applied to our hue model, the *voltage-based model* reads:

$$\tau_0 \frac{dV_j(\theta,t)}{dt} = -V_j(\theta,t) + \sum_i w_i a_i(\theta,t), \tag{2.14}$$

with the activation function now taking the voltage as its input,

$$a(\theta,t)_{i,j} = g(V_{i,j}). \tag{2.15}$$

As before, $V_i(\theta,t) = V_j(\theta,t)$ if the input is recurrent. This is the variation adopted, for instance, by [1] and [13].

From 2.12 and 2.14, it looks as if the main difference between the two models is in the state variable representing the network dynamics. It may seem surprising, therefore, to find that the most common variation of the voltage-based model [21, 29, 45, 101], as well as the model presented here, takes $a(\theta,t)$ as the state variable. Neglecting the details of the input term, these models take the form:

$$\tau_0 \frac{da_j(\theta,t)}{dt} = -a_j(\theta,t) + g(I_i), \tag{2.16}$$

with

$$I_i = \sum_i w_i a_i(\theta,t), \tag{2.17}$$

such that the synaptic weights are taken into account before the activation function is applied

and I represents the net synaptic current afferent on the neuronal network. We will call this the *firing rate formulation* of the voltage-based model, though it should not be confused with the current-based model, whose dominant timescale differs from the voltage-based model as explained above.

It is sometimes presumed that whether the weights are part of the argument to g as in 2.16 or multiply its output as in 2.12 marks the main difference between the voltage-based and current-based models. However, note that the other variation of the voltage-based model (2.14) also applies the weights post-rectification, while [42] features a current-based model in which the summation is applied before. Thus, these variations are more of a reflection of the various unit conventions adopted than the physiological assumptions the modelers have made [14, 28]. We emphasize that the latter are embodied in the definitions of the time constant (membrane vs. synaptic) as opposed to the specific state variable (V, a, or I) used.

2.2.2 Unit Choices

Among the various firing-rate formulations (wherein the state variable is a) there are two typical unit conventions for the current and activity. If a is measured in spikes/sec and I in mA, it must be assumed that the current is multiplied by a constant which converts its units to those of a firing rate [21]. Correspondingly, the synpatic weights, w_i, of 2.17 are dimensionless. This convention, however, confounds the definitions of current and activity, as the input to the activation function is now in units of spikes/sec. Other formulations avoid such considerations by making all variables dimensionless. This is the approach adopted by the orientation tuning model, wherein the activity variable ranges from 0 to 1, with 1 representing a firing rate on the order of 1000 spikes/sec [45]. Similarly, the activity variable may represent the proportion of active neurons [101] or the probability of activation [28], both dimensionless quantities.

Although our color model, too, is built on a firing-rate formulation of the voltage-based

model, it departs from both of these unit conventions. To characterize the unit choices made here, it is important to note again that the activity variable $a(\theta, t)$ is the average firing rate of a large population of hue cells. Correspondingly, each of the quantities discussed below are averaged across all the neurons in the relevant populations. Here, we express the variables in their natural units to avoid any ambiguity in the physiological quantities they represent.

As in the voltage formulation, we have expressed the input as the net effect of the afferent connections on the population-averaged membrane potential of the target hue cells. We make this choice because at the single-cell level, the threshold potential, T, indicates the value of the membrane *potential* at which the cell begins to fire. Although the ensuing action potentials are identical, their frequency — the neuron's firing rate — increases with larger values of the *coarse membrane potential*, obtained by removing the spikes from the full voltage traces [12]. The coarse membrane potential during a signal's duration is therefore a measure of its magnitude, as illustrated in figure 2.2.

For the recurrent signal, this convention requires us to express the cortical strengths, J_0 and J_1, in units of mV/spike·sec^{-1}, such that convolution with the activity gives us units of voltage. On the other hand, in our formulation of the LGN input, c multiplies the dimensionless DKL projections and is therefore itself measured in mV. Thus, we note that while the cortical strengths are the equivalent of the presynaptic weights w_i in the general rate equation (2.16), the relative influences of the presynaptic LGN cells are modulated by the projections themselves, and the stimulus strength is consequently not interpreted as a proper "weight." These two types of strengths are therefore measured differently from each other, and differently from the conventions described above (see [13] for a similar convention within the voltage formulation framework). Finally, in building the color model with g as in 2.3, we have assumed a linear relationship between the network averages for coarse membrane potential and activity, with a slope given by β, in units of spike·sec^{-1}/mV.

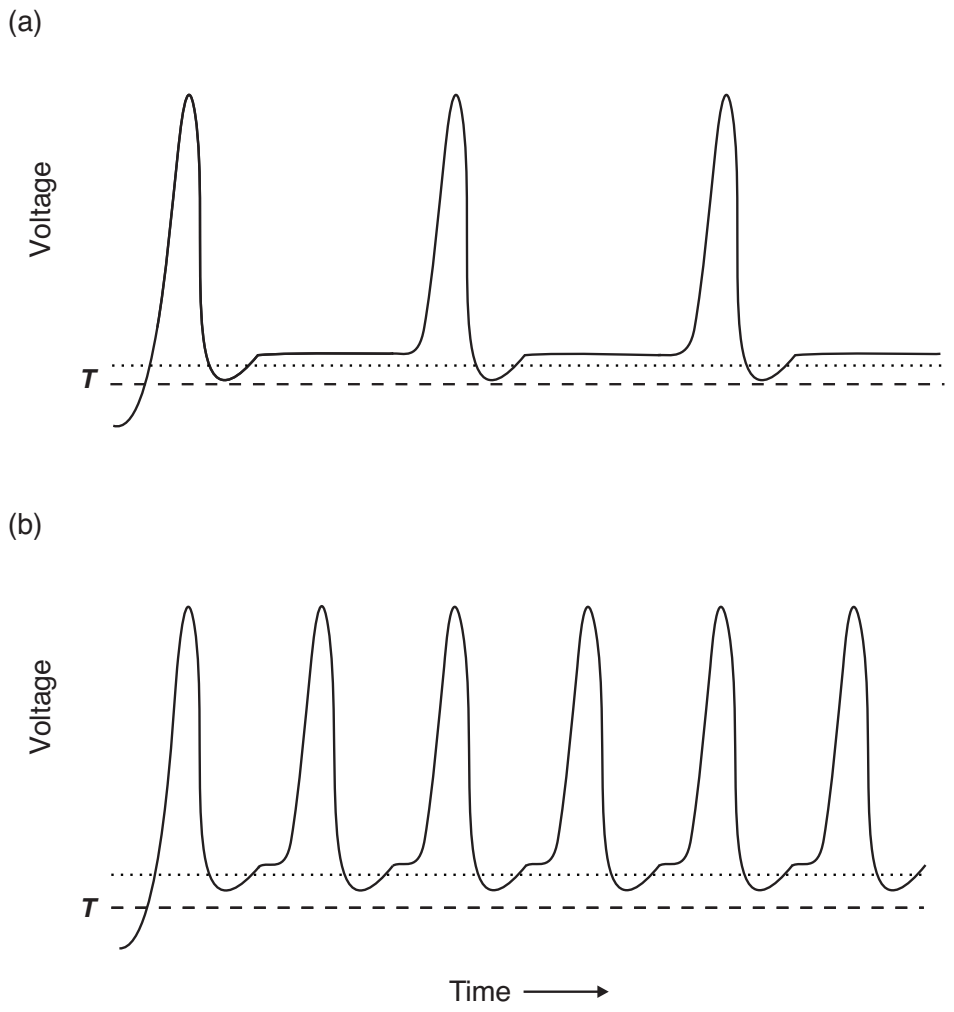

Figure 2.2: Firing rate of a neuron in response to constant inputs of different strengths. (a) An input, represented as the average coarse membrane potential (dotted line) of the target cells, results in a firing rate if it exceeds the threshold potential (dashed line). (b) For a larger input, and larger corresponding coarse membrane potential, the firing rate increases. The coarse membrane potential is further averaged across all neurons in the network, yielding $h(\theta, t)$.

CHAPTER 3

METHODS AND RESULTS

The solution to our rate equation models the formation of hue tuning curves in V1. In this context, a prevailing approach of previous neural-field feature models has been to assume a steady-state solution from whose properties they glean the defining features of the recurrent and feedforward interactions [3, 8]. Similarly, models of spontaneous pattern formation posit a steady-state solution which, with the onset of a Turing-like instability, bifurcates into new steady states representative of spontaneous activity patterns [6, 9]. However, the emphasis on the emergent steady state largely ignores the nonlinear dynamics underlying its formation.

Here, I analyze the full time-dependent solution to highlight the role of our model's nonlinearity at each point in the formation of the steady-state hue tuning curves. This leads to a discussion of the **analytical regime**, which permits a closed-form solution. I then present the numerical steady-state solution with which I characterize the roles of the gain, threshold, input strength, and cortical strength parameters in the mechanisms underlying V1's encoding of hue. This is followed by a comparison to the orientation tuning model and a numerical stability analysis of the emergent steady-state tuning curves, in which I describe the role of the nonlinearity in expanding the stable parameter regime. Finally, I show that our model is capable of explaining color responses in the absence of visual stimuli via a Turing-like mechanism of biological pattern formation.

3.1 Time-Dependent Solution

We start by observing that by virtue of the invariance of $w(\theta - \theta')$ under translations of θ, the convolution operator $T_w \rightarrow w * f(\theta) = \int_{-\pi}^{\pi} w(\theta - \theta') f(\theta') d\theta'$ is diagonalizable by the Fourier eigenfunction basis

$$\hat{e}_\mu(\theta) = \frac{1}{\sqrt{2\pi}} e^{i\mu\theta} \tag{3.1}$$

with $\mu \in \mathbb{N}$ and $\hat{e}_\mu$ normalized to integrate to 1 on $[-\pi, \pi]$. To determine the eigenvalues λ_μ of the corresponding linear transformations,

$$\int_{-\pi}^{\pi} d\theta' w(\theta - \theta') \frac{1}{\sqrt{2\pi}} e^{i\mu\theta'} = \lambda_\mu \frac{1}{\sqrt{2\pi}} e^{i\mu\theta}, \tag{3.2}$$

we make the change of variables $\theta - \theta' = \phi$, so that the left-hand side of 3.2 can be rewritten as

$$-\int_{\theta+\pi}^{\theta-\pi} d\phi\, w(\phi) e^{-i\mu\phi} \frac{1}{\sqrt{2\pi}} e^{i\mu\theta} = \int_{-\pi}^{\pi} d\phi\, w(\phi) e^{-i\mu\phi} \frac{1}{\sqrt{2\pi}} e^{i\mu\theta}. \tag{3.3}$$

The eigenvalues are thus:

$$\lambda_\mu = \int_{-\pi}^{\pi} d\phi\, w(\phi) e^{-i\mu\phi}. \tag{3.4}$$

Next, we assume $a(\theta, t)$ is separable in t and θ and bounded on $[-\pi, \pi]$ so that we may expand it in the eigenbasis of the convolution operator as:

$$a(\theta, t) = \sum_\mu c_\mu(t) \hat{e}_\mu(\theta). \tag{3.5}$$

Substituting the expansion into 2.10, we have for 2.2

$$h(\theta, t) = \sum_\mu c_\mu(t) \int_{-\pi}^{\pi} w(\theta - \theta') \hat{e}_\mu(\theta') d\theta' + h_{\text{lgn}}(\theta), \tag{3.6}$$

where $w(\theta - \theta')$ is our choice for the connectivity function (2.9) and $h_{\text{lgn}}(\theta)$ is defined as in 2.6. Evaluating the integrals, we obtain

$$h(\theta,t) = \lambda_{\text{-}1}\, c_{\text{-}1}(t)\, \hat{e}_{\text{-}1}(\theta) + \lambda_0\, c_0(t)\, \hat{e}_0(\theta) + \lambda_1\, c_1(t)\, \hat{e}_1(\theta) + c\cos(\theta - \bar{\theta}) \tag{3.7}$$

with $\lambda_0 = 2\pi J_0$ and $\lambda_1 = \lambda_{\text{-}1} = \pi J_1$.

Note here that only the zeroth and first-order complex Fourier components remain.

3.1.1 Thresholding Nonlinearity

So far, we have only been concerned with the linear transformations of $a(\theta,t)$ and that of its eigenfunction expansion under the action of the convolution operator. The nonlinearity of the model comes into play when we recall the thresholding property of the activation function in the context of the full rate dynamics.

Substituting in the expansion 3.5 and the explicit form of the activation function 2.3 into 2.1 yields:

$$\tau_0 \sum_{-\infty}^{\infty} \frac{dc_\mu(t)}{dt} \hat{e}_\mu(\theta) = -\sum_{-\infty}^{\infty} c_\mu(t)\hat{e}_\mu(\theta) + \beta\big(h(\theta,t) - T\big)\mathcal{H}\big(h(\theta,t) - T\big). \tag{3.8}$$

In the absence of the nonlinearity (2.11), each of the eigenmodes $\hat{e}_\mu(\theta)$ would evolve independently of the others, and a complete analysis of the time-dependent system would seek to solve a set of equations for $c_\mu(t)$. However, in our setup, the thresholding introduces a coupling of these coefficients, as the critical hue angle at which the input is cut off is determined by the combined $c_\mu(t)$ at each point in time. While an analytical solution to this system is in most cases intractable, it is nonetheless informative to break down the rate equation into a coupled system of equations for the evolution of the coefficients $c_\mu(t)$. Taking the inner product of 3.8 with $\hat{e}_\nu$ and using $\langle \hat{e}_\nu | \hat{e}_\mu \rangle = \delta_{\mu\nu}$, we obtain:

$$\begin{aligned} \tau_0 \frac{dc_\nu(t)}{dt} &= -c_\nu(t) + \langle \hat{e}_\nu | \beta\big(h - T\big)\mathcal{H}\big(h - T\big)\rangle \\ &= -c_\nu(t) + \tilde{g}_\nu\big(\tilde{h}_\nu(h)\big) \end{aligned} \tag{3.9}$$

where $\tilde{g}_\nu\big(\tilde{h}_\nu(h)\big)$ represents the effect of the nonlinear activation function g on the νth coefficient of the input, $\tilde{h}_\nu \equiv \langle \hat{e}_\nu | h \rangle$.

Note here that the coupling of the coefficients c_ν introduced by the nonlinearity means that $\tilde{g}_\nu(\tilde{h}_\nu) \neq g(\tilde{h}_\nu) \equiv \beta(\tilde{h}_\nu - T)\mathcal{H}(\tilde{h}_\nu - T)$. That is, the effect of the thresholding nonlinearity on the evolution of c_ν is not simply the application of the original activation function directly onto the corresponding $\tilde{h}_\nu$. Since the Heaviside formulation in 3.9 is a function of the net input $h \neq \tilde{h}_\nu$, we cannot determine $\tilde{g}_\nu(\tilde{h}_\nu)$ in a stepwise manner, first computing the inner product to determine $\tilde{h}_\nu$ and then cutting off the contributions where $\tilde{h}_\nu < T$.

Hansel and Sompolinksy [45] have addressed this complexity by directing the analysis to the final steady state of the activity, wherein $a(\theta) = g\big(h(\theta)\big)$. This simplifies the mathematics by allowing us to solve for c_ν with a linear version of the firing rate equation (2.11) and then cutting off the resultant activity profile at values below threshold. However, as mentioned above, this simplification does not allow us to examine the dynamics of the network in full. Alternatively, Carandini and Ringach [13] use a voltage-based Wilson-Cowan equation (2.14) and solve for the dynamics numerically, obtaining the activity profile at each timestep by applying the thresholding nonlinearity to $V(t)$. Their numerical analysis does yield a complete picture of the network activity's evolution over time, but does not provide an analytic framework for these dynamics.

Here, we keep to our firing rate formulation as described in section 2.2, but seek to characterize the effect of the thresholding nonlinearity on the coupled $c_\nu(t)$ at each point throughout the network's evolution. This requires us to reformulate $\tilde{g}_\nu(\tilde{h}_\nu)$ in 3.9. To do so, we recall that the effect of the net activation function $g(h)$ is to cut off the input for values below T. We can thus rewrite its Heaviside formulation in terms of the critical cutoff angles $\delta_1(t)$ and $\delta_2(t)$, symmetric about the peak of the $h(\theta, t)$ curve. The time dependence of the cutoff angles reflects the evolution of this curve, which requires that the thresholding be carried out continuously throughout the duration of the dynamics.

From here, we can compute $\tilde{g}_\nu(\tilde{h}_\nu)$ by evaluating the inner product of $h(\theta,t)$ with $\hat{e}_\nu(\theta)$, restricting the limits of integration to $\{\delta_1(t),\delta_2(t)\}$:

$$\tilde{g}_\nu\big(\tilde{h}_\nu(h)\big) = \beta\,\langle \hat{e}_\nu(\theta)|h(\theta,t)\rangle = \beta\int_{\delta_1(t)}^{\delta_2(t)} h(\phi,t)\hat{e}_\nu^*(\phi)d\phi. \tag{3.10}$$

Thus, the contribution of h_ν to the evolution of c_ν is cut off by $\tilde{g}_\nu$ at the critical angles $\{\delta_1(t),\delta_2(t)\}$, themselves determined by the shape of h and not h_ν. This means that the coupling of the individual c_ν via the thresholding nonlinearity is in fact prescribed by the net input.

To determine δ_1 and δ_2 in 3.10, we must reformulate the Heaviside as a function of θ. For mathematical convenience (see Appendix A), we first rewrite 3.7 in terms of c_0, $\mathrm{Re}(c_{\text{-}1})\equiv c_{\text{-}1}^R$, and $\mathrm{Im}(c_{\text{-}1})\equiv c_{\text{-}1}^I$ as

$$h(\theta,t) = \frac{\lambda_0\,c_0(t)}{\sqrt{2\pi}} + \left(cl + \sqrt{\tfrac{2}{\pi}}\lambda_{\text{-}1}\,c_{\text{-}1}^R(t)\right)\cos(\theta) + \left(cs + \sqrt{\tfrac{2}{\pi}}\lambda_{\text{-}1}\,c_{\text{-}1}^I(t)\right)\sin(\theta). \tag{3.11}$$

Setting

$$\begin{aligned} q_{\mathrm{R}} &= cl + \sqrt{\tfrac{2}{\pi}}\lambda_{\text{-}1}\,c_{\text{-}1}^R(t) \\ q_{\mathrm{I}} &= cs + \sqrt{\tfrac{2}{\pi}}\lambda_{\text{-}1}\,c_{\text{-}1}^I(t) \\ q_0 &= \frac{\lambda_0\,c_0(t)}{\sqrt{2\pi}} \end{aligned} \tag{3.12}$$

the input takes the form

$$h(\theta,t) = q_0(t) + c_h(t)\cos[\theta+\gamma(t)] \tag{3.13}$$

where $\tan(\gamma) = -\frac{q_{\mathrm{I}}}{q_{\mathrm{R}}}$ and $c_h(t) = \sqrt{q_{\mathrm{R}}^2 + q_{\mathrm{I}}^2}$ as shown in Appendix A.

The Heaviside can then be expressed as

$$\begin{aligned}\mathcal{H}\big[h-T\big] &= \mathcal{H}\big[q_0 + c_h\cos(\theta+\gamma) - T\big] \\ &= \mathcal{H}\left[\cos(\theta+\gamma) - \alpha\right] \end{aligned} \tag{3.14}$$

where $\alpha \equiv \frac{T-q_0}{c_h}$, and the time arguments are suppressed for simplicity. In this formulation, the Heaviside sets the limits of integration in 3.10 as the angles $\theta = \delta_1, \delta_2$ where α intersects with $\cos(\theta+\gamma)$, as shown in Fig. 3.1 below.

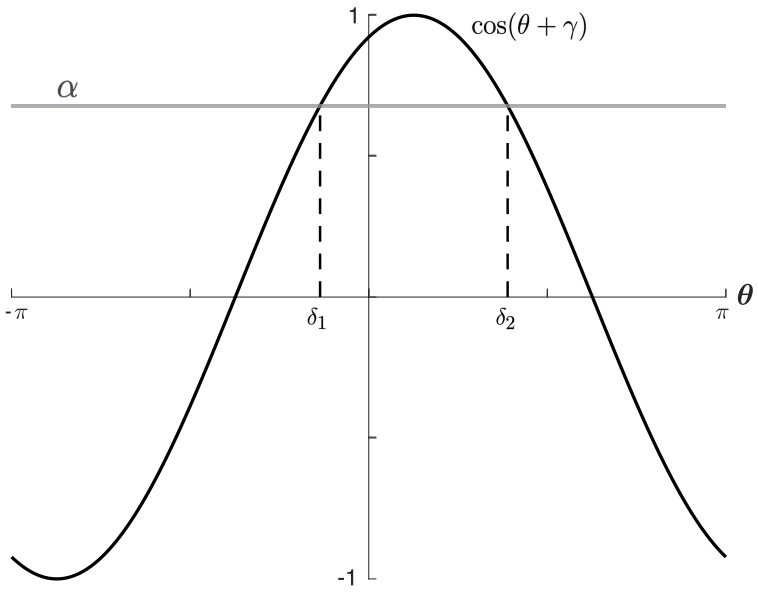

Figure 3.1: The limits of integration δ_1 and δ_2 in 3.10 are the angles corresponding to the intersection of α (in gray) and $\cos(\theta+\gamma)$ (in black). Here, $c = 1$, $\beta = 1$, and $T = -1$. $\bar{\theta} = \pi/8$. J_0 and J_1 are as in Fig. 2.1.

3.1.2 System of Equations

With the reformulation of $\tilde{g}_\nu(\tilde{h}_\nu)$, the system of equations for the evolution of the coupled c_ν (3.9) takes the more explicit form:

$$\tau_0 \frac{dc_\nu(t)}{dt} = -c_\nu(t) + \beta \int_{\delta_1}^{\delta_2} \left[q_0(t) + c_h(t)\cos[\phi + \gamma(t)]\right] \hat{e}_\nu^*(\phi) d\phi, \tag{3.15}$$

where I have substituted 3.13 into 3.10 and δ_1, δ_2 are obtained according to the formalism above. Note that, for all c_ν, the integrand of 3.15 is a function of q_0, c_h, and γ, and therefore, implicitly, only of the coefficients $c_0(t)$, $c_{\text{-}1}(t)$, and $c_1(t)$. Thus, the dynamics are determined in full by the evolution of $c_{|\nu|\leq 1}(t)$:

$$\begin{aligned}
\tau_0 \frac{dc_0(t)}{dt} &= -c_0(t) + \frac{\beta}{\sqrt{2\pi}} \int_{\delta_1}^{\delta_2} \left[q_0(t) + c_h(t)\cos[\phi + \gamma(t)]\right] d\phi \\
\tau_0 \frac{dc_1(t)}{dt} &= -c_1(t) + \frac{\beta}{\sqrt{2\pi}} \int_{\delta_1}^{\delta_2} \left[q_0(t) + c_h(t)\cos[\phi + \gamma(t)]\right] e^{-i\theta}(\phi) d\phi \\
\tau_0 \frac{dc_{\text{-}1}(t)}{dt} &= -c_{\text{-}1}(t) + \frac{\beta}{\sqrt{2\pi}} \int_{\delta_1}^{\delta_2} \left[q_0(t) + c_h(t)\cos[\phi + \gamma(t)]\right] e^{i\theta}(\phi) d\phi.
\end{aligned} \tag{3.16}$$

Separating 3.44 into its real and imaginary parts, and noting that a real-valued activity profile $a(\theta, t)$ requires $c_0 \in \mathbb{R}$ and $c_1 = -c_{\text{-}1}^*$, reduces the system to a set of equations for $c_0(t)$, $c_{\text{-}1}^R(t)$, and $c_{\text{-}1}^I(t)$.

Evaluating the integrals, we obtain:

$$\begin{aligned}
\tau_0 \frac{dc_0(t)}{dt} &= -c_0(t) + \tfrac{\beta}{\sqrt{2\pi}} \Big\{ c_h \big[\sin(\delta_2 + \gamma) - \sin(\delta_1 + \gamma) \big] + (T - q_0)(\delta_1 - \delta_2) \Big\} \\
\tau_0 \frac{dc_{\text{-}1}^R(t)}{dt} &= -c_{\text{-}1}^R(t) + \tfrac{\beta}{\sqrt{2\pi}} \Big\{ \tfrac{c_h}{2} \big[\cos\gamma(\delta_2 - \delta_1) + \cos(\gamma + \delta_1 + \delta_2)\sin(\delta_2 - \delta_1) \big] \\
&\qquad + (T - q_0)(\sin\delta_1 - \sin\delta_2) \Big\} \\
\tau_0 \frac{dc_{\text{-}1}^I(t)}{dt} &= -c_{\text{-}1}^I(t) + \tfrac{\beta}{\sqrt{2\pi}} \Big\{ \tfrac{c_h}{2} \big[\sin\gamma(\delta_1 - \delta_2) + \sin(\gamma + \delta_1 + \delta_2)\sin(\delta_2 - \delta_1) \big] \\
&\qquad + (T - q_0)(\cos\delta_2 - \cos\delta_1) \Big\},
\end{aligned} \tag{3.17}$$

where the time arguments of q_0, c_h, γ, δ_1, and δ_2 are suppressed for clarity.

Written in this form, the system provides a representation of the time evolution of $a(\theta, t)$ in terms of the coupled evolution of the constants $c_{|\nu|\leq 1}$. It is important to note that these equations are nonlinear due to the implicit Heaviside in our determination of $\delta_1(t)$ and $\delta_2(t)$. While our reformulation of the right-hand side of 3.9 allows for the explicit representation of the coupling of c_ν via the nonlinearity, it is also this coupling which proves the analytical solution of the trajectories intractable. Thus, to analyze the behavior of the time-dependent solution, I turn next to a description of the phase portrait of the system (see chapter six of [91] for an in-depth treatment of nonlinear phase plane analysis).

3.2 Steady-State Solution

Expressing 3.17 in the form of the general vector field, we have:

$$\begin{aligned}
\tau_0 \frac{dc_0(t)}{dt} &= f_1(c_0, c_{\text{-}1}^R, c_{\text{-}1}^I) \\
\tau_0 \frac{dc_{\text{-}1}^R(t)}{dt} &= f_2(c_0, c_{\text{-}1}^R, c_{\text{-}1}^I) \\
\tau_0 \frac{dc_{\text{-}1}^I(t)}{dt} &= f_3(c_0, c_{\text{-}1}^R, c_{\text{-}1}^I),
\end{aligned} \tag{3.18}$$

which captures the fact that $q_0(t)$, $c_h(t)$, $\gamma(t)$, $\delta_1(t)$, and $\delta_2(t)$ are completely determined by the coefficients $c_{|\nu|\leq 1}(t)$.

The coefficients of the steady-state hue tuning curve, $a_\infty(\theta)$, then satisfy $\boldsymbol{f(c^*)} = 0$, that is:

$$\begin{aligned}
f_1(c_0, c_{\text{-}1}^R, c_{\text{-}1}^I) &= 0 \\
f_2(c_0, c_{\text{-}1}^R, c_{\text{-}1}^I) &= 0 \\
f_3(c_0, c_{\text{-}1}^R, c_{\text{-}1}^I) &= 0.
\end{aligned} \tag{3.19}$$

To solve this system of equations for the steady-state values of c_ν, we must first determine the values of the angles δ_1, δ_2, and γ at the steady state. This is best approached by considering the generic shape of the activity profile itself, specifically in terms of the angles corresponding to its peak and cutoff values.

3.2.1 Evolution of Peak Angle

We first assume that upon receiving a stimulus $\bar{\theta}$ at time $t = 0$, the network has a random spontaneous firing rate $a(\theta, 0)$. Using 3.5, we expand the activity profile in terms of the initial values of the corresponding coefficients $c_\nu(0)$:

$$\begin{aligned} a(\theta,0) &= \sum_{\mu} c_\mu(0)\hat{e}_\mu(\theta) \\ &= \frac{1}{\sqrt{2\pi}}c_0(0) + \frac{1}{\sqrt{2\pi}}\sum_{\mu\geq 1}\big(2c^R_{\text{-}\mu}(0)\cos(\mu\theta) + 2c^I_{\text{-}\mu}(0)\sin(\mu\theta)\big) \\ &= \frac{1}{\sqrt{2\pi}}c_0(0) + \frac{1}{\sqrt{2\pi}}\sum_{\mu\geq 1} 2[r_\mu(0)\cos(\mu\theta - \phi_\mu(0))] \end{aligned} \tag{3.20}$$

with $\tan(\phi_\mu) = \frac{c^I_{\text{-}\mu}}{c^R_{\text{-}\mu}}$ and $r^2_\mu = (c^I_{\text{-}\mu})^2 + (c^R_{\text{-}\mu})^2$ such that $\phi_\mu(0)$ are completely determined by the initial conditions. Thus, at $t = 0$ the activity profile is composed of an infinite sum of cosine functions, each peaked about a corresponding disparate angle ϕ_μ, and therefore has no discernible peak. To characterize the evolution of the network activity from these initial conditions to its hue tuning profile at $t \to \infty$, we seek to obtain the steady-state values of ϕ_μ and the corresponding tuning curve peak inductively as follows.

Let us first take $\mu = 1$. As seen in Fig. 3.1, we note that $\delta_1(t)$ and $\delta_2(t)$ are symmetric about $\gamma(t)$ such that $\delta_2 + \gamma = 2\pi - (\delta_1 + \gamma)$. Using this symmetry, we factor out $\cos(\gamma)$ and

$\sin(\gamma)$ respectively in the equations for c_{-1}^R and c_{-1}^I of 3.17:

$$\begin{aligned}\tau_0 \frac{dc_{-1}^R}{dt} &= -c_{-1}^R + \tfrac{\beta}{\sqrt{2\pi}} F_1 \cos\gamma \\ \tau_0 \frac{dc_{-1}^I}{dt} &= -c_{-1}^I - \tfrac{\beta}{\sqrt{2\pi}} F_1 \sin\gamma \end{aligned} \tag{3.21}$$

with

$$F_1 = \tfrac{c_h}{2}\big[(\delta_2 - \delta_1) + \sin(\delta_2 - \delta_1)\big] + 2(T - q_0)\sin(\gamma + \delta_1) \tag{3.22}$$

and time arguments suppressed. We let F^* and γ^* denote the steady-state values of F and γ respectively, allowing for the following expressions for the steady-state values of c_{-1}^R and c_{-1}^I:

$$\begin{aligned} c_{-1}^{R*} &= \tfrac{\beta}{\sqrt{2\pi}} F_1^* \cos\gamma^* \\ c_{-1}^{I\,*} &= -\tfrac{\beta}{\sqrt{2\pi}} F_1^* \sin\gamma^*. \end{aligned} \tag{3.23}$$

Thus, we have

$$\begin{aligned} \tan(\phi_1^*) &= \frac{c_{-1}^{I\,*}}{c_{-1}^{R*}} \\ &= -\tan(\gamma^*). \end{aligned} \tag{3.24}$$

Similar calculations for the steady-state values of the higher-order coefficients yield the general equations

$$\begin{aligned}\tau_0 \frac{dc_{-\mu}^R(t)}{dt} &= -c_{-\mu}^R(t) + \tfrac{\beta}{\sqrt{2\pi}} F_\mu(t) \cos\big(\gamma(t)\big) \\ \tau_0 \frac{dc_{-\mu}^I(t)}{dt} &= -c_{-\mu}^I(t) - \tfrac{\beta}{\sqrt{2\pi}} F_\mu(t) \sin\big(\gamma(t)\big). \end{aligned} \tag{3.25}$$

As before, we note that the evolution of $c_\mu(t)$, and therefore of $F_\mu(t)$, $\forall\ \mu \in \mathbb{Z}$ depends only

on the first-order coefficients $c_{|\mu|\leq 1}(t)$. Therefore, the steady-state values of the higher-order coefficients

$$\begin{aligned} c_{\text{-}\mu}^{R\,*} &= \tfrac{\beta}{\sqrt{2\pi}} F_\mu^* \cos(\mu\gamma^*) \\ c_{\text{-}\mu}^{I\,*} &= -\tfrac{\beta}{\sqrt{2\pi}} F_\mu^* \sin(\mu\gamma^*) \end{aligned} \tag{3.26}$$

and the corresponding ϕ_μ, i.e,

$$\begin{aligned} \tan(\phi_\mu^*) &= \frac{c_{\text{-}\mu}^{I\,*}}{c_{\text{-}\mu}^{R\,*}} \\ &= -\tan(\mu\gamma^*), \end{aligned} \tag{3.27}$$

are fully determined by the solution to 3.19.

Substitution of 3.26 into 3.5 then gives:

$$\begin{aligned} a_\infty(\theta) &= \frac{1}{\sqrt{2\pi}} c_0^* + \frac{\beta}{\pi} \sum_{\mu\geq 1} \big(F_\mu^* \cos(\mu\gamma^*) \cos\mu\theta - F_\mu^* \sin(\mu\gamma^*) \sin\mu\theta \big) \\ &= \frac{1}{\sqrt{2\pi}} c_0^* + \frac{\beta}{\pi} \sum_{\mu\geq 1} F_\mu^* \cos\big(\mu(\theta+\gamma^*)\big), \end{aligned} \tag{3.28}$$

so that $\theta = -\gamma^*$ represents the peak angle of the steady-state profile $a_\infty(\theta)$.

Further, from 3.13, we have

$$\begin{aligned} \tan(\gamma^*) &= -\frac{q_{\mathrm{I}}^*}{q_{\mathrm{R}}^*} \\ &= -\frac{c\sin\bar{\theta} - \frac{\beta}{\pi}\lambda_{\text{-}1} F^* \sin\gamma^*}{c\cos\bar{\theta} + \frac{\beta}{\pi}\lambda_{\text{-}1} F^* \cos\gamma^*} \end{aligned} \tag{3.29}$$

which requires

$$\gamma^* = -\bar{\theta}. \tag{3.30}$$

That is, the steady-state peak $-\gamma^*$, implicit in 3.19, is equivalent to the LGN hue input $\bar{\theta}$.

3.2.2 Obtaining the Steady-State Profile

Note, next, that the steady-state solution requires $\frac{da_\infty(\theta)}{dt} = 0$ so that 2.1 becomes

$$a_\infty(\theta) = g[h_\infty(\theta)]. \tag{3.31}$$

Thus, the shape of the activity profile at the steady state is equivalent to the net cortical input, cut off by g at $\delta_1^* \equiv \theta_{c1}^*$ and $\delta_2^* \equiv \theta_{c2}^*$. Here, $\theta_{c1,c2}^*$ are the critical cutoff angles for the steady-state activity profile, beyond which $a_\infty(\theta)$ would take on negative values. That is, at the steady state, the cutoff angles in the Heaviside formulation of g are equivalent to the critical angles of the activity profile. Further, since $h_\infty(\theta)$ is a function of the first-order coefficients $c_{|\nu|\leq 1}^*$, we need only solve 3.19 to determine the steady-state profile. We do so numerically using the forward Euler method, assuming a random initial activity with values for all hue preferences between 0 and 2 spikes/sec and propagating $c_{|\nu|\leq 1}(t)$ forward in time to large t (see Appendix B). Substitution of these coefficients into 3.12 yields the steady-state values of $h(\theta, t)$ in terms of q_0^*, c_h^*, and γ^*.

Thus, at the steady state, 3.31 reads

$$a_\infty(\theta) = \beta \left[q_0^* + c_h^* \cos(\theta - \bar{\theta})\right]_+ \tag{3.32}$$

where $[x]_+$ is the rectification function which cuts off the steady-state tuning curve at values below zero. Figure 3.2 shows an example of a hue tuning curve obtained with this method.

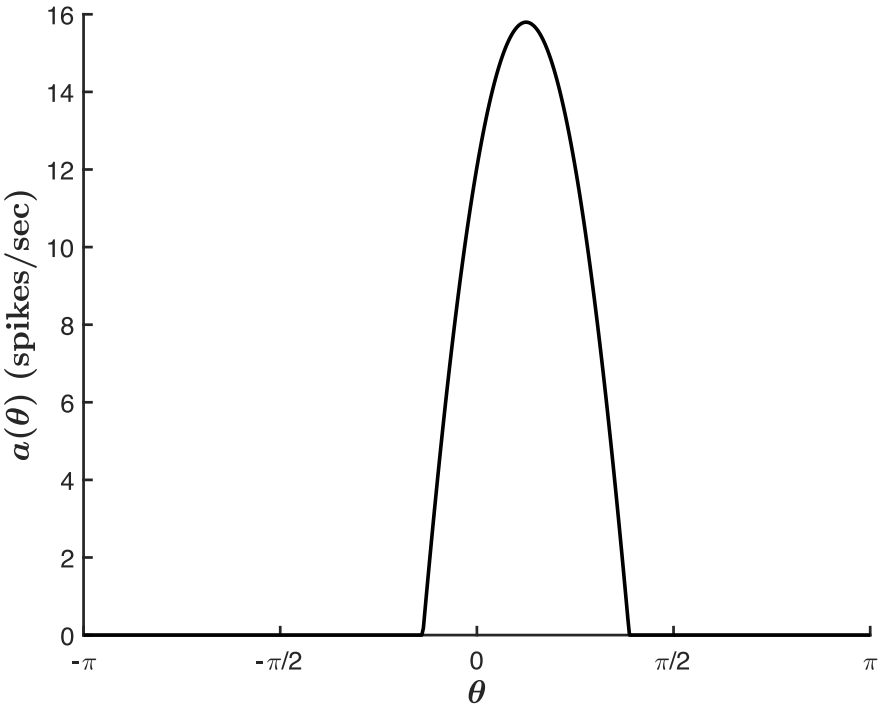

Figure 3.2: Steady-state activity profile obtained using the method described in 3.2.2. Parameters are as in Fig. 3.1.

It is important to bear in mind that the solution above only applies to the steady state. A general time-dependent solution is analytically intractable because the coupling of the coefficients imposed by the nonlinearity requires an infinite number of similar computations to obtain $c_{|\mu|>1}$ in our eigenfunction expansion of $a(\theta, t)$ (3.5). However, $h(\theta, t)$ is always fully determined by the first-order Fourier components of $a(\theta, t)$, regardless of the discontinuity introduced by the cutoff. It is only at the steady state, therefore, when the profile is equivalent to the rectified input, that the activity may be expressed in terms of the first-order Fourier coefficients as in 3.32.

Despite this, the model does permit a time-dependent analytical solution for cases where the activity of all the hue preferring cells is above threshold.

3.3 Solution for the Linear Case

We assume in the linear case that the net input $h(\theta, t)$ is above threshold throughout the dynamics such that the activity profile is never cut off and $\mathcal{H}\big(h(\theta,t)-T\big) = 1 \; \forall \; \theta \in \{-\pi, \pi\}$. Equation 3.8 therefore takes the linear form:

$$\tau_0 \sum_{-\infty}^{\infty} \frac{dc_\mu(t)}{dt} \hat{e}_\mu(\theta) = -\sum_{-\infty}^{\infty} c_\mu(t) \hat{e}_\mu(\theta) + \beta \cdot \big(h(\theta,t) - T\big) \tag{3.33}$$

Taking the inner product of 3.33 with $\hat{e}_\nu$ as before, we obtain the system of equations for all the coefficients c_μ:

$$\begin{aligned}
\tau_0 \frac{dc_0(t)}{dt} &= (2\pi\beta J_0 - 1)c_0(t) - \sqrt{2\pi}\beta T \\
\tau_0 \frac{dc_1(t)}{dt} &= (\beta\pi J1 - 1)c_1(t) + \sqrt{\tfrac{\pi}{2}}\beta c(l - is) \\
\tau_0 \frac{dc_{\text{-}1}(t)}{dt} &= (\beta\pi J1 - 1)c_{\text{-}1}(t) + \sqrt{\tfrac{\pi}{2}}\beta c(l + is) \\
\tau_0 \frac{dc_\nu(t)}{dt} &= -c_\nu(t) \; \forall \; |\nu| > 1
\end{aligned} \tag{3.34}$$

We may thus solve for each of the coefficients independently, yielding equations for the evolution of each:

$$\begin{aligned}
c_0(t) &= K_0 e^{-(1-2\pi\beta J_0)t/\tau_0} - \tfrac{\sqrt{2\pi}\beta T}{1-2\pi\beta J_0} \\
c_{\text{-}1}(t) &= K_{\text{-}1} e^{-(1-\pi\beta J_1)t/\tau_0} + \tfrac{\sqrt{\frac{\pi}{2}} c\beta(l+is)}{1-\pi\beta J_1} \\
c_1(t) &= K_1 e^{-(1-\pi\beta J_1)t/\tau_0} + \tfrac{\sqrt{\frac{\pi}{2}} c\beta(l-is)}{1-\pi\beta J_1} \\
c_\nu(t) &= K_\nu e^{-t} \; \forall \; |\nu| > 1
\end{aligned} \tag{3.35}$$

with the constants K_ν determined by the Fourier coefficients $c_\nu(0)$ of the initial activity

$a(\theta, 0)$ as:

$$
\begin{aligned}
K_0 &= c_0(0) - \tfrac{\sqrt{2\pi}\beta T}{1-2\pi\beta J_0} \\
K_{\pm 1} &= c_{\pm 1}(0) - \tfrac{\sqrt{\frac{\pi}{2}} c\beta(l \mp is)}{1-\pi\beta J_1} \\
K_\nu &= c_\nu(0) \;\forall\; |\nu| > 1.
\end{aligned} \tag{3.36}
$$

Substitution of 3.35 into the activity expansion 3.5 then gives the closed-form solution for the evolution of the activity:

$$
\begin{aligned}
a(\theta, t) = &\big\{ K_0 e^{-(1-2\pi\beta J_0)t/\tau_0} - \tfrac{\sqrt{2\pi}\beta T}{1-2\pi\beta J_0} \big\} \frac{1}{\sqrt{2\pi}} \\
&+ \big\{ K_{\text{-}1} e^{-(1-\pi\beta J_1)t/\tau_0} + \tfrac{\sqrt{\frac{\pi}{2}} c\beta(l+is)}{1-\pi\beta J_1} \big\} \frac{1}{\sqrt{2\pi}} e^{-i\theta} \\
&+ \big\{ K_1 e^{-(1-\pi\beta J_1)t/\tau_0} + \tfrac{\sqrt{\frac{\pi}{2}} c\beta(l-is)}{1-\pi\beta J_1} \big\} \frac{1}{\sqrt{2\pi}} e^{i\theta} \\
&+ \big\{ K_\nu \frac{1}{\sqrt{2\pi}} e^{-t} \big\} e^{i\nu\theta} \Big|_{|\nu|>1}
\end{aligned} \tag{3.37}
$$

which is stable for $1 - 2\pi\beta J_0 > 0$ and $1 - \pi\beta J_1 > 0$. We call the corresponding (J_0, J_1) parameter space the **analytical regime**.

At the steady state, i.e., as $t \to \infty$, 3.37 gives

$$
\begin{aligned}
a_\infty(\theta) &= -\frac{\beta T}{1-2\pi\beta J_0} + \frac{c\beta(l+is)}{2(1-\pi\beta J_1)} e^{-i\theta} + \frac{c\beta(l-is)}{2(1-\pi\beta J_1)} e^{i\theta} \\
&= -\frac{\beta T}{1-2\pi\beta J_0} + \frac{c\beta\cos(\theta - \bar{\theta})}{1-\pi\beta J_1}.
\end{aligned} \tag{3.38}
$$

We see from 3.38 that as $t \to \infty$, $c_{|\mu|>1} \to 0$. Further, unlike the nonlinear case, the steady-state coefficients $c_{|\mu|<1}$, and thus the hue tuning curve, can be expressed analytically in terms of the cortical parameters. Note also that the solution 3.37 constrains T to val-

ues such that the input is not rectified throughout the dynamics. However, 3.38 holds for $h_\infty(\theta) > T$, regardless of whether thresholding has been implemented at any point. This can be seen in the Fourier analysis of the steady-state profile (see Appendix A), which makes no assumptions about the preceding dynamics. Thus, 3.38 restricts T such that

$$T \leq -\frac{c(1-2\pi\beta J_0)}{1-\pi\beta J_1} \equiv T_c. \tag{3.39}$$

The tuning curve satisfying these conditions is analogous to Hansel and Sompolinksy's broad profile of orientation tuning [45]. Figure 3.3 shows one such curve at the limit $T = T_c$. The figure demonstrates the difference between a stand-alone analysis of the steady state and one that considers the dynamics leading to its emergence. While thresholding in this example is not applied at the steady state, $h(\theta, t)$ is usually rectified early on in the dynamics, with $\delta_1(t)$ and $\delta_2(t)$ dependent on the initial conditions of the activity. In those cases, 3.33 does not hold and the solution must satisfy the original nonlinear equation. Thus, though we may use 3.38 to obtain figure 3.3, the activity does not typically obey 3.37 throughout the preceding interval. Only for a narrow range of initial conditions can we use the linear and nonlinear models interchangeably.

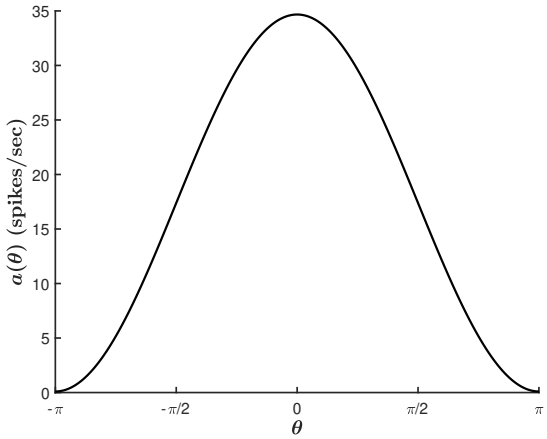

Figure 3.3: Steady-state solution for $T = T_c$ and $\bar{\theta} = 0$ with $J_0 = -2$, $J_1 = .3$, and $\beta = c = 1$.

Even so, we note that with 3.39, the activity dynamics appear to be "linear" in the sense that the activity itself is never cut off. In the case of figure 3.3, for example, the activity profile stops evolving right before it would take on negative values. However, it is the rectification on $\{h(\theta,t) - T\}$ — not $a(\theta,t)$ — which ensures that the activity is always positive, and therefore physiological, a distinction easily overlooked in light of the equivalence $a_\infty = \beta(h-T)$ in the linear steady-state solution. That is, we cannot assume a linear solution based on the dynamics of $a(\theta,t)$ alone. To trace the general nonlinear solution leading up to the steady state, as well as the steady state for $T > T_c$, we must turn to numerical methods.

3.4 Numerical Solution

We approach the solution to 2.1 with a Forward Euler method (see Appendix B), propagating the activity from a random array of spontaneous initial values between 0 and .2 spikes/sec to its steady-state profile. Within each timestep (typically chosen to be .1 msec), we coarse-grain the network into $n = 501$ populations with hue preferences separated evenly across the DKL angle domain $[-\pi, \pi]$. The choice of an odd n allows us to numerically integrate 2.10 using the Composite Simpson's Rule, whereupon we rectify $\{h(\theta,t) - T\}$ and evaluate the right-hand side of 2.1. Note that the Fourier coefficients of the emergent steady-state tuning curve are equivalent to those obtained in the manner of section 3.2.2. Below, I use the term *tuning curve* only in reference to these steady-state profiles.

We emphasize that the values of the cortical parameters J_0, J_1, c, T, and β are bound by the physiological properties of V1. Varying these parameters in the subsequent analysis is therefore an investigation of their relative effects on hue processing, and we are not fine-tuning their weights to obtain specific hue tuning curves. As described in section 1.3, this approach differs from those of the previous combinatorial models of color processing, in which the authors tune the weights of signals from successive processing stages to generate specific hue selectivity.

Here, we explore a range of values for the cortical parameters under the constraint that the network activity remains between 0 and 60 spikes/sec, as motivated in chapter two. Our main aim is to characterize their relative effects on the width, $\Delta_c = \theta^*_{c2} - \theta^*_{c1}$, and peak height, $a_\infty(\bar{\theta})$, of the network tuning curves. Together, these two properties reflect the network selectivity and emergent signal strength, respectively.

It is also important to distinguish between a network tuning curve and a single-neuron tuning curve. The former is a coarse-grained representation of the CO blob response, with the horizontal axis representing the gamut of hue preferences within a single network. A relatively large tuning width would therefore indicate considerable responses from a wide range of hue tuning cells and poor network selectivity. The single-neuron tuning curve, on the other hand, is an electrophysiological recording of an individual cell's response to a set of hue stimuli, with the horizontal axis representing the range of stimulus hue angles used in the experiment. The peak location of the single-neuron tuning curve would therefore indicate the hue preference of the individual neuron, while the width would represent its selectivity for that specific hue. Thus, though the two types of tuning curves are labeled and shaped similarly, the latter is only useful to characterize our network's constituent neurons and *not* the emergent properties of the population as a whole [8].

3.4.1 Roles of Stimulus Strength and Cortical Threshold

We begin our analysis by considering the role of the stimulus signal strength c on the hue tuning width and peak height. Figure 3.4 shows typical tuning curves for two values of J_1. We see that for lower values of J_1 (panel a), c has a pronounced, but quickly saturating, effect on Δ_c. With increasing values of J_1 (panel b), Δ_c saturates for lower values of the stimulus strength. Above saturation, the main contribution of the chromatic signal is to increase the network response, i.e., to increase $a_\infty(\bar{\theta})$.

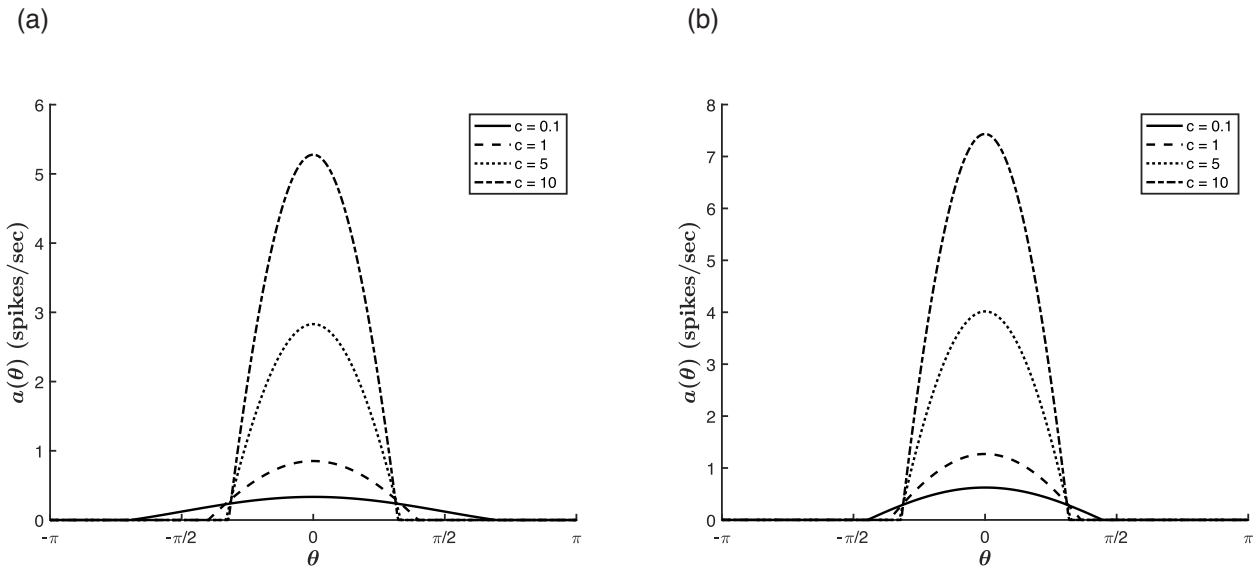

Figure 3.4: Effect of c on the tuning curve properties. For $\bar{\theta} = 0$, $\beta = 1$, $T = -1$, and $J_0 = -1$. (a) $J_1 = .2$ (b) $J_1 = .7$.

We also note that at $T = 0$, the trend reverses, such that increasing c has no effect on the tuning width at $T = 0$ and a widening effect for $T > 0$. Figure 3.5 below illustrates this reversal with four tuning curves of matched parameters and varying values of T. The coupling of c and T must be considered because some neural field models (see [1, 13, 21]) take $T = 0$ for mathematical simplicity. Indeed, we might expect that there is no more physiological significance to choosing a threshold potential of $T = 0$ mV than any other value, beyond their relative magnitudes to $h(\theta, t)$. However, the independence of c and Δ_c at $T = 0$ and the significance of the relative signs of c and T elsewhere suggest quite the opposite. The chromatic input strength ceases to have an effect on the network hue selectivity not only once the anisotropic strength parameter, J_1, is large enough to predominate, but also as $T \to 0$. As shown in figure 3.6, the effect of the sign reversal points to the fact that the stimulus strength, which is always positive, stretches $h(\theta, t)$. For $T > 0$ (panel d), this raises $h(\theta, t)$ above threshold for a larger subset of the hue angles, meaning more neurons receive sufficient input to contribute to the network dynamics and, therefore, an increase in Δ_c with

increasing c. However, for $T < 0$ (panels a, c), an increase in the stimulus strength narrows the range of neurons receiving an input above threshold.

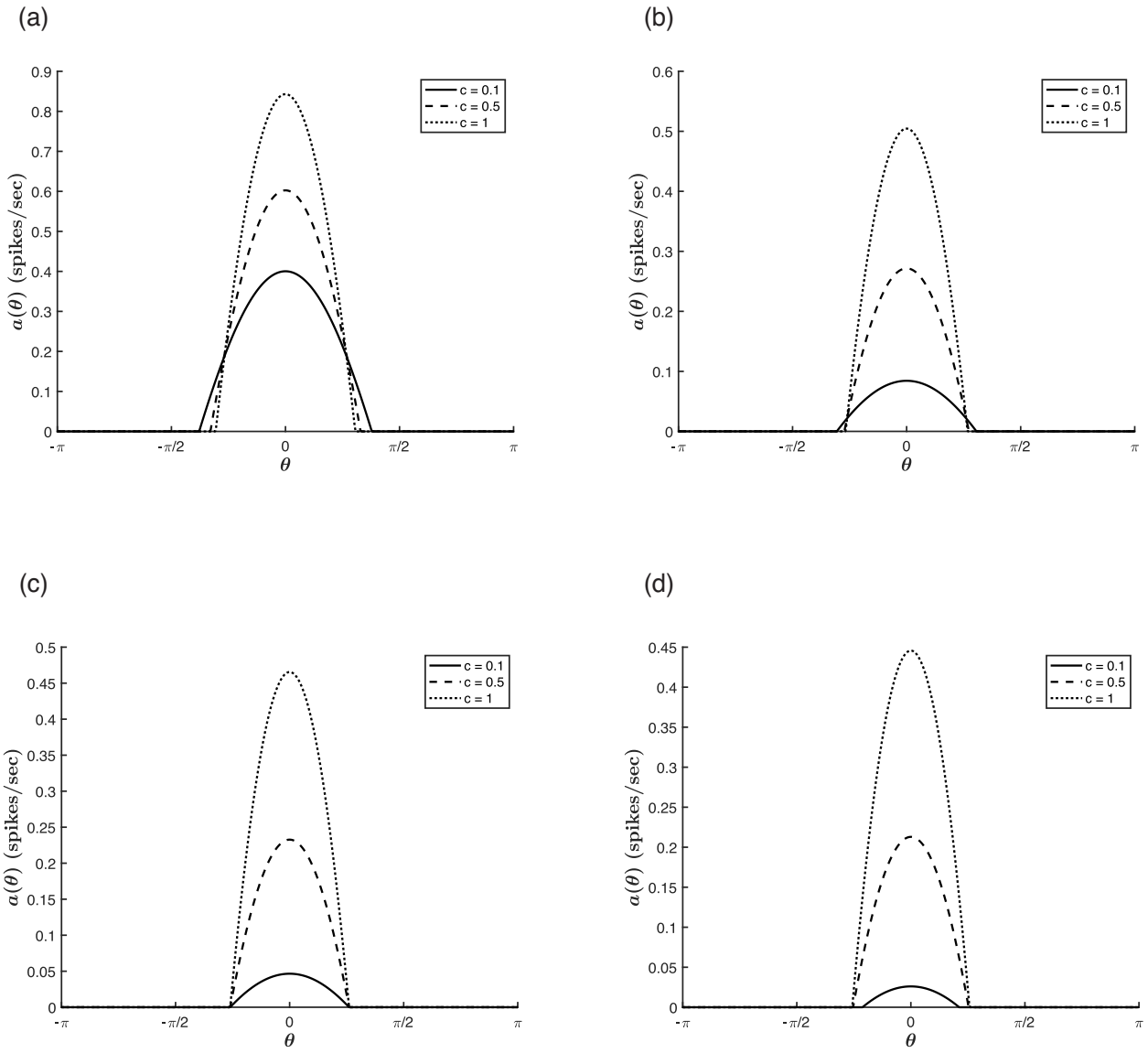

Figure 3.5: Effect of c on the tuning curve for varying values of T with $\beta = 1$, $J_0 = -2$, $J_1 = 1$, and $\bar{\theta} = 0$. Note that the small network response rates are due to the low values of c chosen here. (a) $T = -1$. (b) $T = -.1$. (c) $T = 0$. (d) $T = .05$.

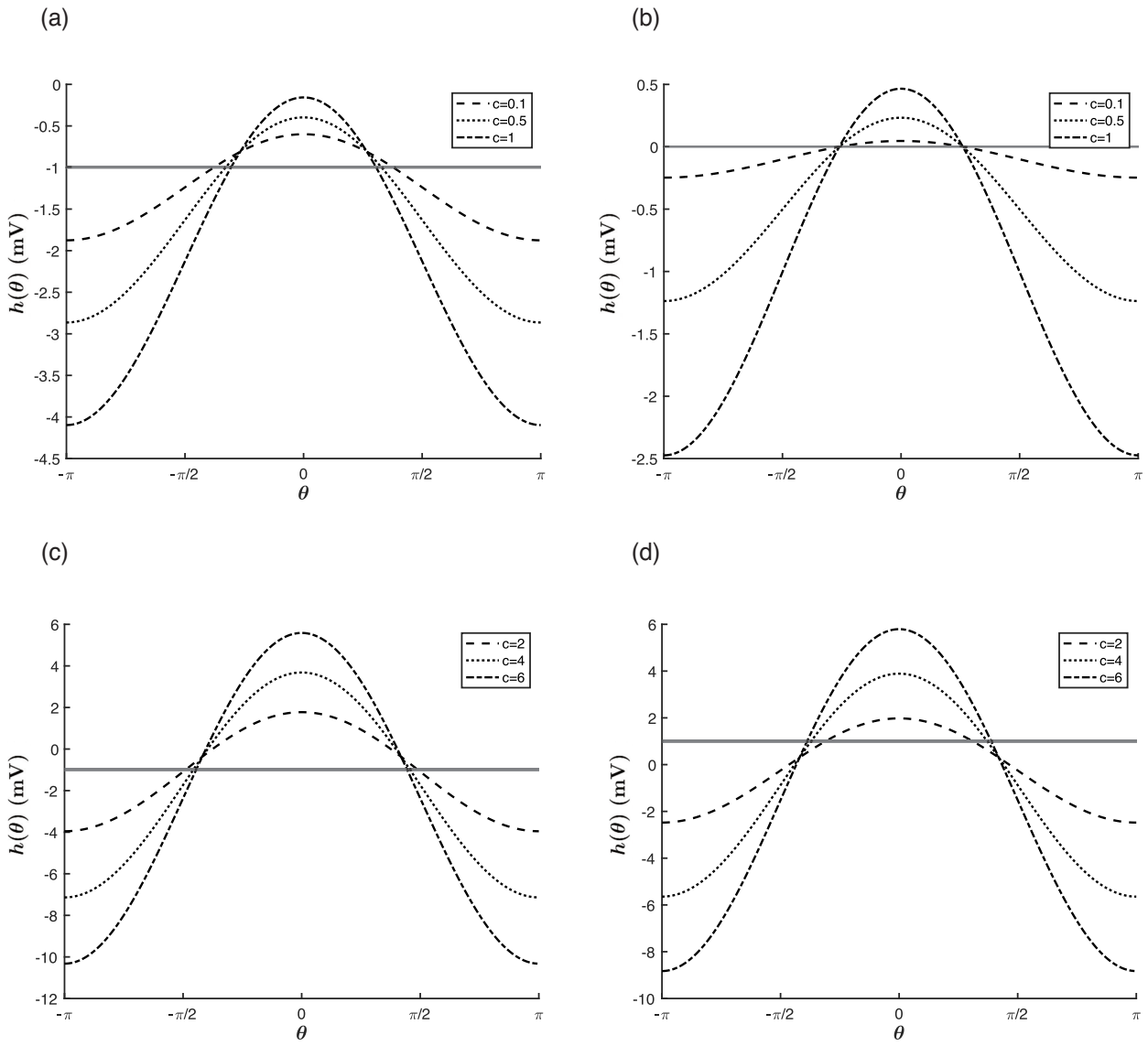

Figure 3.6: (a)-(b): Effect of c on $h_\infty(\theta)$ for (a) $T = -1$ and (b) $T = 0$ with parameters as in Fig. 3.5. (c)-(d): With $J_0 = -.2$ and $J_1 = .2$ for (c) $T = -1$. (d) $T = 1$.

The coupling of c and T is equally significant to the effects of T on the tuning curve properties. Figure 3.7 shows that below a certain value, T primarily modulates $a_\infty(\bar{\theta})$. However, for comparable magnitudes of the stimulus strength and threshold, $|c| \sim |T|$, we see a transition in which T also begins to sharpen the tuning curve and continues to do so until the threshold surpasses $h(\theta, t)$ for all θ (i.e., for $\delta_1^* = \delta_2^* = 0$). Accordingly, for

higher stimulus strengths, the thresholding nonlinearity plays a greater role in modulating the network selectivity at lower and a wider range of T values.

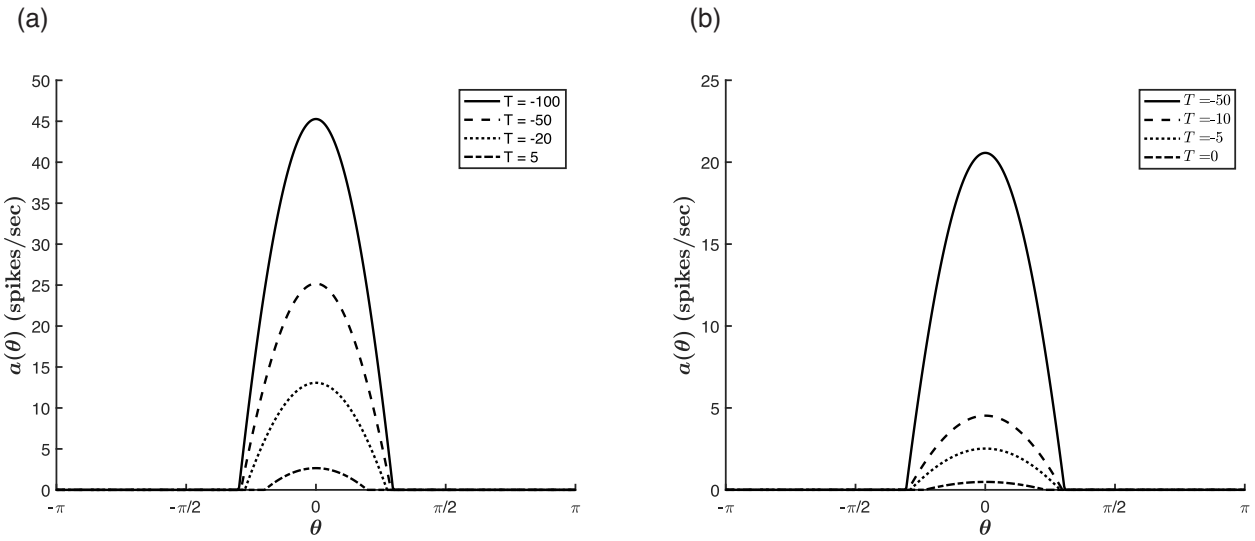

Figure 3.7: Effect of T on the tuning curve properties. $\beta = 1$, $J_0 = -3$, $J_1 = 2$, and $\bar{\theta} = 0$. (a) $c = 10$. (b) $c = 1$.

Finally, we note that β acts similarly to c for $T < 0$, narrowing Δ_c to a saturating value and raising $a_\infty(\bar{\theta})$ without bound. However, as illustrated in Fig. 3.8, it does so for both negative and positive values of T. In fact, as a factor multiplying $g(h)$ post-rectification, its narrowing role holds for varying values of c (Fig. 3.9), as well as the cortical parameters J_0 and J_1 (Fig. 3.10). That is, β works cooperatively with these parameters to enhance the network selectivity. As we will see next, whether or not such cooperativity holds for the relationship between the stimulus and cortical parameters has important bearings on their relative processing roles in V1.

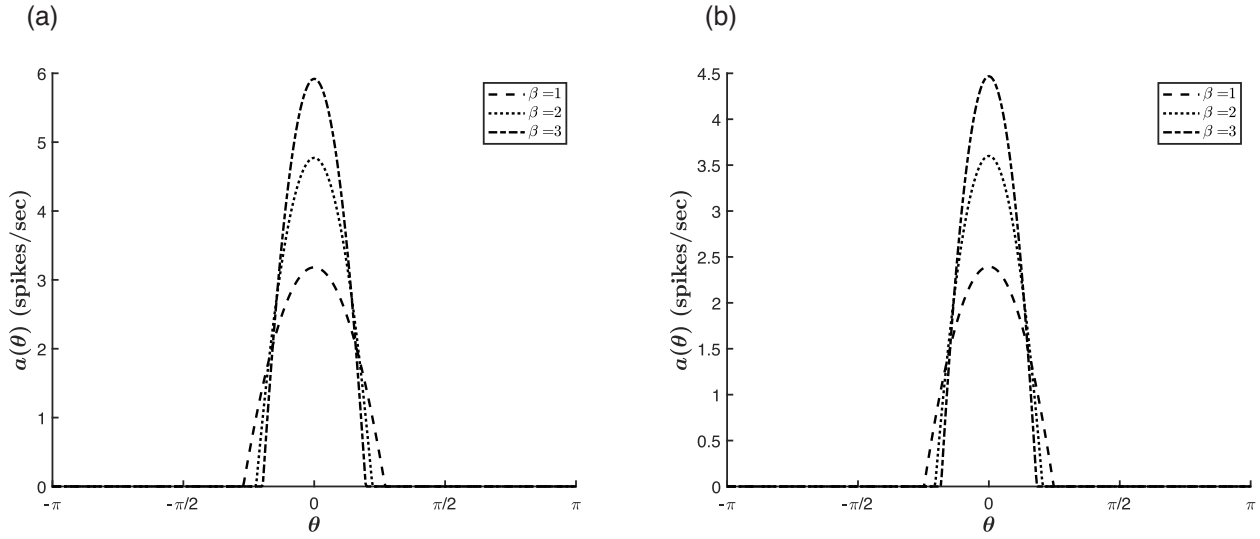

Figure 3.8: Effect of β on the tuning curve properties for varying values of T. $c = 6$, $J_0 = -2$, $J_1 = 1$, and $\bar{\theta} = 0$. (a) $T = -1$. (b) $T = 1$.

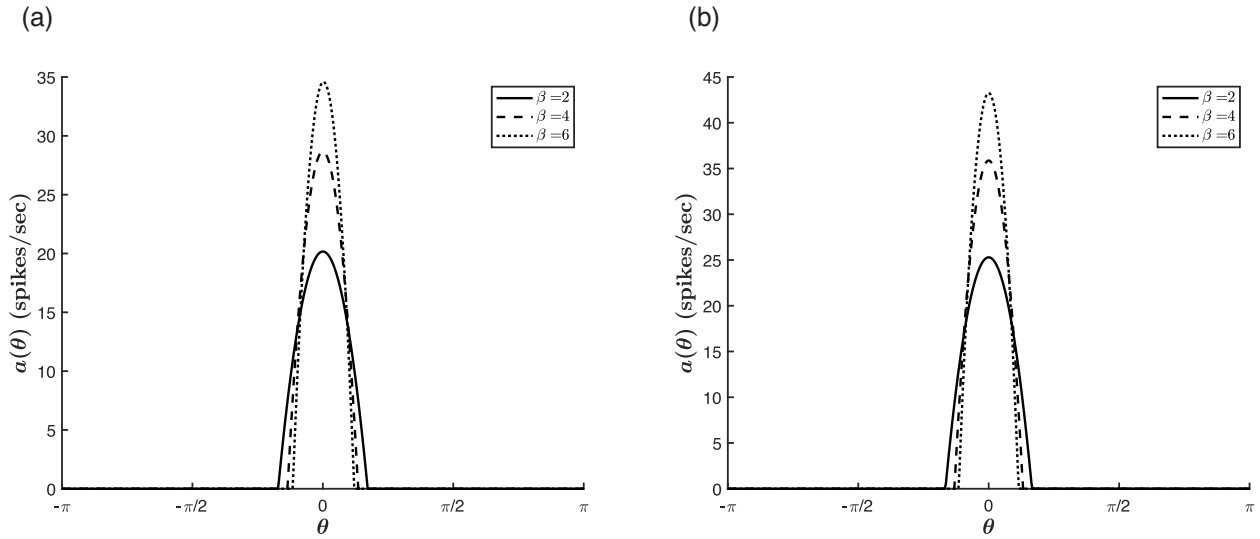

Figure 3.9: Effect of β on the tuning curve properties for varying values of c. $J_0 = -7$, $J_1 = 5$, $T = -40$, and $\bar{\theta} = 0$. (a) $c = 1$. (b) $c = 10$.

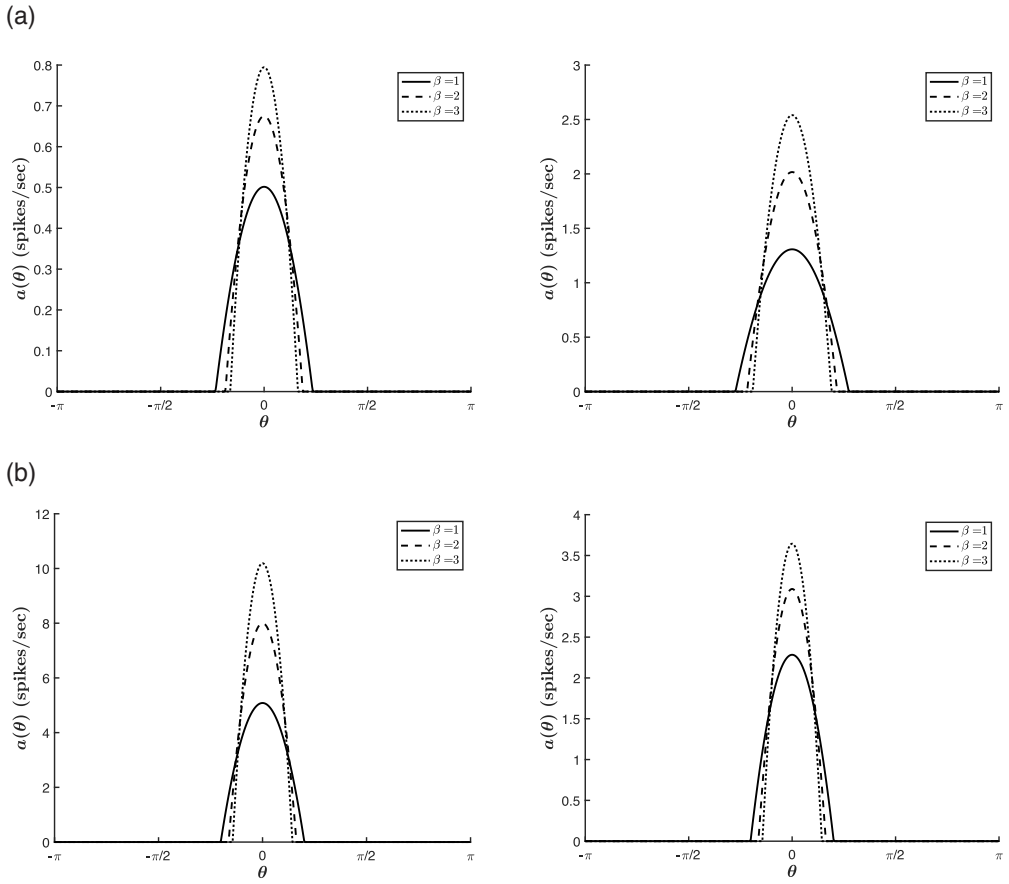

Figure 3.10: Effect of β on the tuning curve properties for varying values of J_0 (panel a) and J_1 (panel b). (a) $c = 1$, $J_1 = 2$, $T = -2$, and $\bar{\theta} = 0$. Left: $J_0 = -7$. Right: $J_0 = -3$. (b) $c = 10$, $J_0 = -5$, $T = 0$, and $\bar{\theta} = 0$. Left: $J_1 = 4$. Right: $J_1 = 1$.

3.4.2 Role of the Cortical Weights

The anisotropic connectivity strength J_1 exhibits similar relationships to the tuning curve properties to those of c. That is, for $T < 0$, Δ_c narrows with increasing J_1 to a saturating value, at which point $a_\infty(\bar{\theta})$ continues to increase (see Fig. 3.11, panel a). The trend with respect to Δ_c reverses for $T > 0$ (panel b), whereas the trend with respect to $a_\infty(\bar{\theta})$ remains unaffected. These similarities are a mark of the competition between the external input and the cortical parameters in driving the network selectivity and reflect the fact that both

parameters modulate the anisotropic terms of the model.

Fig. 3.12 shows two sets of tuning curves for two close values of c. Even with such small variations in c, we see that the role of J_1 in driving network selectivity becomes more significant with decreasing stimulus strength. However, a large external input does not suppress the contribution of J_1 to the overall network activity. That is, increasing J_1 results in raising $a_\infty(\bar{\theta})$, regardless of the strength of the stimulus (see Fig. 3.13, panel a). Similarly, a relatively large value of J_1 does not restrict the growth of the network response with increasing stimulus strength (panel b). Thus, the anisotropic tuning introduced by the external input and the recurrent interactions act cooperatively to raise the network's response to the stimulus hue, and competitively to tune its selectivity.

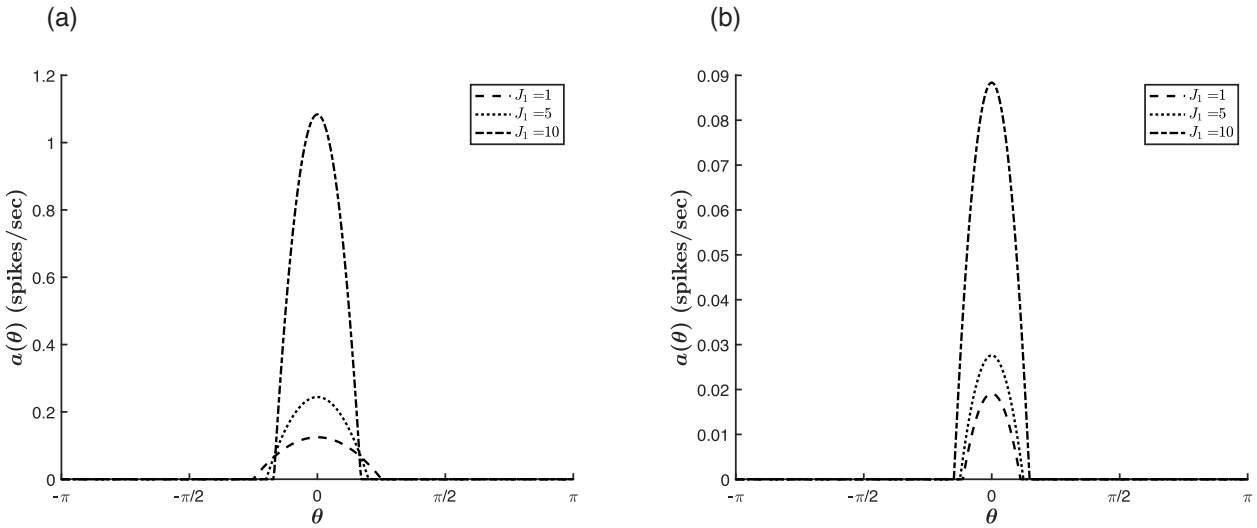

Figure 3.11: Effect of J_1 on the tuning curve properties for varying values of T. $\beta = 1$, $c = .3$, $J_0 = -10$, and $\bar{\theta} = 0$. (a) $T = -1$. (b) $T = .2$.

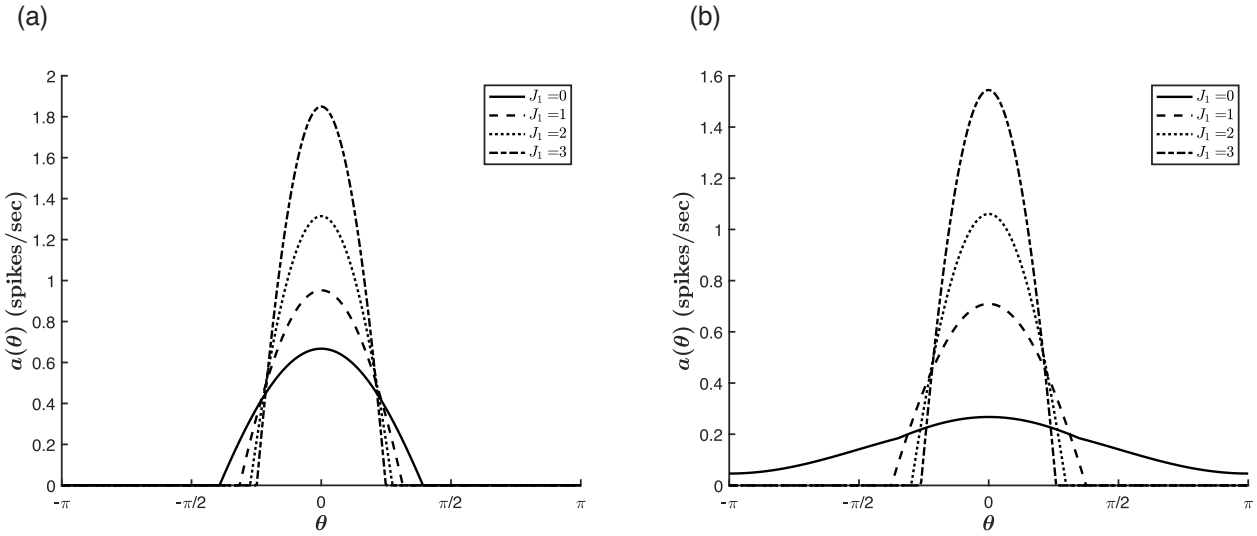

Figure 3.12: Effect of J_1 on the tuning curve properties for different stimulus strengths. $\beta = 1$, $T = -5$, $J_0 = -5$, and $\bar{\theta} = 0$. (a) $c = 1$. (b) $c = .2$.

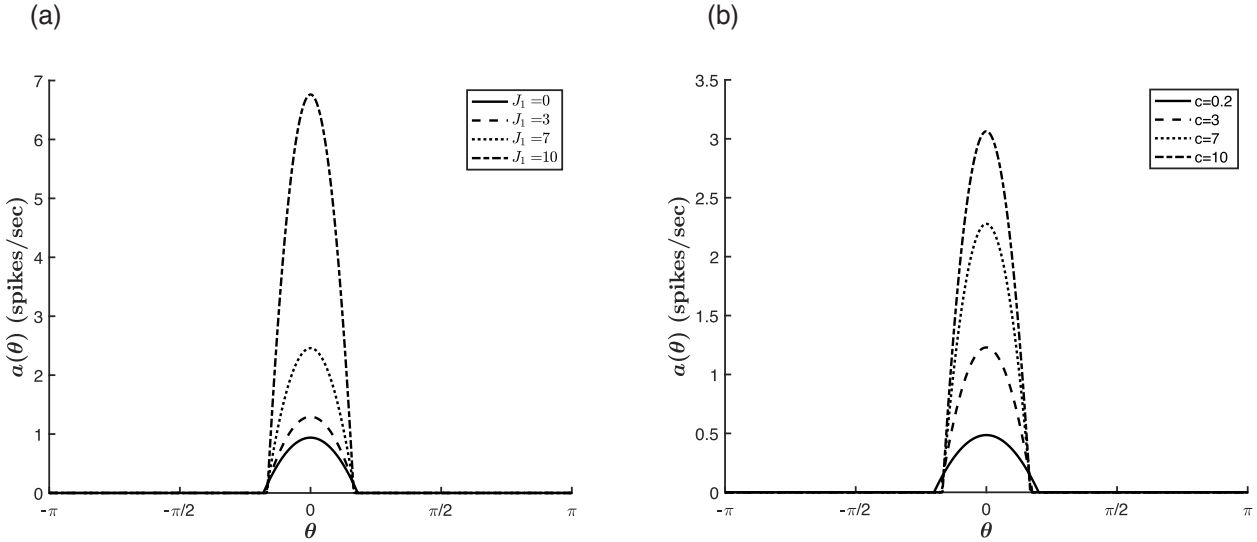

Figure 3.13: Effect of J_1 and c on $a_\infty(\bar{\theta})$. $\beta = 1$, $T = -2$, $J_0 = -10$, and $\bar{\theta} = 0$. (a) $c = 6$. (b) $J_1 = 6$.

In contrast, J_0 acts cooperatively with the external stimulus to sharpen the curves. As shown in figure 3.14, the tuning curves narrow with decreasing values of J_0, i.e., with an increase in the relative strength of global inhibition to global excitation, a trend which is conserved for various stimulus strengths. Furthermore, there is no trend reversal at $T = 0$. Rather, for much of the parameter space, J_0 acts with the thresholding to sharpen the tuning curves, as is illustrated in Fig. 3.15.

This could be expected from the fact that at each point throughout the dynamics, both T and J_0 act isotropically on all hue preferences, lowering or raising the input for all contributing neurons. However, this commonality also means that for $|T| >> |c|$ (where the effect of T on Δ_c saturates, as explained above), the thresholding suppresses the role of J_0, analogous to the competition between c and J_1 (see Fig. 3.16). Finally, figures 3.14 and 3.15 also show that increasing the global inhibition acts to reduce the value of $a_\infty(\bar{\theta})$ for all c and T.

We thus conclude that the emergent hue curves in V1 are *both* inherited from the LGN *and* built on the recurrent interactions. The competition between J_1 and c points to a continuum of regimes in which either h_{lgn} or h_{ctx} dominates. However, in all regimes, J_0 works cooperatively with c to narrow the curves, and all the parameters work together to raise the network response. Likewise, the competition between J_0 and T (both cortical parameters) is modulated by the value of c, and we recall from section 3.2.1 that the location of the peak is always completely determined by the LGN signal, regardless of the relative magnitudes of the cortical and stimulus strength parameters.

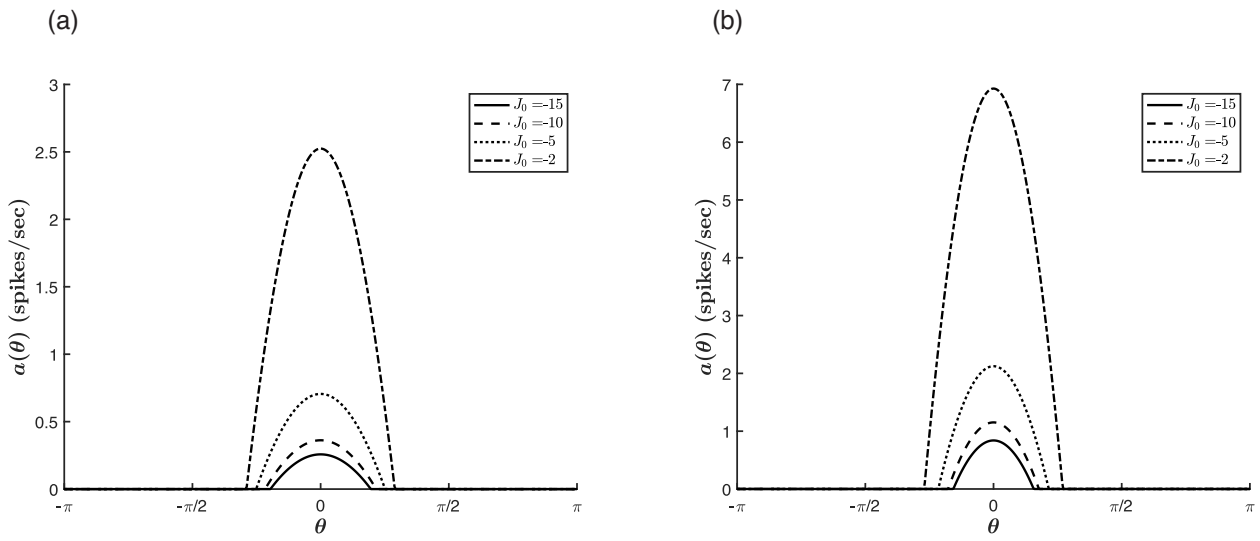

Figure 3.14: Effect of J_0 on the tuning curve properties for varying stimulus strengths. $\beta = 1$, $T = -2$, $J_1 = 2$, and $\bar{\theta} = 0$. (a) $c = 1$. (b) $c = 6$.

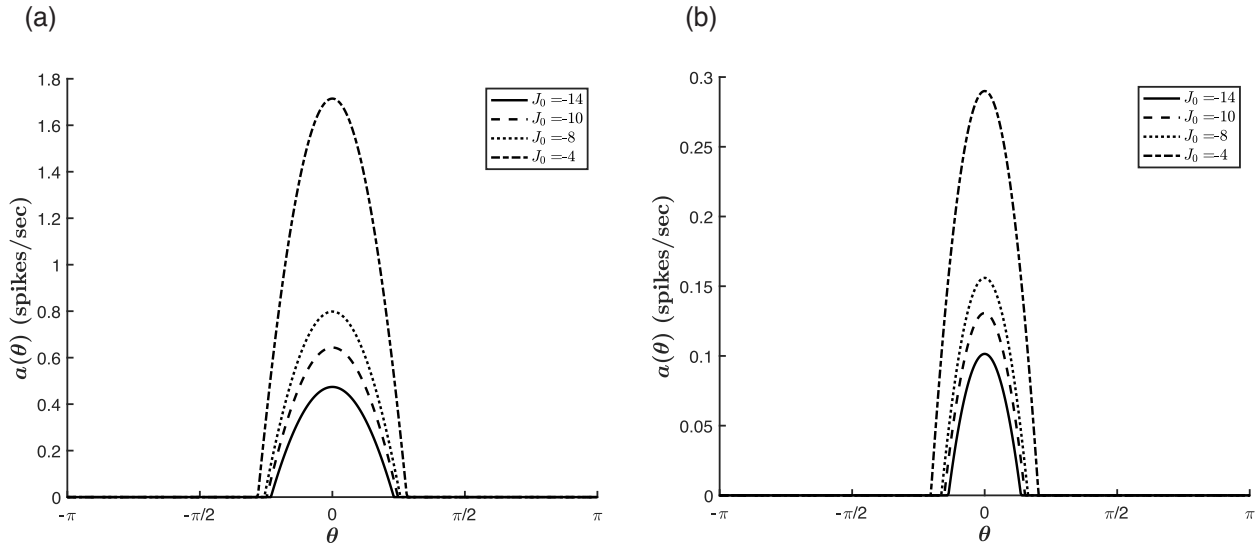

Figure 3.15: Effect of J_0 on the tuning curve properties for varying values of T. $\beta = 1$, $c = 1$, $J_1 = 2$, and $\bar{\theta} = 0$. (a) $T = -5$. (b) $T = .2$.

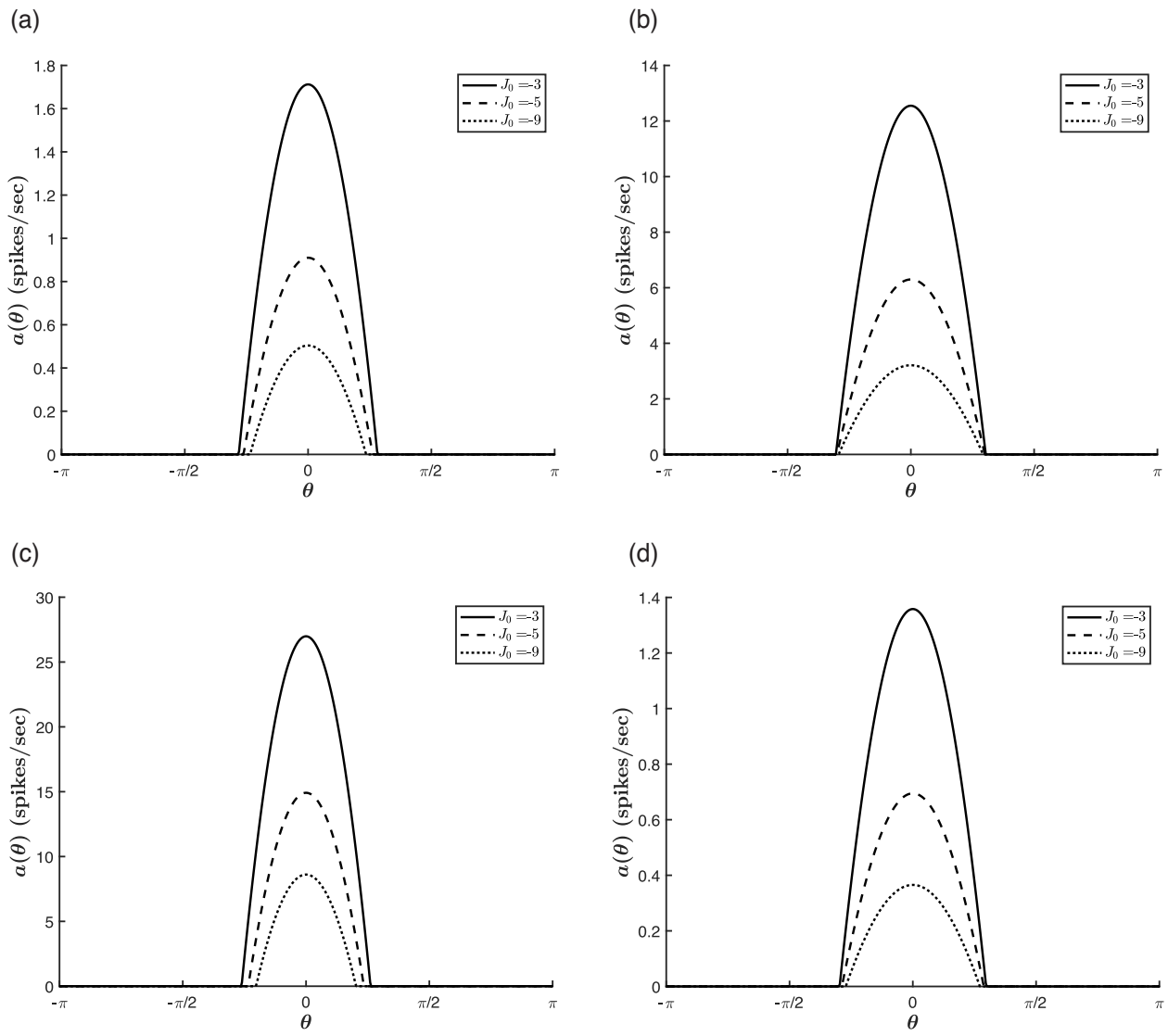

Figure 3.16: Competition between J_0 and T. $\bar{\theta} = 0$, $\beta = 1$, $J_1 = 2$. (a) $c = 1$ and $T = -3$. For $|T| \sim |c|$, J_0 has a strong influence on Δ_c. (b) $c = 1$ and $T = -30$. This effect is suppressed for $|T| >> |c|$. (c) $c = 30$ and $T = -30$. The influence is seen for $|T| >> 0$, as long as the stimulus strength is large enough. (d) $c = .3$ and $T = -3$. Similarly, the influence is suppressed for small $|T|$ if the ratio of $|T|/|c| >> 0$.

3.5 Comparison with the Orientation Tuning Model

Finally, we seek to compare the emergent properties of the hue tuning model with those of the orientation tuning model [3, 45]. This leads us to separate the analysis into two regions: one corresponding to the **analytical regime** of section 3.3 with $J_0 < \frac{1}{2\pi\beta}$ and $J_1 < \frac{1}{\pi\beta}$, and the other to the **extended regime** with $J_1 \geq \frac{1}{\pi\beta}$ and J_0 constrained as described in section 3.6. For comparison purposes, note that these parameter regions are analogous to the orientation model's homogeneous and marginal regimes, respectively, labels which refer to the latter's responses to unoriented stimuli.

An important difference between our two models is our choice to assume modularity for the color vision pathway. As described in chapter two, there is no consensus as to when and how the various visual features are separated along the visual pathway. That is, we do not yet understand how the brain recognizes the extent to which an activated color- and orientation-preferring neuron is signalling for a stimulus's color or orientation. And moreover, we do not know at which point of the visual pathway the differentiation becomes important.

We have therefore chosen to emphasize the unoriented color selective cells localized in the CO blob regions of V1, though the model is intended to describe the color processing pathway broadly, for any color-preferring neurons regardless of other feature tuning capabilities. Thus, the choice of modularity is not to reject the possibility of joint feature processing, but rather to parse out the color mechanism for a separate analysis. Furthermore, it is in keeping with perceptual studies which indicate that the red-green and blue-yellow color-opponent systems are only responsive to color stimuli and not to broadband, white light [89]. The difference between our two models thus comes to our choice to consider the purely chromatic component of the input afferent from the LGN, whereas the orientation model incorporates

external inputs with varying degrees of anisotropy, i.e.,

$$h^{\text{ext}}(\theta) = c[1 - \epsilon + \epsilon\cos(2\theta)] \ , \ 0 \leq \epsilon \leq 1/2 \tag{3.40}$$

where ϵ represents the degree of anisotropy.

The differing assumptions underlying the formulation of $h(\theta, t)$ have important implications for the subsequent parameter analyses adopted by our two models. In the orientation tuning model, the authors detail the pronounced shift in the relative roles of the cortical and stimulus parameters in narrowing the tuning curve. In this setup, for $\epsilon \to .5$, an increase in c widens the tuning curve, whereas for $\epsilon \to 0$, the tuning curve selectivity is completely determined by the cortical parameters. The latter scenario constrains the value of the analogous anisotropic cortical parameter, J_2, to the *marginal* regime.

In contrast, as described in section 3.4, our model does not apportion separate regions of the parameter space to external and recurrent mechanisms. Rather, in both the analytical and extended regimes, the roles of c and J_1 exist on a spectrum, where the effect of each parameter is suppressed by larger values of the other. Of course, this suppression is more stark in the extended regime because it covers larger values of J_1. In this sense, the color model draws a similar conclusion to that of the orientation model: when the anisotropic tuning provided by the recurrent interactions is large, the tuning from the stimulus is negligible, and vice versa. However, we emphasize that the transition is not sharp and that c does have an effect on the tuning curve selectivity in the extended regime (see Fig. 3.4), as does J_1 in the analytical regime (see Fig. 3.17 below).

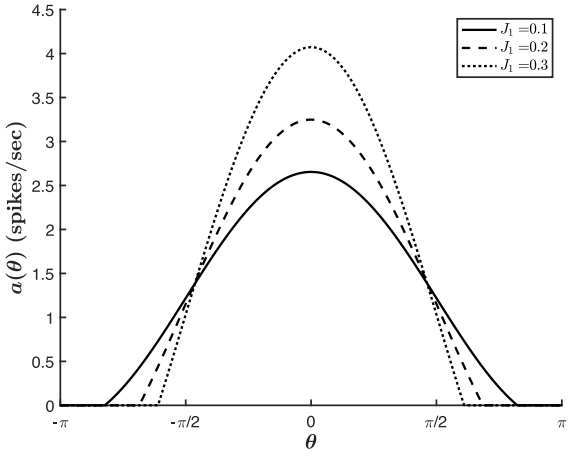

Figure 3.17: Effect of J_1 on the tuning curve selectivity in the analytical regime. For $\bar{\theta} = 0$, $\beta = 1$, $c = 1$, $T = -2$, and $J_0 = -0.1$.

In this regard, the two models are more consistent in their interpretations of J_0's contribution to the selectivity of the tuning curves. That is, in the two regimes of each model, the inhibition acts cooperatively with the thresholding to sharpen the tuning curves. Here again, the orientation model makes a distinction between the marginal phase (i.e., $\epsilon = 0$ and $J_2 \in$ marginal regime), wherein the tuning curve width is completely determined by the cortical anisotropy, and all other cases, where the isotropic inhibition and stimulus come into play. For these cases, the authors argue, J_0 does not act alone to narrow the curve: though J_0 may sharpen the tuning curves, it is the anisotropy from the input or cortical interactions which acts as the source of the orientation selectivity.

Although the color model's tuning mechanism, too, requires a source of *anisotropy*, we have emphasized in section 3.4 that there is no single source of *hue selectivity*. When J_1 is small, in either regime, both the stimulus and the uniform inhibition are significant to the hue tuning mechanism. Figure 3.18 illustrates this with extremes: an example in which the tuning curve narrows with increasing values of c while $J_0 = 0$, and one in which varying c

does not affect Δ_c, though varying J_0 does. Likewise, figure 3.19 shows that for larger values of J_1, decreasing J_0 increases the hue selectivity even when varying J_1 has no effect. We also note that both figures pertain to our analysis of the trend reversal at $T = 0$ in the influence of the anisotropic cortical and stimulus strengths on the network selectivity, in which regard the color and orientation models differ significantly. Specifically, the orientation model does not contain a parameter regime in which increasing values of the anisotropic tuning parameter widen the tuning curve. Moreover, the authors do not consider the narrowing role of the stimulus strength.

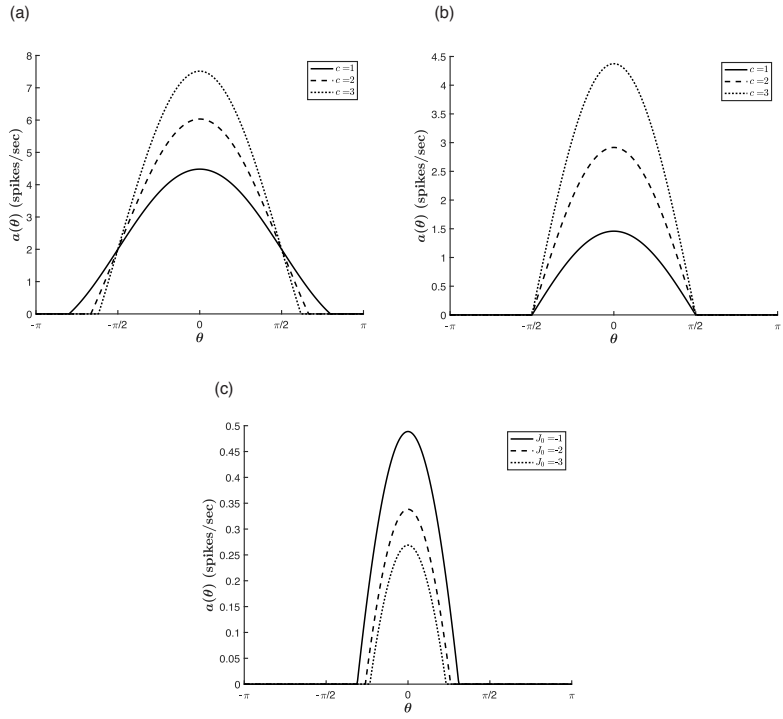

Figure 3.18: The sources of hue selectivity: the roles of J_0 and c. $\bar{\theta} = 0$, $\beta = 1$, and $J_1 = .2$. (a) $J_0 = 0$ and $T = -2$. c has a pronounced effect on Δ_c when $J_0 = 0$, indicating that J_0 is not the only source of hue selectivity. (b) $J_0 = 0$ and $T = 0$. Varying c has no effect on Δ_c when $T = 0$. (c) $c = 1$ and $T = 0$. Decreasing J_0 increases the hue selectivity even when varying c has no effect, indicating that c is not the only source of hue selectivity.

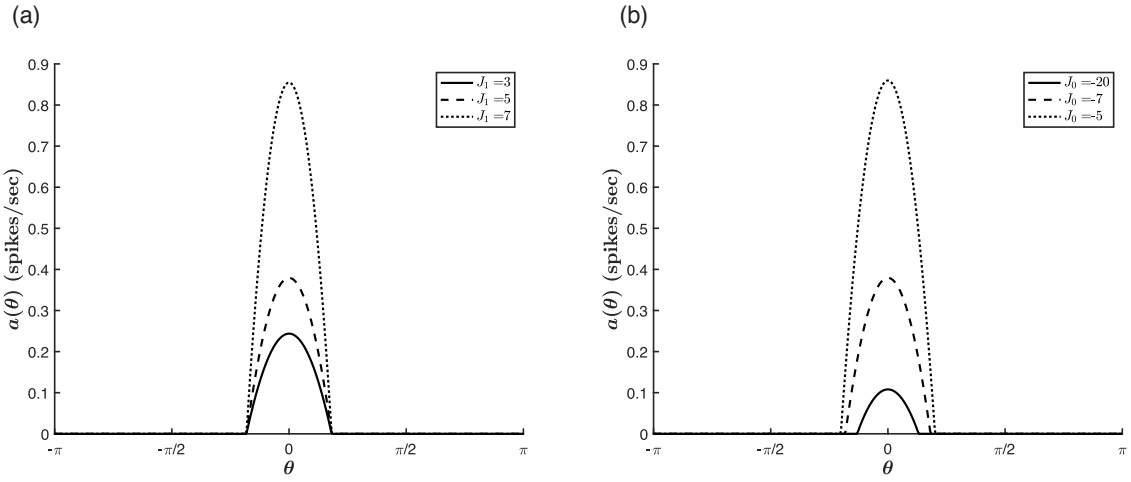

Figure 3.19: The sources of hue selectivity: the roles of J_0 and J_1. $\bar{\theta} = 0$, $\beta = 1$, $c = 1$, and $T = 0$. (a) $J_0 = -7$. Varying J_1 has no effect on Δ_c, indicating that it is not the only source of hue selectivity. (b) $J_1 = 5$. In the same parameter regime, J_0 has a pronounced effect on Δ_c.

Ultimately, the orientation model sets up a dichotomy between two specific regions of parameter space. In the non-marginal case, c is the primary player in the tuning mechanism and in the marginal case, this role belongs to J_2. The uniform inhibition is thus given a secondary "sharpening" role. By contrast, in choosing a fully anisotropic h_{lgn}, the color model does not encompass an analogous marginal phase with an always-dominating J_1. Rather, even for large J_1, the uniform inhibition is at least equally important to the modulation of the tuning width. In fact, as we have shown in section 3.4, for larger values of c, J_0 is more effective than J_1 in narrowing the tuning curves, for both the analytical and extended regimes.

We thus stress that the two regimes, though analogous to those of the orientation model, do not constitute a division in the hue processing mechanism. Rather, recall from section 3.3 that we define the boundary between the analytical and extended regimes solely by

whether or not the linear case exists. It is therefore determined by the values of J_0 and J_1 for which the linear solution applies, given that the values of c, T, and β keep the input above threshold throughout the dynamics. Again, we note that for each combination of J_0 and J_1 within the analytical regime there exists also a nonlinear case, in which $h(\theta, t)$ is cut off by the thresholding nonlinearity and, thereby, the linear solution does not apply. This definition differs from that of the orientation model, which demarcates the boundary between the homogeneous and marginal phases based on the emergent steady-state tuning curves alone. For more on this approach, see the discussion of the broad and narrow profiles in [45]. As we will see in the following section, the boundary is integral to the corresponding stability analysis of the steady-state tuning curves.

3.6 Stability Analysis

To analyze the stability of the emergent tuning curves, we turn once more to our separable activity ansatz assumed in the eigenfunction decomposition of equation 3.5. This means that we are faced again with a nonlinearity-induced coupling of the time-dependent coefficients and, consequently, the intractability of the associated stability analysis. We thus proceed as before, presenting first a closed-form stability analysis in the model's linear regime, which will serve as the backdrop to the numerical approach we use in the general nonlinear case.

3.6.1 Stability of the Linear Case

Approaching the question of stability through the lens of linear stability analysis, we begin by adding a small perturbation $\delta a(\theta, t)$ to the steady-state tuning curve to see if the resulting activity,

$$a(\theta, t) = a_\infty(\theta) + \delta a(\theta, t), \tag{3.41}$$

is driven back to the same curve. Substitution into 2.11, with $a_\infty = \beta(h(\theta,t) - T)$, then yields the following equation for the perturbation dynamics:

$$\tau_0 \frac{d\delta a(\theta,t)}{dt} = -\delta a(\theta,t) + \beta \int_{-\pi}^{\pi} w(\theta - \theta')\delta a(\theta',t) d\theta'. \tag{3.42}$$

Expanding the perturbation in the Fourier eigenbasis,

$$\delta a(\theta,t) = \sum_{\mu} D_\mu(t)\hat{e}_\mu(\theta), \tag{3.43}$$

and taking the inner product with $\hat{e}_\nu(\theta)$, we obtain a system of equations for the uncoupled evolution of the eigenmodes:

$$\begin{aligned}
\tau_0 \frac{dD_0(t)}{dt} &= (2\pi\beta J_0 - 1)D_0(t) \\
\tau_0 \frac{dD_1(t)}{dt} &= (\pi\beta J1 - 1)D_1(t) \\
\tau_0 \frac{dD_{\text{-}1}(t)}{dt} &= (\pi\beta J1 - 1)D_{\text{-}1}(t) \\
\tau_0 \frac{dD_\nu(t)}{dt} &= -D_\nu(t) \;\forall\; |\nu| > 1.
\end{aligned} \tag{3.44}$$

Here we can see that the higher order modes, $|\nu| > 1$, always decay, so that the stability of a_∞ is completely determined by the growth or decay of the first-order perturbations. The relevant Jacobian matrix thus reads:

$$\mathbb{J}_{lin} = \begin{bmatrix} \tilde{\lambda}_0 & 0 & 0 \\ 0 & \tilde{\lambda}_{+1} & 0 \\ 0 & 0 & \tilde{\lambda}_{-1} \end{bmatrix}, \tag{3.45}$$

where $\tilde{\lambda}_0 = 2\pi\beta J_0 - 1$ and $\tilde{\lambda}_{\pm 1} = \pi\beta J_1 - 1$. The perturbation decays if each of the Jacobian

matrix eigenvalues, $\tilde{\lambda}_\nu$, is negative, so that the tuning curve $a_\infty(\theta)$ is stable for

$$\begin{aligned} J_0 &< \frac{1}{2\pi\beta} \\ J_1 &< \frac{1}{\pi\beta}. \end{aligned} \tag{3.46}$$

These stability conditions on J_0 and J_1 are also evident in the linear solution 3.37 derived above, which, in addition to the local stability revealed by the perturbation analysis, shows that a tuning curve satisfying 3.46 is asymptotically stable, attracting the activity profile from any initial condition [79, 91]. Recall that 3.46 also sets the boundary of the analytical regime, defined above as the (J_0, J_1) parameter subspace which permits a linear solution.

3.6.2 Linear Stability Analysis of the General Model

While we do not have an analytical solution for the general nonlinear model, and definitely not one so easy to interpret as 3.37, we may nonetheless set up the Jacobian matrix for a numerical analysis of the local stability. We thus begin from the same starting point as in the linear case, adding a small perturbation of the form 3.43 and substituting the resulting activity into 2.1. The eigenmodes then evolve according to the following equation for the coefficients D_μ (see Appendix A):

$$\tau_0 \frac{dD_\nu(t)}{dt} = -D_\nu(t) + \beta \int_{\delta_1^*}^{\delta_2^*} \left[\delta q_0(t) + \delta q_{\mathrm{R}}(t)\cos(\phi) + \delta q_{\mathrm{I}}(t)\sin(\phi)\right] \hat{e}_\nu^*(\phi) d\phi, \tag{3.47}$$

where δ_1^* and δ_2^* are the critical cutoff angles of the steady-state solution, obtained numerically in the method of section 3.1.1 (see Appendix B). Unlike in the linear case, we cannot make a general statement about the growth or decay of the higher-order coefficients $D_{|\nu|>1}(t)$. However, we observe that the integrand of 3.47 is a function of D_0, $D_{\text{-}1}^R$, and $D_{\text{-}1}^I$ alone, and, as such, the stability of the steady-state tuning curve is completely determined by the stability of these first-order coefficients.

Evaluating the integrals for $\nu = 0$ and $\nu = -1$, and noting that

$$\begin{aligned}
\delta q_0 &= \sqrt{2\pi} J_0 \delta c_0 \equiv \sqrt{2\pi} J_0 D_0 \\
\delta q_{\mathrm{R}} &= \sqrt{2\pi} J_1 \delta c_{\text{-}1}^R \equiv \sqrt{2\pi} J_1 D_{\text{-}1}^R \\
\delta q_{\mathrm{I}} &= \sqrt{2\pi} J_1 \delta c_{\text{-}1}^I \equiv \sqrt{2\pi} J_1 D_{\text{-}1}^I
\end{aligned} \tag{3.48}$$

from 3.12, we obtain the following system of equations for the evolution of the characteristic coefficients:

$$\begin{aligned}
\tau_0 \frac{dD_0}{dt} &= \big[\beta J_0(\delta_2^* - \delta_1^*) - 1\big] D_0 + \big[\beta J_1(\sin\delta_2^* - \sin\delta_1^*)\big] D_{\text{-}1}^R \\
&\quad + \big[\beta J_1(\cos\delta_1^* - \cos\delta_2^*)\big] D_{\text{-}1}^I \\
\tau_0 \frac{dD_{\text{-}1}^R}{dt} &= \big[\beta J_0(\sin\delta_2^* - \sin\delta_1^*)\big] D_0 + \big[\tfrac{\beta J_1}{4}\big(2\delta_2^* - 2\delta_1^* + \sin(2\delta_2^*) - \sin(2\delta_1^*)\big) - 1\big] D_{\text{-}1}^R \\
&\quad + \big[\tfrac{\beta J_1}{4}\big(\cos(2\delta_1^*) - \cos(2\delta_2^*)\big)\big] D_{\text{-}1}^I \\
\tau_0 \frac{dD_{\text{-}1}^I}{dt} &= \big[\beta J_0(\cos\delta_1^* - \cos\delta_2^*)\big] D_0 + \big[\tfrac{\beta J_1}{4}\big(\cos(2\delta_1^*) - \cos(2\delta_2^*)\big)\big] D_{\text{-}1}^R \\
&\quad + \big[\tfrac{\beta J_1}{4}\big(2\delta_2^* - 2\delta_1^* + \sin(2\delta_1^*) - \sin(2\delta_2^*)\big) - 1\big] D_{\text{-}1}^I
\end{aligned} \tag{3.49}$$

The corresponding Jacobian matrix is thus

$$\mathbb{J} = \begin{bmatrix}
\beta J_0(\delta_2^* - \delta_1^*) - 1 & \beta J_1(\sin\delta_2^* - \sin\delta_1^*) & \\
\beta J_0(\sin\delta_2^* - \sin\delta_1^*) & \tfrac{\beta J_1}{4}\big(2\delta_2^* - 2\delta_1^* + \sin(2\delta_2^*) - \sin(2\delta_1^*)\big) - 1 & \dots \\
\beta J_0(\cos\delta_1^* - \cos\delta_2^*) & \tfrac{\beta J_1}{4}\big(\cos(2\delta_1^*) - \cos(2\delta_2^*)\big) & \\
 & \beta J_1(\cos\delta_1^* - \cos\delta_2^*) & \\
 & \tfrac{\beta J_1}{4}\big(\cos(2\delta_1^*) - \cos(2\delta_2^*)\big) & \\
 & \tfrac{\beta J_1}{4}\big(2\delta_2^* - 2\delta_1^* + \sin(2\delta_1^*) - \sin(2\delta_2^*)\big) - 1
\end{bmatrix}. \tag{3.50}$$

Note that its entries may be equally obtained from the right-hand side of the general

system of equations 3.18 for the global network dynamics, as follows:

$$\mathbb{J} = \begin{bmatrix} \frac{\partial f_1}{\partial c_0} & \frac{\partial f_1}{\partial c_{\text{-}1}^R} & \frac{\partial f_1}{\partial c_{\text{-}1}^I} \\ \frac{\partial f_2}{\partial c_0} & \frac{\partial f_2}{\partial c_{\text{-}1}^R} & \frac{\partial f_2}{\partial c_{\text{-}1}^I} \\ \frac{\partial f_3}{\partial c_0} & \frac{\partial f_3}{\partial c_{\text{-}1}^R} & \frac{\partial f_3}{\partial c_{\text{-}1}^I} \end{bmatrix}_{c_0^*,\, c_{\text{-}1}^{R\,*},\, c_{\text{-}1}^{I\,*}} \tag{3.51}$$

where the first-order partial derivatives are evaluated at the steady-state values of c_0, $c_{\text{-}1}^R$, and $c_{\text{-}1}^I$ [91]. The stability of the tuning curve is then determined by the eigenvalues of $\mathbb{J}$.

3.6.3 Numerical Stability Analysis

Graphically, we see that the activity drives to the same steady-state tuning curves for varying initial conditions, or with the addition of small perturbations, as illustrated in figure 3.20. Furthermore, as in the linear case, we note that the existence of such a steady state is a function of the cortical strengths J_0 and J_1. By fixing the values of β, c, $\bar{\theta}$, and T, we are left with a two-parameter family of differential equations, allowing us to analyze this dependence numerically in the associated (J_0, J_1) parameter space.

Carrying out a parameter sweep across this space, we find that the system features a bifurcation curve, below which the model permits steady-state solutions and above which no equilibrium exists. To determine stability within the former region, we compute $\mathbb{J}$ at the emergent steady-state tuning curves of various points in the parameter space. Solving the associated characteristic equations, we observe that the eigenvalues are always real and negative, and thus conclude that **all emergent steady-state tuning curves are stable**.

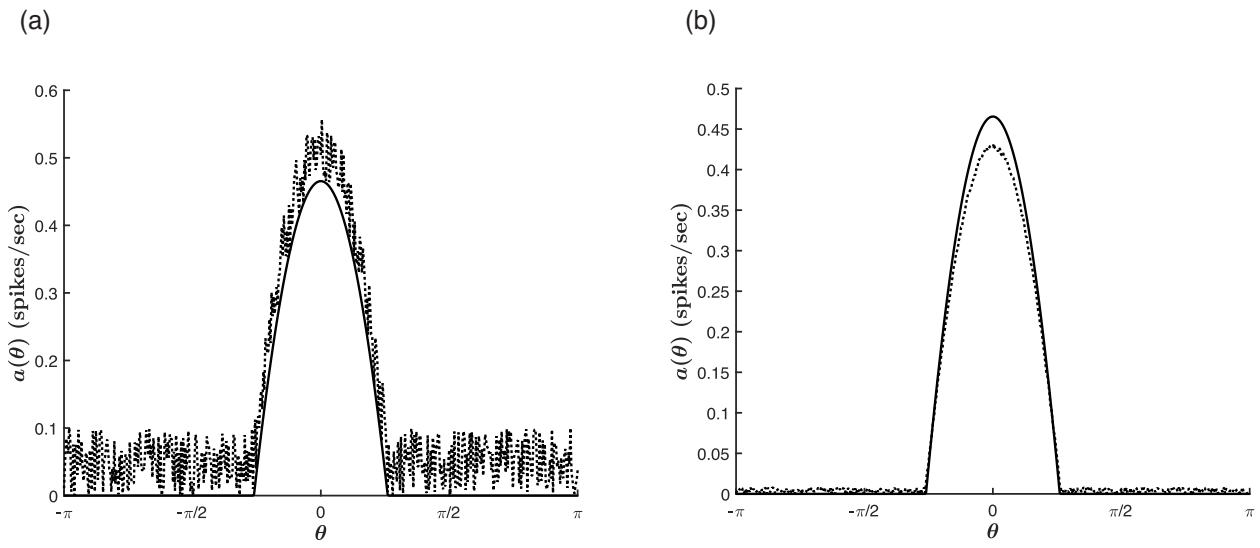

Figure 3.20: Numerical stability analysis for an emergent tuning curve. For $c = 1$, $\bar{\theta} = 0$, $\beta = 1$, $T = 0$, $J_0 = -2$, $J_1 = 1$, and $dt = .1$. The parameters are chosen to produce a weak network activity in order to better illustrate the dynamics after a small ($0 \leq \Delta a(\theta) \leq .1$) perturbation to the steady state. (a) The emergent steady-state tuning curve (solid line) and the network activity after the addition of a random perturbation at each hue angle (dotted line). (b) After 25 timesteps the activity (dotted line) has decayed below the tuning curve, before being driven back to the same steady-state tuning curve as in (a) (solid line).

Figure 3.21 shows the bifurcation diagrams for two families of equations, distinguished by their values for T. Most notable is the *extended regime*, which permits stable steady-state solutions beyond the boundary set by 3.46. As this parameter regime is not accessible to the linear solution, the tuning curves in this regime are necessarily a product of the thresholding nonlinearity and are thus always cut off below $|\theta| = \pi$. The thresholding nonlinearity therefore not only expands the region of stability, but also ensures that the tuning curves emerging within the extended regime are selective for hue. As noted in sections 3.4.2 and 3.5, this expansion is pivotal when the external input is weak and the anisotropic cortical

strength plays the larger role in narrowing the tuning curves. Furthermore, regardless of input strength, it allows for a larger overall network response, as the peak activity, $a_\infty(\bar{\theta})$, grows with increasing J_1. Finally, as we will see in section 3.7, in the absence of any stimulus (i.e., for $c = 0$), the extended regime features the spontaneous generation of stable tuning curves and may thus serve as the bedrock for color hallucinations.

However, looking back at figure 3.21, perhaps most striking is the horizontal portion of the bifurcation curve at $J_0 = \frac{1}{2\pi\beta}$ for $J_1 < \frac{1}{\pi\beta}$, which sets the same stability conditions on J_0 and J_1 as in the linear case. This is despite the fact that, as detailed in section 3.3, many of the points in the analytical regimes of the two featured families correspond to solutions that implement thresholding, thus signifying that the analytical regime is not an exclusively *linear* one.

The key to understanding the shape of this region lies in noticing that the bifurcation diagram does not change for varying values of c, T, and $\bar{\theta}$, as shown in figure 3.21 for the two values of T. The stability conditions on J_0 and J_1 are thus uniquely determined by β alone. Furthermore, for the general diagram (i.e., with β fixed and c, T unfixed), each point of the analytical regime permits linear solutions (satisfying equation 3.39), in addition to the ones that implement thresholding. Accordingly, the uniqueness of the bifurcation diagram implies that at each point of the analytical (J_0, J_1) subspace, the stability of the latter, nonlinear solutions is equivalent to that of the linear solutions. This means that the boundary at $J_0 = \frac{1}{2\pi\beta}$ set by 3.46 applies to the full, nonlinear model as well.

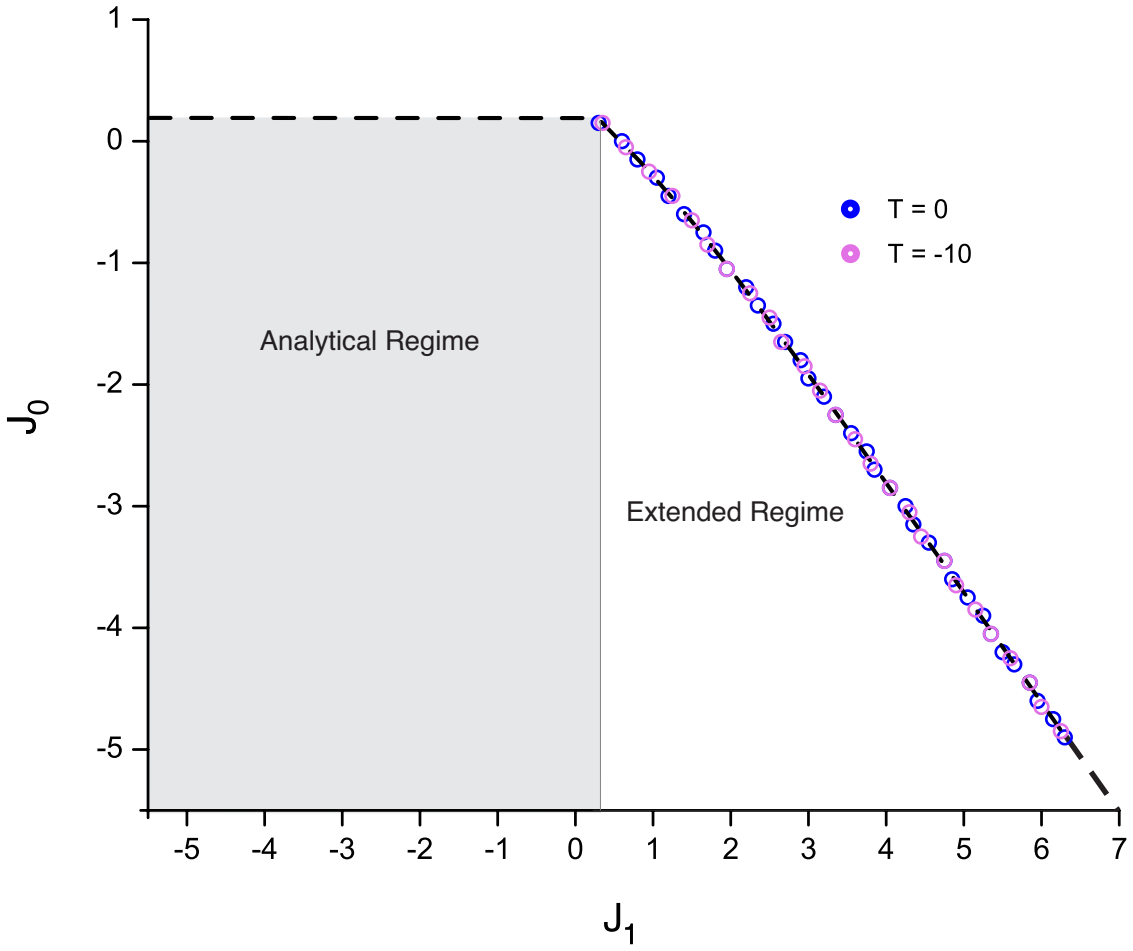

Figure 3.21: Bifurcation diagram for $\beta = 1$ and $c = 1$ for two values of threshold (shown in the legend). The grey and white regions correspond to the analytical and extended regimes, respectively. The black dashed line is the bifurcation curve, above which the tuning curves are unstable. Overlaid open circles correspond to points tested in a parameter sweep over the extended regime. Notably, the parameter sweep produces the same bifurcation curve for both values of T. Here, we must note that for critical values of T, for which the input is not large enough to generate activity, the model permits the trivial $a(\theta) = 0$ steady-state solution in both the analytical and extended regimes. This solution, however, is unstable to perturbations large enough to make the input cross the threshold. For more on bifurcation theory in the context of neural fields, see [41, 46]. See also [45] for an analogous "phase diagram" analysis in the orientation Ring Model.

3.7 A Turing Mechanism for Color Hallucinations

3.7.1 Biological Turing Patterns

Underpinning our hue tuning model is the mathematics of reaction-diffusion systems, for which, in particular, Alan Turing's treatment of biological pattern formation offers many valuable insights [94]. The general Turing mechanism assumes a system of two interacting chemicals, whose local reaction and long-range diffusion properties govern the dynamics of their relative concentrations. In the original framework these chemicals are termed "morphogens" to elicit their form-producing capabilities within a developing embryo, whose anatomical structure emerges as a result of their underlying concentration dynamics. This, for instance, may be attributed to the morphogens' catalysis of organ formation in different parts of the developing organism.

Most analogous to our model is the formulation which distributes the morphogens across a continuous ring of tissue, parameterized by the cellular position θ. Assuming that the system never deviates far from the underlying homogeneous steady state, the two dynamical state equations for their concentrations, X and Y, take the linear form

$$\begin{aligned} \frac{dX(\theta,t)}{dt} &= aX(\theta,t) + bY(\theta,t) + D_X\nabla^2 X(\theta,t) \\ \frac{dY(\theta,t)}{dt} &= cX(\theta,t) + dY(\theta,t) + D_Y\nabla^2 Y(\theta,t), \end{aligned} \tag{3.52}$$

where a, b, c, and d represent the chemical reaction rates, and D_X and D_Y are the diffusion rates of X and Y, respectively. Here, we set a, $c > 0$, so that increasing the concentration of X activates the production of both X and Y, and b, $d < 0$ so that Y has an inhibitory effect on the production of both chemicals [49].

In the absence of diffusion (i.e., with $D_X = D_Y = 0$), the system has a homogeneous steady-state solution, $(X, Y) = 0$, whose stability is determined by a Jacobian composed

of the reaction rates, $\left[\begin{smallmatrix} a & b \\ c & d \end{smallmatrix}\right]$, and hence by the system's local chemical properties alone [49]. Note that at this point the system is circularly symmetric with respect to interchanging any two cells on the ring.

Assuming the existence of a stable steady-state solution, and therefore the corresponding requirements on a-d, we next set the diffusive terms $D_X, D_Y > 0$, taking the separable ansatz for the general solution:

$$X = \sum_{\mu=-\infty}^{\infty} A_\mu e^{\lambda_\mu t} e^{i\mu\theta}$$
$$Y = \sum_{\mu=-\infty}^{\infty} B_\mu e^{\lambda_\mu t} e^{i\mu\theta}. \tag{3.53}$$

Furthermore, we set $D_X < D_Y$ to generate the local excitation and lateral inhibition of the morphogen concentrations [49, 73], evoking the connectivity function ansatz 2.9. The underlying steady state then remains stable if the real parts of the eigenvalues λ_μ, obtained from the modified Jacobian, are negative. With a-d fixed from the stability conditions above, these eigenvalues are functions of the diffusion parameters alone. Thus, the conditions for stability may be thought of in terms of a bifurcation diagram in the (D_X, D_Y) phase space, comparable to figure 3.21.

From here, a set of additional conditions may be placed on D_X and D_Y so that the system undergoes a Turing bifurcation, wherein at least one λ_μ becomes positive and the homogeneous steady state loses its stability. With the addition of a small random perturbation, the instability results in the growth of the corresponding eigenmodes $e^{i\mu\theta}$, such that, over time, 3.53 is dominated by the eigenmodes with largest λ_μ. These represent stationary waves whose wavelengths are set by the circumference of the ring (i.e., by the spatial properties of the medium) and whose growth is bounded by the higher-order terms which had been initially ignored in the near-equilibrium formulation [73, 81, 94]. The underlying circular symmetry is thus broken and a spatial pattern is formed.

In his seminal paper, Turing extrapolated this mechanism to explain various biological phenomena, such as the development of petals on a flower, spotted color patterns, and the growth of an embryo along various directions from an original spherical state. A hallmark of each of these examples is that there is no input into the system so that each of the emergent patterns reflect a mechanism of spontaneous symmetry breaking, onset by a perturbation of "some influences unspecified" [94]. In light of this, we ask, can the visual cortex self-generate the perception of hue?

3.7.2 Spontaneous Symmetry Breaking and Color Hallucinations

To assess our model's ability to self-organize in the absence of visual input, we set $c = 0$ and seek to establish the presence of a Turing mechanism marked by the following three features:

1. A system comprised of local excitation and long-range inhibition.

2. Spontaneous symmetry breaking in the absence of input within a region of a parameter space defined by the relevant bifurcation parameter(s).

3. The emergence of patterns that are bound by the system's nonlinearities.

As noted above, requiring $D_X < D_Y$ in 3.52 sets up the diffusion-driven activator-inhibitor dynamics governing the evolution of the morphogen concentration across the ring of cells. With these assumptions, Turing's reaction-diffusion equations bear a strong resemblance to our one-population generalization of the excitatory and inhibitory color cell dynamics in the absence of LGN input:

$$\tau_0 \frac{da(\theta,t)}{dt} = -a(\theta,t) + g\left[\int_{-\pi}^{\pi} \left(J_0 + J_1 \cos(\theta - \theta')\right) a(\theta',t) d\theta'\right], \tag{3.54}$$

where the local excitation and long-range inhibition are incorporated in the anisotropic interaction term $J_1 \cos(\theta - \theta')$, and the reaction terms $aX(\theta,t)$, $bY(\theta,t)$, $cX(\theta,t)$, and $dY(\theta,t)$

find their neural analogue in the term $-a(\theta, t)$. Importantly, the notions of "local" and "long-range" here describe interactions in the DKL space, and not in the *physical* cortical space correlate to Turing's ring of tissue. Accordingly, we treat J_1 as the Turing bifurcation parameter and look for spontaneous color tuning beyond a bifurcation point $J_1 = J_1^T$. Additionally, we observe that the onset of instability is determined by a critical value of T, so that the relevant parameter space for our exploration is (J_1, T) (Fig. 3.22). This analysis is summarized by figure 3.23.

We observe that within the analytical regime, the system generates a stable homogeneous steady-state solution $a_\infty(\theta) \geq 0$ for all values of the parameters β, T, J_0, and J_1 (panels a-b). As such, from the closed-form linear steady-state solution 3.38, we obtain

$$a_\infty(\theta) = \begin{cases} -\dfrac{\beta T}{1 - 2\pi\beta J_0} & \text{for } T \leq 0 \\ 0 & \text{for } T > 0. \end{cases} \tag{3.55}$$

We further observe that beyond $J_1 = \frac{1}{\pi\beta}$, a stable homogeneous steady-state solution remains at $a_\infty(\theta) = 0$ for $T \geq 0$ (panel c). However, at $T = 0$, this radial symmetry is broken, and the cortex generates spontaneous tuning curves with peak locations determined by the random initial conditions (panels d-f). Thus, the system bifurcates when $J_1 = \frac{1}{\pi\beta}$ and $T = 0$, permitting the onset of color hallucinations in a region defined by these two values (Fig. 3.22).

Bearing these predictions in mind, we point to a recent functional MRI study of blind patients experiencing visual hallucinations [43]. The study attributes these visions to the activation of the neural networks underlying normal vision, precipitated by the hyper-excitability of the cortex to spontaneous resting-state activity fluctuations when it is deprived of external input. This is suggestive of the required lowering of neuronal threshold at the onset of color hallucinations predicted here. Notably, a reduction in membrane potential threshold has also been attributed to the action of hallucinogens [25, 97].

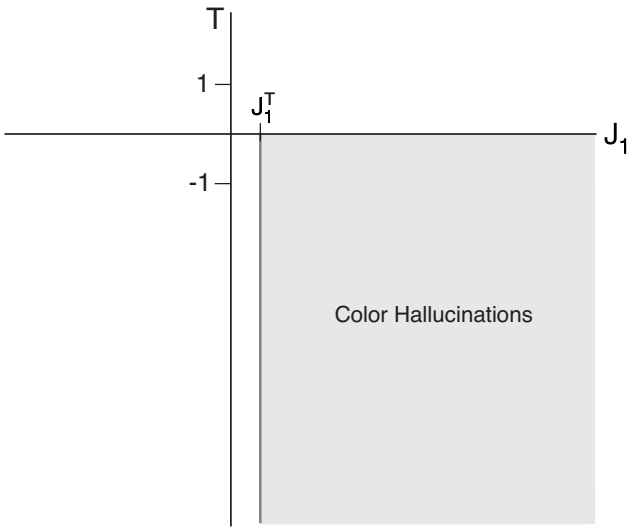

Figure 3.22: The onset of color hallucinations in the (J_1, T) parameter space. The model generates spontaneous hue tuning curves beyond $J_1 = J_1^T \equiv \frac{1}{\pi\beta}$ and below $T = 0$.

Finally, we note that the stability of the emergent tuning curves is determined by the bifurcation diagram of figure 3.21. This means that, in addition to expanding the region of stability in the presence of chromatic stimuli, the model's nonlinearity allows for *stable*, spontaneous color hallucinations in their absence. This is most starkly seen with a comparison to the emergent curves obtained with the linear model (equation 2.11), which grow without bound for the same parameter values (Fig. 3.24).

Having thus established a Turing-like mechanism for our model's self-organization, we end with an analogy to Turing's original diffusion-driven formulation. In his concluding example, Turing applies the mechanism to explain the growth of an embryo along various axes of its original spherical state. This growth is driven by diffusion, directed by the "disturbing influences," shaped by the system's chemical and physical properties, and bounded by the system's nonlinearities. It is all too clear to see the parallels with our hue tuning model, wherein a hallucination is driven by the anisotropy of the cortical interactions, its hue determined by the initial conditions, its selectivity shaped by the cortical parameters, and its stability ensured by the thresholding nonlinearity.

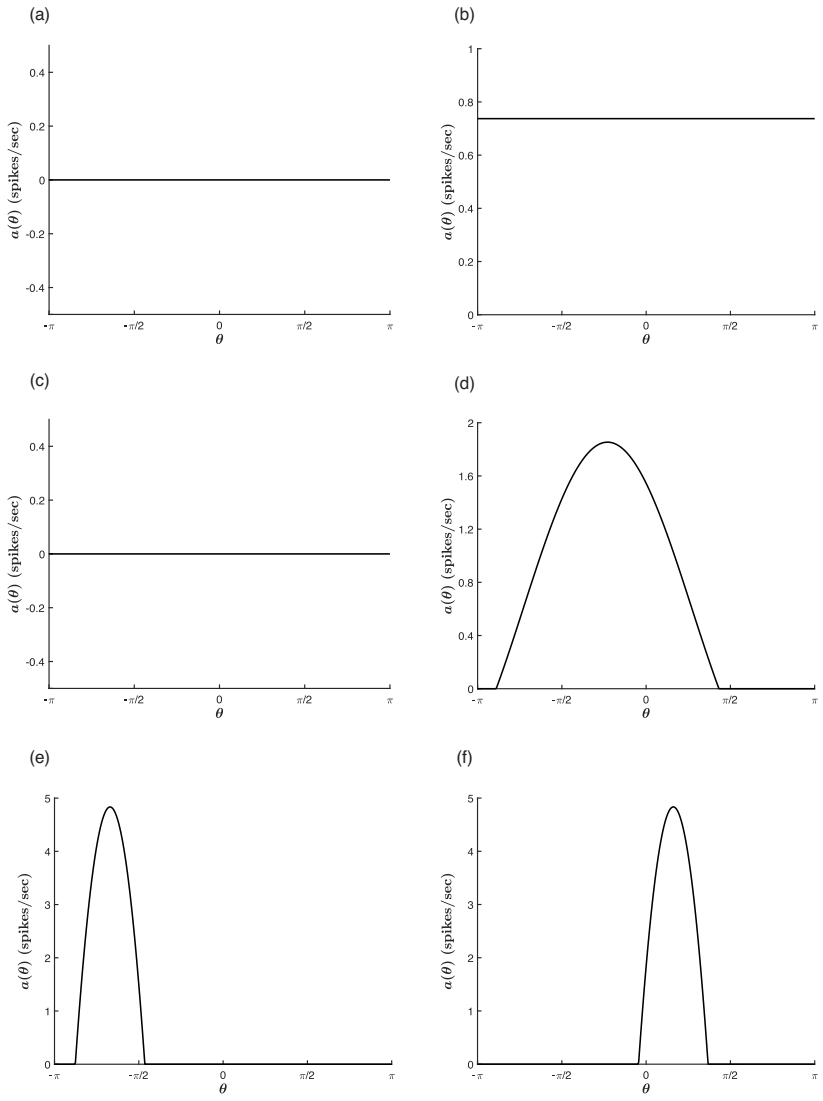

Figure 3.23: Spontaneous pattern formation in the absence of input ($c = 0$). $\beta = 1$. (a)-(b): $J_0 = -2$, $J_1 = .1$ (a) $T = 0$ (b) For $T < 0$, the value of the homogeneous steady-state activity increases. Here, $T = -10$. (c)-(d): Pattern formation in the extended regime $J_0 = -2$, $J_1 = .4$. (c) No hue tuning curve emerges for $T \geq 0$. Here, $T = 0$. (d) $T = -10$. A hue tuning curve is generated in the absence of external input. (e)-(f): $T = -10$, $J_0 = -7$, $J_1 = 6$. The emergent tuning curve is more selective for larger values of J_1. For each run, the activity is peaked about a different angle, set by the random initial conditions. The peak value and tuning width are consistent between trials.

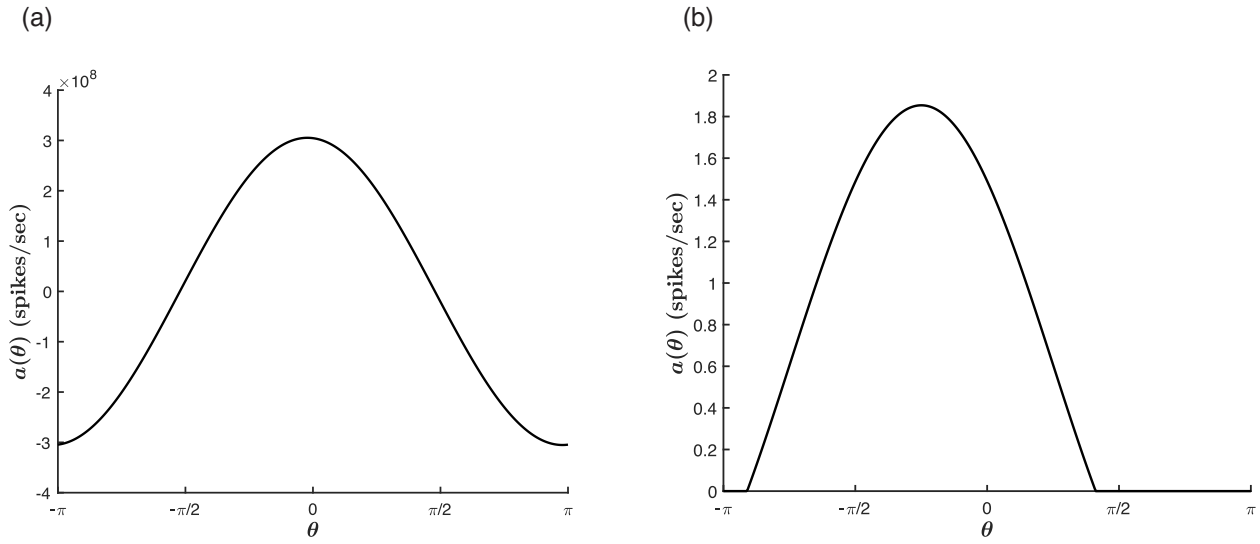

Figure 3.24: Stability of Spontaneous Tuning Curves. With $\beta = 1$, $T = -10$, $J_0 = -2$, and $J_1 = .4$, the tuning curves generated in the linear model (equation 2.11) are unstable (a), while those generated by the full model (equation 2.1) are stable (b). Panels a and b show the emergent activity after equal durations of time and for the same parameter values. Note that, as a point of contrast, the linear model demonstrates the stabilizing role of the thresholding nonlinearity. As such, it is pictured here for illustrative purposes alone, so that the negative activity values in panel a should not be given a physical interpretation.

CHAPTER 4

CONCLUSION

This dissertation presents a neural field model of color vision processing which reconceptualizes the link between chromatic stimuli and our perception of hue. It does so guided by the premise that the visual cortex initiates the mixing of the cardinal L−M and S−(L+M) pathways and thereby transforms the discrete cone-opponent signals to a continuous representation of chromatic information. We emphasize that this modeling assumption is based on experimental evidence. Just as it is not obvious that the brain should break apart a photon's chromatic information in its earliest processing stages, neither is it implicit that it should be reintegrated in V1. Such mixing mechanisms have been implemented by previous combinatorial models of color processing, though through a largely feed-forward approach.

Our theory bears in mind the mixing mechanism, but reframes the stage-wise combinatorial scheme to one based on the nonlinear population dynamics within the visual cortex. Accordingly, we propose a hue-based cortical connectivity, built upon the cortical hue map micro-architecture revealed by recent optical imaging studies of V1. By considering the intracortical network interactions, we have accounted for V1 cells responsive to the gamut of DKL directions without the need to fine-tune the cortical parameters. We do so without restricting to a particular category of V1 neuron, as both single-opponent and double-opponent, and altogether novel types of cells, have been pegged as the primary messengers of chromatic information. Rather, we zoom out of the individual neuron's receptive field to model the aggregate, population-level properties and, in particular, the stable representation of hue. We thereby offer that chromatic processing in the visual cortex is, in its essence, a self-organizing system of neuronal-activity pattern formation, capable of encoding chromatic information in the presence of visual stimuli and generating information in their absence.

Further, in assuming modularity for chromatic processing, we have not ruled out a mechanism for joint feature processing. Our choice to focus on the unoriented color cells within

the CO blob regions allowed us to parse out the chromatic pathway for an independent analysis, but should not be interpreted as a claim about its functional independence. We leave open the question of the functional and anatomical separation of the various visual streams.

Finally, we emphasize that the emergent hue tuning curves we have characterized are a network property reflective of the *physiological* neuronal responses, and should not be confounded with our *perception* of hue. By recognizing that the hue tuning mechanism of the visual cortex is an early stop in the visual pathway, we hope that this research inspires further field theory approaches to our understanding of color perception.

APPENDIX A

MATHEMATICAL SUPPLEMENT

This appendix details to a greater extent the analysis in chapter 3.

A.1 Reformulating the Input

Given that the activity $a(\theta, t)$ is a real-valued function, $c_0 \in \mathbb{R}$ and $c_1 = c_{\text{-}1}^*$. The recurrent terms of 3.7 can then be rewritten as:

$$\begin{aligned} h_{\text{ctx}}(\theta, t) &= \lambda_0\, c_0(t)\, \hat{e}_0(\theta) + \lambda_{\text{-}1}\big(c_{\text{-}1}(t)\, \hat{e}_{\text{-}1}(\theta) + c_{\text{-}1}^*(t)\, \hat{e}_1(\theta)\big) \\ &= \tfrac{1}{\sqrt{2\pi}}\Big\{\lambda_0\, c_0(t) + \lambda_{\text{-}1}\big[(c_{\text{-}1}^R(t) + ic_{\text{-}1}^I(t))(\cos\theta - i\sin\theta) \\ &\qquad + (c_{\text{-}1}^R(t) - ic_{\text{-}1}^I(t))(\cos\theta + i\sin\theta)\big]\Big\} \\ &= \tfrac{1}{\sqrt{2\pi}}\Big\{\lambda_0\, c_0(t) + 2\lambda_{\text{-}1}\big[(c_{\text{-}1}^R(t)\cos\theta + c_{\text{-}1}^I(t)\sin\theta)\big]\Big\}. \end{aligned} \tag{A.1}$$

Combining A.1 with the cone-opponent formulation of the feedforward input 2.5 and the substitutions of 3.12 yields:

$$h(\theta, t) = q_0(t) + q_{\text{R}}(t)\cos(\theta) + q_{\text{I}}(t)\sin(\theta) \tag{A.2}$$

which we reexpress as

$$h(\theta, t) = q_0(t) + \text{Re}\big[(q_{\text{R}} - iq_{\text{I}})e^{i\theta}\big]. \tag{A.3}$$

We then let $q_{\text{R}}(t) - iq_{\text{I}}(t) = c_h(t)e^{i\gamma(t)}$ with $c_h(t) = \sqrt{q_{\text{R}}^2(t) + q_{\text{I}}^2(t)}$ and $\tan(\gamma(t)) = -\frac{q_{\text{I}}(t)}{q_{\text{R}}(t)}$

to reexpress $h(\theta, t)$ in the form

$$\begin{aligned} h(\theta, t) &= q_0(t) + \mathrm{Re}\big[c_h(t) e^{i(\gamma+\theta)}\big] \\ &= q_0(t) + c_h(t)\cos[\theta + \gamma(t)] \end{aligned} \tag{A.4}$$

A.2 Fourier Analysis of Linear Steady-State Solution

In this section I provide an alternate approach to the steady-state solution of the linear case of our model (section 3.3). The methods here draw on the work of [45] in their analysis of steady-state orientation tuning curves (see [21] for more details).

From 3.31, we have $a_\infty(\theta) = g[h_\infty(\theta)]$. Defining $h_\infty(\theta)$ as in 3.7 in terms of the steady-state values of the coefficients, $c_\nu(\infty)$, gives

$$h_\infty(\theta) = \lambda_{\text{-}1}\, c_{\text{-}1}(\infty)\, \hat{e}_{\text{-}1}(\theta) + \lambda_0\, c_0(\infty)\, \hat{e}_0(\theta) + \lambda_1\, c_1(\infty)\, \hat{e}_1(\theta) + c\cos(\theta - \bar{\theta}). \tag{A.5}$$

Here, we recall from 3.5 that the coefficients c_ν are the first-order Fourier coefficients of $a_\infty(\theta)$, defined on the interval $\{-\pi, \pi\}$, where we assume values for the cortical parameters such that the steady-state input is above threshold for all DKL angles and the profile is not cut off by the action of g. This allows us to make use of the orthogonality of the Fourier eigenfunctions on $\{-\pi, \pi\}$.

The coefficients are thus defined as

$$\begin{aligned} c_0(\infty) &= \frac{1}{\sqrt{2\pi}} \int_{-\pi}^{\pi} \beta(h_\infty(\theta) - T) d\theta \\ c_{\text{-}1}(\infty) &= \frac{1}{\sqrt{2\pi}} \int_{-\pi}^{\pi} \beta(h_\infty(\theta) - T) e^{i\theta} d\theta \\ c_1(\infty) &= \frac{1}{\sqrt{2\pi}} \int_{-\pi}^{\pi} \beta(h_\infty(\theta) - T) e^{-i\theta} d\theta, \end{aligned} \tag{A.6}$$

where the prefactors preceding the integrals take into account the normalization factor in $\hat{e}_\nu$

such that $c_\nu = \alpha_\nu \int_{-\pi}^{\pi} \Big(\sum_\mu c_\mu(t) \hat{e}_\mu(\theta) \Big) e^{-i\nu\theta} d\theta$ for normalization constants α_ν.

Substitution of A.5 into A.6 then yields

$$c_0(\infty) = \frac{-\sqrt{2\pi} T\beta}{1 - 2\pi\beta J_0}$$

$$c_{\text{-}1}(\infty) = \frac{\sqrt{\frac{\pi}{2}}\beta c e^{i\bar{\theta}}}{1 - \pi\beta J_1}$$

$$c_1(\infty) = \frac{\sqrt{\frac{\pi}{2}}\beta c e^{-i\bar{\theta}}}{1 - \pi\beta J_1},$$

where I have used $\lambda_0 = 2\pi J_0$ and $\lambda_1 = \lambda_{\text{-}1} = \pi J_1$.

Finally, I rewrite 3.31 with these expressions for c_ν to obtain the steady-state profile:

$$\begin{aligned} a_\infty(\theta) &= \beta \left[\lambda_0 \frac{-T\beta}{1 - 2\pi\beta J_0} + \lambda_{\text{-}1} \frac{\frac{1}{2}\beta c e^{i(-\theta+\bar{\theta})}}{1 - \pi\beta J_1} + \lambda_1 \frac{\frac{1}{2}\beta c e^{i(\theta-\bar{\theta})}}{1 - \pi\beta J_1} - T + c\cos(\theta - \bar{\theta}) \right], \\ &= -\frac{\beta T}{1 - 2\pi\beta J_0} + \frac{c\beta\cos(\theta - \bar{\theta})}{1 - \pi\beta J_1}, \end{aligned} \tag{A.7}$$

as in 3.38.

A.3 Linear Stability Analysis

This section presents the mathematical details for obtaining equation 3.47.

Adding a small perturbation $\delta a(\theta, t)$ to the steady-state tuning curve and substituting the resulting network activity 3.41 into 2.1, we obtain:

$$\tau_0 \frac{d\delta a(\theta,t)}{dt} = -\big(a_\infty(\theta) + \delta a(\theta,t)\big) + \beta\big(h_\infty(\theta) + \delta h(\theta,t) - T\big)\mathcal{H}\big(h_\infty(\theta) + \delta h(\theta,t) - T\big), \tag{A.8}$$

where $\delta h(\theta, t)$ is a perturbation to the input due to $\delta a(\theta, t)$. Taylor expanding the right-hand

side of A.8 in $h(\theta,t) \equiv h_\infty(\theta) + \delta h(\theta,t)$ about $h(\theta,t) = h_\infty(\theta)$ then yields

$$\tau_0 \frac{d\delta a(\theta,t)}{dt} = -\big(a_\infty(\theta) + \delta a(\theta,t)\big) + \beta\Big\{\big(h_\infty(\theta) - T\big)\mathcal{H}\big(h_\infty(\theta) - T\big) + \delta h(\theta,t)\mathcal{H}\big(h_\infty(\theta) - T\big) + O\big((\delta h(\theta,t))^2\big)\Big\}. \quad \text{(A.9)}$$

For small perturbations, the higher-order terms in $\delta h(\theta,t)$ are negligible, and, using $a_\infty(\theta) = \beta\big(h_\infty(\theta) - T\big)\mathcal{H}\big(h_\infty(\theta) - T\big)$, we rewrite A.9 as

$$\tau_0 \frac{d\delta a(\theta,t)}{dt} = -\delta a(\theta,t) + \beta\delta h(\theta,t)\mathcal{H}\big(h_\infty(\theta) - T\big). \quad \text{(A.10)}$$

Next, expanding $\delta a(\theta,t)$ as in 3.43, we obtain

$$\tau_0 \sum_{-\infty}^{\infty} \frac{dD_\mu(t)}{dt}\hat{e}_\mu(\theta) = -\sum_{-\infty}^{\infty} D_\mu(t)\hat{e}_\mu(\theta) + \beta\delta h(\theta,t)\mathcal{H}\big(h_\infty(\theta) - T\big), \quad \text{(A.11)}$$

wherein we express $\delta h(\theta,t)$ in the formulation of A.2 to yield:

$$\tau_0 \sum_{-\infty}^{\infty} \frac{dD_\mu(t)}{dt}\hat{e}_\mu(\theta) = -\sum_{-\infty}^{\infty} D_\mu(t)\hat{e}_\mu(\theta) + \beta\big[\delta q_0(t) + dq_{\mathrm{R}}(t)\cos(\theta) + \delta q_{\mathrm{I}}(t)\sin(\theta)\big]\mathcal{H}\big(h_\infty(\theta) - T\big). \quad \text{(A.12)}$$

Finally, taking the inner product of A.12 with $\hat{e}_\nu(\theta)$, and recalling from section 3.1.1 that the action of the Heaviside function may be reformulated in terms of the critical cutoff angles δ_1 and δ_2, we arrive at

$$\tau_0 \frac{dD_\nu(t)}{dt} = -D_\nu(t) + \beta \int_{\delta_1^*}^{\delta_2^*} \left[\delta q_0(t) + \delta q_{\mathrm{R}}(t)\cos(\phi) + \delta q_{\mathrm{I}}(t)\sin(\phi)\right] \hat{e}_\nu^*(\phi)d\phi, \quad \text{(A.13)}$$

where δ_1^* and δ_2^* are the steady-state values of the cutoff angles.

APPENDIX B

MATLAB CODE

B.1 Numerical Solution for Steady-State Coefficients

This is the Matlab code for computing the coefficients $c^*_{|\mu|\leq 1}$ as described in section 3.2.2.

```
%% ---------------------- Parameters ----------------------
n = 501;   % number of hue-preferring populations
phi180 = -pi:2*pi/(n-1):pi;   % range of hue preferences
beta = 1;   % gain (spikes/sec/mV)
Rrest = .2;   % initial firing rate (sp/s)
tau = 1;   % membrane time constant (ms)
dt = .1;   % simulation time step (ms)
duration = 900;   % number of steps
J0 = -2;   % isotropic connectivity strength
J1 = 3;   % anisotropic connectivity strength
c = 1;   % strength of LGN signal (mV)
th = 0;   % hue angle of stimulus
l_m = cos(th);   % projection of hue angle onto the L-M axis
s = sin(th);   % projection of hue angle onto the S-(L+M) axis
T = 0;   % threshold (mV)
%% ---- Computing the Steady State Fourier Coefficients ----
a = Rrest*rand(1,n);   % random initial activity profile
% Use Composite Simpson's Rule to obtain first-order Fourier
   components of initial activity profile.
im=sqrt(-1);
m=-1;
```

```
hsum=exp(-im*phi180(1)*m)*a(1)+exp(-im*phi180(1)*m)*a(n);
for k =2:n-1
    if rem(k,2)==0
        hsum=hsum+exp(-im*phi180(k)*m)*a(k)*4;
    else
        hsum=hsum+exp(-im*phi180(k)*m)*a(k)*2;
    end
end
coeff=hsum*(2*pi/(n-1))/3;
normcoeff1=coeff/sqrt(2*pi);   % initial value of c_{-1}
cr=real(normcoeff1);   % initial value of c_{-1, real}
ci=imag(normcoeff1);   % initial value of c_{-1, imag}
m=0;
hsum=exp(-im*phi180(1)*m)*a(1)+exp(-im*phi180(1)*m)*a(n);
for k =2:n-1
    if rem(k,2)==0
        hsum=hsum+exp(-im*phi180(k)*m)*a(k)*4;
    else
        hsum=hsum+exp(-im*phi180(k)*m)*a(k)*2;
    end
end
coeff=hsum*(2*pi/(n-1))/3;
c0=coeff/sqrt(2*pi);   % initial value of c_{0}
% Relevant variable values computed as described in chapter 3.
qr=c*l_m+sqrt(2*pi)*J1*cr;
qi=c*s+sqrt(2*pi)*J1*ci;
```

```
47 ch=sqrt(qr^2+qi^2);
48 q0=sqrt(2*pi)*J0*c0;
49 alpha= (T-q0)/ch;
50 theta2=acos(alpha);
51 theta1=-theta2;
52 gamma=atan(-qi/qr);
53 if alpha<-1
54   delta1=-pi;
55   delta2=pi;
56 elseif alpha>1
57   delta1=0;
58   delta2=0;
59 else
60   delta1=theta1-gamma;
61   delta2=theta2-gamma;
62 end
63 % Use Forward Euler to compute steady state values of c_{0}, c_
     {-1, real}, and c_{-1, imag}, updating variables at every
     timestep.
64 for i = 1: duration
65     c0=c0-c0*dt+dt*beta/sqrt(2*pi)*(ch*(sin(delta2+gamma)-sin(
         delta1+gamma))+(T-q0)*(delta1-delta2));
66     cr=cr-cr*dt+dt*beta/sqrt(2*pi)*(ch/2*((delta2-delta1)+sin(
         delta2-delta1))+2*(T-q0)*sin(gamma+delta1))*cos(gamma);
67     ci=ci-ci*dt-dt*beta/sqrt(2*pi)*(ch/2*((delta2-delta1)+sin(
         delta2-delta1))+2*(T-q0)*sin(gamma+delta1))*sin(gamma);
```

```
68      qr=c*l_m+sqrt(2*pi)*J1*cr;
69      qi=c*s+sqrt(2*pi)*J1*ci;
70      ch=sqrt(qr^2+qi^2);
71      q0=sqrt(2*pi)*J0*c0;
72      alpha=(T-q0)/ch;
73      theta2=acos(alpha);
74      theta1=-theta2;
75      gamma=atan(-qi/qr);
76      if alpha<-1
77          delta1=-pi;
78          delta2=pi;
79      elseif alpha>1
80          delta1=0;
81          delta2=0;
82      else
83      delta1=theta1-gamma;
84      delta2=theta2-gamma;
85      end
86  end
```

B.2 Numerical Solution and Stability Analysis

This is the Matlab code for plotting the activity dynamics and steady-state profile, computing the first-order Fourier coefficients of the network activity, and performing a linear stability analysis of the steady state.

```
%% ---------------------- Parameters ----------------------
n = 501;   % number of hue-preferring populations
phi180 = -pi:2*pi/(n-1):pi;   % range of hue preferences
beta = 1;   % gain (spikes/sec/mV)
Rrest = .2;   % initial firing rate maximum
tau = 1;   % membrane time constant (ms)
dt = .1;   % simulation timestep (ms)
duration = 500;   % number of steps
J0 = -2;   % isotropic connectivity strength
J1 = 3;   % anisotropic connectivity strength
c = 1;   % strength of LGN signal (mV)
th = 0;   % hue angle of stimulus
l_m = cos(th);   % projection of hue angle onto the L-M axis
s = sin(th);   % projection of hue angle onto the S-(L+M) axis
T = 0;   % threshold (mV)
%% -------------------- LGN Input -----------------------
% Tuned Stimulus Condition:
lgn = c*(l_m*cos(phi180)+s*sin(phi180));
Rlgnmovie = ones(duration,1)*lgn;
% Zero Input Condition:
% Rlgnmovie = zeros(duration,1)*lgn;
%% ------------------- Initialization -------------------
```

```
% Random Initial Conditions:
a = Rrest*rand(1,n);   % current network activity (spikes/sec)
Rmovie = a;   % matrix of network activity from t=0 to t=
   duration+1.
% Isotropic Initial Conditions:
% a = Rrest*ones(1,n);
% Rmovie = a;
rhs = zeros(1,n);   % right-hand side of model equation
%% ---------------------- Dynamics ----------------------
for t=1:duration
    Vctx=zeros(1,n);   % net cortical input (mV)
    %  Use Simpson's Rule to obtain cortical input at current
       timestep.
    for i=1:n
        hsum=(J0+J1*cos(phi180(i)-phi180(1)))*a(1)+(J0+J1*cos(
           phi180(i)-phi180(n)))*a(n);
        for k =2:n-1
            if rem(k,2)==0
               hsum=hsum+(J0+J1*cos(phi180(i)-phi180(k)))*a(k)
                  *4;
            else
               hsum=hsum+(J0+J1*cos(phi180(i)-phi180(k)))*a(k)
                  *2;
            end
        end
       Vctx(i)=hsum*(2*pi/(n-1))/3;
```

```
    end
    h=Rlgnmovie(t,:)+Vctx;    % total input (mV)
    % Apply thresholding and evaluate RHS.
    for k = 1:n
        if h(k)>T
            rhs(k)=-a(k)+beta*(h(k)-T);
        else
            rhs(k)=-a(k);
        end
    end
     % Compute the activity and update the activity matrix.
     a=a+rhs*(dt/tau);
     Rmovie(t+1,:)=a;
end
% Plot the network activity dynamics.
figure;
for m=1:duration
    plot(phi180,Rmovie(m,:));
    hold on;
    pause(.01);
end
% Plot the steady state profile.
figure;
plot(phi180, Rmovie(duration+1,:),'black','linewidth',2);
box off;
ax=gca;
```

```
xlim([-pi pi]);
xticks(-pi:pi/2:pi);
xticklabels({'-\pi','-\pi/2','0','\pi/2','\pi'});
ax.LineWidth=1.5;
ax.FontSize=14;
as.FontWeight='bold';
xlabel('\boldmath${\theta}$','Fontsize', 18,'Interpreter','
   latex');
ylabel('\boldmath $a(\theta)$ \bf{(spikes/sec)}','Fontsize',
   18, 'Interpreter','latex');
set(gcf,'color','w');
%% ---------------- Perturbation Analysis ----------------
% Add a random perturbation to the steady state activity and
   update the activity array.
Rmovie(duration+2,:)=Rmovie(duration+1,:)+.1*rand(1,n).*Rmovie(
   duration,:);
a=Rmovie(duration+2,:);
% Reset matrix to reflect peturbation dynamics and proceed with
    Forward Euler method as above.
Rmovie=a;
for t=1:duration
    for i=1:n
        hsum=(J0+J1*cos(phi180(i)-phi180(1)))*a(1)+(J0+J1*cos(
           phi180(i)-phi180(n)))*a(n);
        for k=2:n-1
            if rem(k,2)==0
```

```
90                  hsum=hsum+(J0+J1*cos(phi180(i)-phi180(k)))*a(k)
                        *4;
91              else
92                  hsum=hsum+(J0+J1*cos(phi180(i)-phi180(k)))*a(k)
                        *2;
93              end
94          end
95         Vctx(i)=hsum*(2*pi/(n-1))/3;
96      end
97      h=Rlgnmovie(t,:)+Vctx;
98      for k = 1:n
99          if h(k)>T
100             rhs(k)=-a(k)+beta*(h(k)-T);
101         else
102             rhs(k)=-a(k);
103         end
104     end
105     a = a + rhs*(dt/tau);
106     Rmovie(t+1,:)= a;
107 end
108 % Plot the dynamics.
109 figure;
110 for m=1:duration
111     plot(phi180,Rmovie(m,:));
112     hold on;
113     pause(.01);
```

```
114 end
115 % Plot the steady state profile.
116 figure;
117 plot(phi180, Rmovie(duration+1,:),'black','linewidth',2);
118 box off;
119 ax = gca;
120 xlim([-pi pi]);
121 xticks(-pi:pi/2:pi);
122 xticklabels({'-\pi','-\pi/2','0','\pi/2','\pi'});
123 ax.LineWidth=1.5;
124 ax.FontSize=14;
125 as.FontWeight='bold';
126 xlabel('\boldmath${\theta}$','Fontsize', 18,'Interpreter','
      latex');
127 ylabel('\boldmath $a(\theta)$ \bf{(spikes/sec)}','Fontsize',
      18, 'Interpreter','latex');
128 set(gcf,'color','w');
129 %% ---- Computing the First-Order Fourier Coefficients ----
130 % Use the Composite Simpson's Rule to compute c_{-1}.
131 im=sqrt(-1); m=-1;
132 hsum=exp(-im*phi180(1)*m)*a(1)+exp(-im*phi180(1)*m)*a(n);
133 for k =2:n-1
134     if rem(k,2)==0
135         hsum=hsum+exp(-im*phi180(k)*m)*a(k)*4;
136     else
137         hsum=hsum+exp(-im*phi180(k)*m)*a(k)*2;
```

```
138     end
139 end
140 coeff=hsum*(2*pi/(n-1))/3;
141 normcoeff1=coeff/sqrt(2*pi);   % normalized c_{-1}
142 % Use the Composite Simpson's Rule to compute c_{0}.
143 m=0;
144 hsum=exp(-im*phi180(1)*m)*a(1)+exp(-im*phi180(1)*m)*a(n);
145 for k =2:n-1
146     if rem(k,2)==0
147         hsum=hsum+exp(-im*phi180(k)*m)*a(k)*4;
148     else
149         hsum=hsum+exp(-im*phi180(k)*m)*a(k)*2;
150     end
151 end
152 coeff=hsum*(2*pi/(n-1))/3;
153 normcoeff0=coeff/sqrt(2*pi);   % normalized c_{0}
154 %% -------------- Linear Stability Analysis --------------
155 % Compute the Jacobian at the steady state to analyze stability
      of emergent tuning curve. Relevant variable values computed
      as described in chapter 3.
156 c1real=real(normcoeff1); c1imag=imag(normcoeff1);
157 qr=c*cos(th)+J1*sqrt(2*pi)*c1real;
158 qi=c*sin(th)+J1*sqrt(2*pi)*c1imag;
159 ch=sqrt(qr^2+qi^2);
160 q0=sqrt(2*pi)*J0*normcoeff0;
161 alpha= (T-q0)/ch;
```

```
theta2=acos(alpha); theta1=-theta2;
gamma=atan(-qi/qr);
if alpha<-1
    delta1=-pi;
    delta2=pi;
elseif alpha>1
    delta1=0;
    delta2=0;
else
    delta1=theta1-gamma;
    delta2=theta2-gamma;
end
stab0_a=[beta*J0*(delta2-delta1)-1; beta*J1*(sin(delta2)-sin(
   delta1)); beta*J1*(cos(delta1)-cos(delta2))];
stabr_a=[beta*J0*(sin(delta2)-sin(delta1)); beta*J1/4*(2*delta2
   -2*delta1+sin(2*delta2)-sin(2*delta1))-1; beta*J1/4*(cos(2*
   delta1)-cos(2*delta2))];
stabi_a=[beta*J0*(cos(delta1)-cos(delta2)); beta*J1/4*(cos(2*
   delta1)-cos(2*delta2)); beta*J1/4*(2*delta2-2*delta1+sin(2*
   delta1)-sin(2*delta2))-1];
stab_mat=[stab0_a stabr_a stabi_a]';   % Jacobian matrix
syms x
poly_stab=charpoly(stab_mat,x);   % characteristic polynomial
eigen_stab=double(solve(poly_stab))   % Solve characteristic
   equation to obtain eigenvalues of the Jacobian.
```

REFERENCES

[1] Shun-ichi Amari. Dynamics of pattern formation in lateral-inhibition type neural fields. *Biological Cybernetics*, 27(2):77–87, 1977.

[2] Eyal Bartfeld and Amiram Grinvald. Relationships between orientation-preference pinwheels, cytochrome oxidase blobs, and ocular-dominance columns in primate striate cortex. *Proceedings of the National Academy of Sciences*, 89(24):11905–11909, 1992.

[3] Rani Ben-Yishai, Ruth Lev Bar-Or, and Haim Sompolinsky. Theory of orientation tuning in visual cortex. *Proceedings of the National Academy of Sciences*, 92(9):3844–3848, 1995.

[4] William H. Bosking, Ying Zhang, Brett Schofield, and David Fitzpatrick. Orientation selectivity and the arrangement of horizontal connections in tree shrew striate cortex. *Journal of Neuroscience*, 17(6):2112–2127, 1997.

[5] Paul C. Bressloff. Spatially periodic modulation of cortical patterns by long-range horizontal connections. *Physica D: Nonlinear Phenomena*, 185(3-4):131–157, 2003.

[6] Paul C. Bressloff and Jack D. Cowan. The visual cortex as a crystal. *Physica D: Nonlinear Phenomena*, 173(3-4):226–258, 2002.

[7] Paul C. Bressloff and Jack D. Cowan. The functional geometry of local and horizontal connections in a model of V1. *Journal of Physiology-Paris*, 97(2-3):221–236, 2003.

[8] Paul C. Bressloff and Jack D. Cowan. A spherical model for orientation and spatial–frequency tuning in a cortical hypercolumn. *Philosophical Transactions of the Royal Society of London. Series B: Biological Sciences*, 358(1438):1643–1667, 2003.

[9] Paul C. Bressloff, Jack D. Cowan, Martin Golubitsky, Peter J. Thomas, and Matthew C. Wiener. Geometric visual hallucinations, Euclidean symmetry and the functional architecture of striate cortex. *Philosophical Transactions of the Royal Society of London. Series B: Biological Sciences*, 356(1407):299–330, 2001.

[10] Joshua W. Brown. The tale of the neuroscientists and the computer: why mechanistic theory matters. *Frontiers in Neuroscience*, 8:349, 2014.

[11] Ed Bullmore and Olaf Sporns. The economy of brain network organization. *Nature Reviews Neuroscience*, 13(5):336–349, 2012.

[12] Matteo Carandini and David Ferster. Membrane potential and firing rate in cat primary visual cortex. *Journal of Neuroscience*, 20(1):470–484, 2000.

[13] Matteo Carandini and Dario L. Ringach. Predictions of a recurrent model of orientation selectivity. *Vision Research*, 37(21):3061–3071, 1997.

[14] Carson C. Chow and Yahya Karimipanah. Before and beyond the Wilson–Cowan equations. *Journal of Neurophysiology*, 123(5):1645–1656, 2020.

[15] Bevil R. Conway. Spatial structure of cone inputs to color cells in alert macaque primary visual cortex (V-1). *Journal of Neuroscience*, 21(8):2768–2783, 2001.

[16] Bevil R. Conway. Color vision, cones, and color-coding in the cortex. *The Neuroscientist*, 15(3):274–290, 2009.

[17] Bevil R. Conway, Rhea T. Eskew Jr., Paul R. Martin, and Andrew Stockman. A tour of contemporary color vision research. *Vision Research*, 151:2–6, 2018.

[18] Bevil R. Conway, Sebastian Moeller, and Doris Y. Tsao. Specialized color modules in macaque extrastriate cortex. *Neuron*, 56(3):560–573, 2007.

[19] Blake J. Cook, Andre D. H. Peterson, Wessel Woldman, and John R. Terry. Neural field models: A mathematical overview and unifying framework. *Mathematical Neuroscience and Applications*, 2, 2022.

[20] Dennis M. Dacey, Joanna D. Crook, and Orin S. Packer. Distinct synaptic mechanisms create parallel S-ON and S-OFF color opponent pathways in the primate retina. *Visual Neuroscience*, 31(2):139–151, 2014.

[21] Peter Dayan and L. F. Abbott. *Theoretical Neuroscience: Computational and Mathematical Modeling of Neural Systems*. MIT Press, 2001.

[22] Abhishek De and Gregory D. Horwitz. Spatial receptive field structure of double-opponent cells in macaque V1. *Journal of Neurophysiology*, 125(3):843–857, 2021.

[23] Russell L. De Valois, Nicolas P. Cottaris, Sylvia D. Elfar, Luke E. Mahon, and J. Anthony Wilson. Some transformations of color information from lateral geniculate nucleus to striate cortex. *Proceedings of the National Academy of Sciences*, 97(9):4997–5002, 2000.

[24] Russell L. De Valois and Karen K. De Valois. A multi-stage color model. *Vision Research*, 33(8):1053–1065, 1993.

[25] Cato M. H. de Vos, Natasha L. Mason, and Kim P. C. Kuypers. Psychedelics and neuroplasticity: a systematic review unraveling the biological underpinnings of psychedelics. *Frontiers in Psychiatry*, 12:724606, 2021.

[26] Andrew M. Derrington, John Krauskopf, and Peter Lennie. Chromatic mechanisms in lateral geniculate nucleus of macaque. *The Journal of Physiology*, 357(1):241–265, 1984.

[27] Andrew J. Elliot, Mark D. Fairchild, and Anna Franklin. Introduction and overview. In Andrew J. Elliot, Mark D. Fairchild, and Anna Franklin, editors, *Handbook of Color Psychology*, pages 1–6. Cambridge University Press, 2015.

[28] Bard Ermentrout. Neural networks as spatio-temporal pattern-forming systems. *Reports on Progress in Physics*, 61(4):353–430, 1998.

[29] Bard Ermentrout and Jack D. Cowan. A mathematical theory of visual hallucination patterns. *Biological Cybernetics*, 34(3):137–150, 1979.

[30] Rhea T. Eskew Jr. Higher order color mechanisms: a critical review. *Vision Research*, 49(22):2686–2704, 2009.

[31] Mark D. Fairchild. Color models and systems. In Andrew J. Elliot, Mark D. Fairchild, and Anna Franklin, editors, *Handbook of Color Psychology*, pages 9–26. Cambridge University Press, 2015.

[32] Olivier D. Faugeras, Anna Song, and Romain Veltz. Spatial and color hallucinations in a mathematical model of primary visual cortex. *Comptes Rendus. Mathématique*, 360:59–87, 2022.

[33] Katie A. Ferguson and Jessica A. Cardin. Mechanisms underlying gain modulation in the cortex. *Nature Reviews Neuroscience*, 21(2):80–92, 2020.

[34] Howard S. Friedman, Hong Zhou, and Rüdiger von der Heydt. The coding of uniform colour figures in monkey visual cortex. *The Journal of Physiology*, 548(2):593–613, 2003.

[35] Anupam K. Garg, Peichao Li, Mohammad S. Rashid, and Edward M. Callaway. Color and orientation are jointly coded and spatially organized in primate primary visual cortex. *Science*, 364(6447):1275–1279, 2019.

[36] Karl R. Gegenfurtner. Cortical mechanisms of colour vision. *Nature Reviews Neuroscience*, 4(7):563–572, 2003.

[37] Karl R. Gegenfurtner and Robert Ennis. Color vision II: higher-order color processing. In Andrew J. Elliot, Mark D. Fairchild, and Anna Franklin, editors, *Handbook of Color Psychology*, pages 70–109. Cambridge University Press, 2015.

[38] Apostolos P. Georgopoulos, Masato Taira, and Alexander Lukashin. Cognitive neurophysiology of the motor cortex. *Science*, 260(5104):47–52, 1993.

[39] Peter Gouras. Color vision. In Helga Kolb, Ralph Nelson, Eduardo Fernandez, and Bryan Jones, editors, *The Organization of the Retina and Visual System*. 2011.

[40] Olivia Gozel and Brent Doiron. Between-area communication through the lens of within-area neuronal dynamics. *bioRxiv*, 2022.

[41] Thilo Gross. Not one, but many critical states: a dynamical systems perspective. *Frontiers in Neural Circuits*, 15:614268, 2021.

[42] Boris Gutkin, David Pinto, and Bard Ermentrout. Mathematical neuroscience: from neurons to circuits to systems. *Journal of Physiology-Paris*, 97(2-3):209–219, 2003.

[43] Avital Hahamy, Meytal Wilf, Boris Rosin, Marlene Behrmann, and Rafael Malach. How do the blind 'see'? The role of spontaneous brain activity in self-generated perception. *Brain*, 144(1):340–353, 2021.

[44] Akitoshi Hanazawa, Hidehiko Komatsu, and Ikuya Murakami. Neural selectivity for hue and saturation of colour in the primary visual cortex of the monkey. *European Journal of Neuroscience*, 12(5):1753–1763, 2000.

[45] David Hansel and Haim Sompolinksy. Modeling feature selectivity in local cortical circuits. In Christof Koch and Idan Segev, editors, *Methods in Neuronal Modeling: From Ions to Networks*, pages 499–567. MIT Press, 2nd edition, 1998.

[46] Janina Hesse and Thilo Gross. Self-organized criticality as a fundamental property of neural systems. *Frontiers in Systems Neuroscience*, 8:166, 2014.

[47] John J. Hopfield. Neurons with graded response have collective computational properties like those of two-state neurons. *Proceedings of the National Academy of Sciences*, 81(10):3088–3092, 1984.

[48] Gregory D. Horwitz. What studies of macaque monkeys have told us about human color vision. *Neuroscience*, 296:110–115, 2015.

[49] Rebecca Hoyle. *Pattern Formation: An Introduction to Methods*. Cambridge University Press, 2006.

[50] David H. Hubel and Margaret S. Livingstone. Color and contrast sensitivity in the lateral geniculate body and primary visual cortex of the macaque monkey. *Journal of Neuroscience*, 10(7):2223–2237, 1990.

[51] David H. Hubel and Torsten N. Wiesel. Uniformity of monkey striate cortex: a parallel relationship between field size, scatter, and magnification factor. *Journal of Comparative Neurology*, 158(3):295–305, 1974.

[52] Dorothea Jameson and Leo M. Hurvich. Some quantitative aspects of an opponent-colors theory. I. Chromatic responses and spectral saturation. *JOSA*, 45(7):546–552, 1955.

[53] Elizabeth N. Johnson, Michael J. Hawken, and Robert Shapley. The spatial transformation of color in the primary visual cortex of the macaque monkey. *Nature Neuroscience*, 4(4):409–416, 2001.

[54] Elizabeth N. Johnson, Michael J. Hawken, and Robert Shapley. Cone inputs in macaque primary visual cortex. *Journal of Neurophysiology*, 91(6):2501–2514, 2004.

[55] Elizabeth N. Johnson, Michael J. Hawken, and Robert Shapley. The orientation selectivity of color-responsive neurons in macaque V1. *Journal of Neuroscience*, 28(32):8096–8106, 2008.

[56] Deane B. Judd. Response functions for types of vision according to the Müller theory. *Journal of Research of the National Bureau of Standards*, 42(RP1946), 1949.

[57] Peter K. Kaiser and Robert M. Boynton. *Human Color Vision*. Optical Society of America, 2nd edition, 1996.

[58] Sung Soo Kim, Hervé Rouault, Shaul Druckmann, and Vivek Jayaraman. Ring attractor dynamics in the drosophila central brain. *Science*, 356(6340):849–853, 2017.

[59] Heinrich Klüver. *Mescal and Mechanisms of Hallucinations*. The University of Chicago Press, 1966.

[60] Helga Kolb. S-cone pathways. In Helga Kolb, Ralph Nelson, Eduardo Fernandez, and Bryan Jones, editors, *The Organization of the Retina and Visual System*. 2011.

[61] Carole E. Landisman and Daniel Y. Ts'o. Color processing in macaque striate cortex: electrophysiological properties. *Journal of Neurophysiology*, 87(6):3138–3151, 2002.

[62] Carole E. Landisman and Daniel Y. Ts'o. Color processing in macaque striate cortex: relationships to ocular dominance, cytochrome oxidase, and orientation. *Journal of Neurophysiology*, 87(6):3126–3137, 2002.

[63] Sidney R. Lehky and Terrence J. Sejnowski. Seeing white: Qualia in the context of decoding population codes. *Neural Computation*, 11(6):1261–1280, 1999.

[64] Peter Lennie, John Krauskopf, and Gary Sclar. Chromatic mechanisms in striate cortex of macaque. *Journal of Neuroscience*, 10(2):649–669, 1990.

[65] Ming Li, Fang Liu, Mikko Juusola, and Shiming Tang. Perceptual color map in macaque visual area V4. *Journal of Neuroscience*, 34(1):202–217, 2014.

[66] Peichao Li, Anupam K. Garg, Li A. Zhang, Mohammad S. Rashid, and Edward M. Callaway. Functional organization for color appearance mechanisms in primary visual cortex. *bioRxiv*, 2020.

[67] Ye Liu, Ming Li, Xian Zhang, Yiliang Lu, Hongliang Gong, Jiapeng Yin, Zheyuan Chen, Liling Qian, Yupeng Yang, Ian M. Andolina, Stewart Shipp, Niall Mcloughlin, Shiming Tang, and Wei Wang. Hierarchical representation for chromatic processing across macaque V1, V2, and V4. *Neuron*, 108(3):538–550.e5, 2020.

[68] Margaret S. Livingstone and David H. Hubel. Anatomy and physiology of a color system in the primate visual cortex. *Journal of Neuroscience*, 4(1):309–356, 1984.

[69] Haidong D. Lu and Anna W. Roe. Functional organization of color domains in V1 and V2 of macaque monkey revealed by optical imaging. *Cerebral Cortex*, 18(3):516–533, 2008.

[70] Paria Mehrani, Andrei Mouraviev, and John K. Tsotsos. Multiplicative modulations enhance diversity of hue-selective cells. *Scientific Reports*, 10(1):1–15, 2020.

[71] Angie M. Michaiel, Philip R. L. Parker, and Cristopher M. Niell. A hallucinogenic serotonin-2a receptor agonist reduces visual response gain and alters temporal dynamics in mouse V1. *Cell Reports*, 26(13):3475–3483, 2019.

[72] J. D. Mollon and Gabriele Jordan. On the nature of unique hues. In David Carden, Christine Dickinson, and Ian Murray, editors, *John Dalton's Colour Vision Legacy*, pages 381–392. Taylor & Francis, 1997.

[73] James D. Murray. *Mathematical Biology II: Spatial Models and Biomedical Applications*. Springer, 3rd edition, 2003.

[74] Ian Nauhaus, Kristina J. Nielsen, Anita A. Disney, and Edward M. Callaway. Orthogonal micro-organization of orientation and spatial frequency in primate primary visual cortex. *Nature Neuroscience*, 15(12):1683–1690, 2012.

[75] Sara S. Patterson, Maureen Neitz, and Jay Neitz. S-cone circuits in the primate retina for non-image-forming vision. In *Seminars in Cell & Developmental Biology*. Elsevier, 2021.

[76] Jonathan R. Polimeni, Domhnull Granquist-Fraser, Richard J. Wood, and Eric L. Schwartz. Physical limits to spatial resolution of optical recording: clarifying the spatial structure of cortical hypercolumns. *Proceedings of the National Academy of Sciences*, 102(11):4158–4163, 2005.

[77] Emilio Salinas and Laurence F. Abbott. A model of multiplicative neural responses in parietal cortex. *Proceedings of the National Academy of Sciences*, 93(21):11956–11961, 1996.

[78] Matthias F. Valverde Salzmann, Andreas Bartels, Nikos K. Logothetis, and Almut Schüz. Color blobs in cortical areas V1 and V2 of the new world monkey Callithrix jacchus, revealed by non-differential optical imaging. *Journal of Neuroscience*, 32(23):7881–7894, 2012.

[79] Hiroki Sayama. *Introduction to the modeling and analysis of complex systems*. Open SUNY Textbooks, 2015.

[80] Denis Schluppeck and Stephen A. Engel. Color opponent neurons in V1: a review and model reconciling results from imaging and single-unit recording. *Journal of Vision*, 2(6):480–492, 2002.

[81] Christian Scholz. *Morphology of experimental and simulated Turing patterns*. PhD thesis, 2009.

[82] Robert Shapley. Physiology of color vision in primates. In *Oxford Research Encyclopedia of Neuroscience*. 2019.

[83] Robert Shapley and Michael J. Hawken. Color in the cortex: single- and double-opponent cells. *Vision Research*, 51(7):701–717, 2011.

[84] Steven K. Shevell and Paul R. Martin. Color opponency: tutorial. *JOSA A*, 34(7):1099–1108, 2017.

[85] Elena Y. Smirnova, Ekaterina A. Chizhkova, and Anton V. Chizhov. A mathematical model of color and orientation processing in V1. *Biological Cybernetics*, 109(4):537–547, 2015.

[86] Samuel G. Solomon and Peter Lennie. The machinery of colour vision. *Nature Reviews Neuroscience*, 8(4):276–286, 2007.

[87] David C. Somers, Sacha B. Nelson, and Mriganka Sur. An emergent model of orientation selectivity in cat visual cortical simple cells. *Journal of Neuroscience*, 15(8):5448–5465, 1995.

[88] Anna Song, Olivier Faugeras, and Romain Veltz. A neural field model for color perception unifying assimilation and contrast. *PLOS Computational Biology*, 15(6):e1007050, 2019.

[89] Andrew Stockman and David H. Brainard. Color vision mechanisms. In Michael Bass, Casimer M. DeCusatis, Jay Enoch, Vasudevan Lakshminarayanan, Guifang Li, Carolyn Macdonald, Virendra N. Mahajan, and Eric van Stryland, editors, *Handbook of Optics, Volume III: Vision and Vision Optics*. McGraw Hill, 3rd edition, 2010.

[90] Cleo M. Stoughton and Bevil R. Conway. Neural basis for unique hues. *Current Biology*, 18(16):R698–R699, 2008.

[91] Steven H. Strogatz. *Nonlinear Dynamics and Chaos: With Applications to Physics, Biology, Chemistry, and Engineering*. Westview Press, 2nd edition, 2015.

[92] Lisa G. Thorell, Russell L. De Valois, and Duane G. Albrecht. Spatial mapping of monkey V1 cells with pure color and luminance stimuli. *Vision Research*, 24(7):751–769, 1984.

[93] Daniel Y. Ts'o, Mark Zarella, and Guy Burkitt. Whither the hypercolumn? *The Journal of Physiology*, 587(12):2791–2805, 2009.

[94] Alan M. Turing. The chemical basis of morphogenesis. *Philosophical Transactions of the Royal Society of London. Series B: Biological Sciences*, 237(641):37–72, 1952.

[95] Maxwell H. Turner, Gregory W. Schwartz, and Fred Rieke. Receptive field center-surround interactions mediate context-dependent spatial contrast encoding in the retina. *Elife*, 7:e38841, 2018.

[96] Arne Valberg. Unique hues: an old problem for a new generation. *Vision Research*, 41(13):1645–1657, 2001.

[97] Thomas F. Varley, Robin Carhart-Harris, Leor Roseman, David K. Menon, and Emmanuel A. Stamatakis. Serotonergic psychedelics LSD & psilocybin increase the fractal dimension of cortical brain activity in spatial and temporal domains. *Neuroimage*, 220:117049, 2020.

[98] Thomas Wachtler, Terrence J. Sejnowski, and Thomas D. Albright. Representation of color stimuli in awake macaque primary visual cortex. *Neuron*, 37(4):681–691, 2003.

[99] Torsten N. Wiesel and David H. Hubel. Spatial and chromatic interactions in the lateral geniculate body of the rhesus monkey. *Journal of Neurophysiology*, 29(6):1115–1156, 1966.

[100] Hugh R. Wilson and Jack D. Cowan. Excitatory and inhibitory interactions in localized populations of model neurons. *Biophysical Journal*, 12(1):1–24, 1972.

[101] Hugh R. Wilson and Jack D. Cowan. A mathematical theory of the functional dynamics of cortical and thalamic nervous tissue. *Kybernetik*, 13(2):55–80, 1973.

[102] Lauren E. Wool, Stanley J. Komban, Jens Kremkow, Michael Jansen, Xiaobing Li, Jose-Manuel Alonso, and Qasim Zaidi. Salience of unique hues and implications for color theory. *Journal of Vision*, 15(2):1–11, 2015.

[103] Sophie M. Wuerger, Philip Atkinson, and Simon Cropper. The cone inputs to the unique-hue mechanisms. *Vision Research*, 45(25-26):3210–3223, 2005.

[104] Youping Xiao. Processing of the S-cone signals in the early visual cortex of primates. *Visual Neuroscience*, 31(2):189–195, 2014.

[105] Youping Xiao, Alexander Casti, Jun Xiao, and Ehud Kaplan. Hue maps in primate striate cortex. *Neuroimage*, 35(2):771–786, 2007.

[106] Xiangmin Xu, William Bosking, Gyula Sáry, James Stefansic, Daniel Shima, and Vivien Casagrande. Functional organization of visual cortex in the owl monkey. *Journal of Neuroscience*, 24(28):6237–6247, 2004.

[107] Takashi Yoshioka and Bruce M. Dow. Color, orientation and cytochrome oxidase reactivity in areas V1, V2 and V4 of macaque monkey visual cortex. *Behavioural Brain Research*, 76(1-2):71–88, 1996.

[108] Qasim Zaidi and Bevil R. Conway. Steps towards neural decoding of colors. *Current Opinion in Behavioral Sciences*, 30:169–177, 2019.